

Institute of Thermoelectricity, Academy of Sciences and Ministry of Education and Science of Ukraine

Journal of THERMOELECTRICITY

International Research

Founded in December, 1993

published 6 times a year

No. I

2014

Editorial Board

Editor-in-Chief LUKYAN I. ANATYCHUK

Petro I. Baransky

Bogdan I. Stadnyk

Lyudmyla N. Vikhor

Vilius Ya. Mikhailovsky

Ivan V. Gutsul

Elena I. Rogacheva

Stepan V. Melnychuk

Andrey A. Snarskii

International Editorial Board

Lukyan I. Anatychuk, *Ukraine*

A.I. Casian, *Moldova*

Steponas P. Ašmontas, *Lithuania*

Takenobu Kajikawa, *Japan*

Jean-Claude Tedenac, *France*

T. Tritt, *USA*

H.J. Goldsmid, *Australia*

Sergiy O. Filin, *Poland*

L.P. Bulat, *Russia*

M.I. Fedorov, *Russia*

L. Chen, *China*

D. Sharp, *USA*

T. Caillat, *USA*

Yuri Gurevich, *Mexico*

Yuri Grin, *Germany*

Founders - National Academy of Sciences, Ukraine
Institute of Thermoelectricity of National Academy of Sciences and Ministry
of Education and Science of Ukraine

Certificate of state registration № KB 15496-4068 ПР

Editorial office manager D. Taschuk

Editors:

L. Vikhor, V. Kramar, V. Katerynchuk, O. Luste, A. Farion, O. Bodnaruk

Approved for printing by the Academic Council of Institute of Thermoelectricity
of the National Academy of Sciences and Ministry of Education and Science, Ukraine

Address of editorial office:

Ukraine, 58002, Chernivtsi, General Post Office, P.O. Box 86.

Phone: +(380-372) 90 31 65.

Fax: +(380-3722) 4 19 17.

E-mail: jt@inst.cv.ua

<http://www.jt.inst.cv.ua>

Signed for publication 25.02.14. Format 70×108/16. Offset paper №1. Offset printing.
Printer's sheet 11.1. Publisher's signature 9.2. Circulation 400 copies. Order 6.

Printed from the layout original made by "Journal of Thermoelectricity" editorial board
in the printing house of "Bukrek" publishers,
10, Radischev Str., Chernivtsi, 58000, Ukraine

Copyright © Institute of Thermoelectricity, Academy of Sciences
and Ministry of Education and Science, Ukraine, 2014

CONTENTS

Theory

L.I. Anatychuk, P.V. Gorsky, [V.P. Mikhachenko] Impact of size effects on the properties of thermoelectric materials 5

P.I. Baranskii, G.P. Haidar. Anisotropy of thermoelectric properties of multi-valley semiconductors of cubic symmetry under the influence of external directional effects 12

Material Research

D.M. Freik, I.I. Chavyak, V.I. Makovishin, I.A. Arsenyuk. Thermoelectric vapour-phase condensate of *p*-type tin telluride 25

G.N. Kozhemyakin, S.Ya. Skipidarov, Yu.M. Krutov, A.N. Paraschenko, O.N. Ivanov, O.N. Soklakova. Nanostructured bismuth and antimony tellurides for thermoelectric heat pump 33

V.A. Romaka, P. Rogl, V.V. Romaka, Yu.V. Stadnyk, R.O. Korzh, A.M. Horyn, V.Ya. Krajovsky, O.I. Lakh. Optimization of parameters of the new thermoelectric material $HfNiSn_{1-x}Sb_x$ 43

Design

Yu.M. Lobunets. Performance analysis of heat-exchange type thermoelectric generator 52

M.P. Volkov, I.A. Drabkin, L.B. Yershova, D.A. Kondratyev. Dynamics of transient processes in multi-stage thermoelectric modules 59

Yu.M. Lobunets. Optimization of thermal schemes of thermoelectric generator with constant-power heat source 65

T.A. Ismailov, O.V. Yevdulov, M.A. Khazanova, R.A.-M. Magomadov. Mathematical model of a thermoelectric system for local thermal effect on human hand 69

News

O.P. Huk (Dedicated to 60th birthday) 81

Discussion

M.A. Korzhuev, V.V. Temyakov. Richmann's and Lomonosov's research in the field of thermoelectricity (1745 – 1753) 82

L.I. Anatychuk, P.V. Gorsky, V.P. Mikhachenko

Institute of Thermoelectricity of the NAS and MES Ukraine, 1, Nauky Str.,
Chernivtsi, 58029, Ukraine

**IMPACT OF SIZE EFFECTS ON THE PROPERTIES
OF THERMOELECTRIC MATERIALS**

Size effects capable of influencing the properties of thermoelectric materials are divided into classical and quantum ones. The former take place when the size of material particle at least along one of coordinate axes is comparable to mean free path of charge or phonon carriers. The latter occur when this size is comparable to the de Broglie wavelength of electrons (holes). This paper deals exclusively with classical size effects. Here, the shape-forming structural elements in the form of small spherical particles and in the form of semi-spheres contacting in a round area (spot) of a radius which is small against the radius of semi-spheres have been analyzed. The impact of size effects on the electric conductivity of material is considered in the approximation of constant (with respect to energy) mean free path of electrons (holes), since exactly this approximation is valid for Bi_2Te_3 with charge carrier scattering on the deformation potential of acoustic phonons in the relevant for thermoelectricity temperature region. The impact of size effects on the lattice thermal conductivity of material is considered in two approximations, namely that of constant mean free path of phonons and the mean free path depending on frequency due to N- and U-processes of phonon collisions which are relevant in the temperature range of 300 K and higher and are capable of modifying scattering on the boundaries. From the results of approximation it follows that in the approximation of constant mean free paths of electrons and phonons there is no gain in the thermoelectric figure of merit when passing from single-crystal to nanostructured, extruded or powder-based SPS-material. However, with regard to frequency dependence of the mean free path of phonons it turns out that in passing from single-crystal to powder-based material, the thermoelectric figure of merit can increase approximately twice with an oriented arrangement of cleavage planes of shape-forming elements or approximately by 20 % with a random arrangement of these planes. In so doing, the sizes of spherical particles of nanostructured material or nanocontacts between micro semi-spheres should lie within 10 to 40 nm.

Key words: nanostructured material, thermoelectric figure of merit, phonons, electrons, scattering, relaxation time, normal processes, Umklapp processes, Rayleigh distribution.

Introduction

Bismuth telluride Bi_2Te_3 is thermoelectric material most commonly used for the manufacture of working elements of various thermoelectric instruments and devices, in particular, generators and coolers [1, 2]. Its specific feature is a pronounced electric conductivity and thermal conductivity anisotropy. This crystal possesses $R\bar{3}m$ group symmetry and a layered structure. Its thermal conductivity and electric conductivity tensors have two independent components each. In particular, in the absence of a magnetic field, electric conductivity tensor has component σ_{11} in layers plane and component σ_{33} in a perpendicular direction, with $\sigma_{11} > \sigma_{33}$. The same inequality is valid for thermal conductivity components: $\chi_{11} > \chi_{33}$. Therefore, thermoelectric modules of a single crystal are made so that temperature gradient and electric current are parallel to cleavage planes, owing to which the

dimensionless thermoelectric figure of merit ZT at 300 K reaches 1. This direction of temperature gradient and electric current can be also retained when passing from single-crystal to powder-based materials prepared by hot pressing, extrusion or spark plasma sintering methods, if cleavage planes of powder particles are parallel to each other. However, it is much more common when cleavage planes of individual particles that coincide with planes of crystal layers are randomly oriented (nonparallel).

As a result, the figure of merit of material in conformity with the Odelevsky formula with regard to the ratios between components of thermal and electric conductivity tensors should have reduced by a factor of about from $\sqrt{2}$ to $\sqrt{3}$, i.e. by 30 to 40 %, however, in practice such a reduction is not observed. On the other hand, there are many theoretical works, for instance [3-5], where it is shown that transition from single-crystal material to bulk nanostructured material should increase the dimensionless thermoelectric figure of merit. As the mechanisms for such increase, on the one hand, phonon scattering on the boundaries of nanoparticles [3], leading to lattice thermal conductivity reduction is considered, on the other hand – quantum tunneling of charge carriers through vacuum or dielectric gaps between particles, leading to increase in electric conductivity and thermoEMF, hence, in power factor [4, 5]. In these papers it is shown that the best values of dimensionless thermoelectric figure of merit of bulk nanostructured material based on bismuth telluride should have achieved $3.5 \div 3.6$, but in practice no such increase takes place. The discrepancy between theory and experiment is generally related to stronger reduction of electric conductivity when passing from single-crystal material to bulk nanostructured material than it is predicted by theory. This factor forces the experimenters to employ combined materials based on powders, consisting of a nanocomponent with particle size $5 \div 20$ nm, and a microcomponent with particle size $40 \div 70\mu\text{m}$ [6]. Such materials possess power factor typical of single-crystal material, but their thermal conductivity is reduced due to additional phonon scattering on the boundaries of nanoparticles. Relative mass fractions of nano- and microcomponents in powder are selected so as to assure maximum value of thermoelectric figure of merit.

Among the weak points of [3-5] and some other theoretical papers covering this problem, is a modeling character of tunneling effects calculations caused by the absence of valid knowledge on the shape and height of potential barriers between nanoparticles, as well as ignoring the frequency dependence of phonon relaxation time when considering their scattering on nanoparticle boundaries.

With regard to the foregoing, the purpose of this paper is to consider the mechanism of thermoelectric figure of merit variation when passing from single-crystal to bulk nanostructured material due to charge carrier and phonon scattering on the boundaries of spherical nanoparticles in the approximation of relaxation time for electrons and phonons.

Thermoelectric figure of merit calculation in the approximation of constant electron and phonon mean free paths

Consider the problem of thermoelectric figure of merit calculation in the approximation of constant electron and phonon mean free paths. It can be shown that in the framework of this approximation thermoEMF is not changed, as long as both thermal diffusion flux and electric current are proportional to relaxation time. Therefore, a change in thermoelectric figure of merit in this case is completely determined by a change in electric conductivity to thermal conductivity ratio. If electron and phonon mean free paths are l_e and l_{ph} , respectively, then the ratio of figure of merit Z_n of the bulk nanostructured material consisting of identical nanoparticles of radius r to figure of merit Z_m of single-crystal material in conformity with the rule of summation of the inverse mean free paths will make [7-9]:

$$\frac{Z_n}{Z_m} = \left[\int_{-1}^1 \int_0^1 \frac{(r/l_e) \sqrt{y^2 + 2zy + 1} y^2 dz dy}{(r/l_e) \sqrt{y^2 + 2zy + 1} + 1} \right] \left[\int_{-1}^1 \int_0^1 \frac{(r/l_p) \sqrt{y^2 + 2zy + 1} y^2 dz dy}{(r/l_p) \sqrt{y^2 + 2zy + 1} + 1} \right]^{-1}. \quad (1)$$

Double integrals over dimensionless variables z and y in this formula appear due to averaging of expressions for thermal conductivity and electric conductivity over the mean free paths inside the sphere.

Consideration of frequency dependence of phonon relaxation time

We now consider the problem of calculation of thermoelectric figure of merit with regard to frequency dependence of relaxation time of mutually scattered phonons. For this purpose, we first write a general expression for lattice thermal conductivity component parallel to layers (cleavage planes), taking into account that in the temperature region relevant for thermoelectric applications it is determined by Umklapp processes, as well as by normal processes, capable of modifying scattering on sample boundaries by virtue of scattering probabilities redistribution according to frequencies [10, 11]. This expression is of the form:

$$\chi_{\parallel} = \frac{3\hbar\rho v_{\parallel}^4 k_B}{32\gamma^2 (k_B T_D)^2 \theta^3 \pi} \int_0^1 \frac{x^4 \exp(x/\theta)}{\left[\exp(x/\theta) - 1\right]^2} \left(\frac{1}{Q_{l\parallel}(x)} + \frac{2}{Q_{t\parallel}(x)} \right) dx. \quad (2)$$

In this formula, index \parallel refers to lattice thermal conductivity in the direction parallel to layers (cleavage planes), ρ is crystal density, v is sound velocity in it, γ is the Gruneisen parameter, T_D is the Debye temperature, $\theta = T/T_D$, $Q_{l\parallel}(x)$ and $Q_{t\parallel}(x)$ are frequency polynomials determined by the mechanisms of scattering the longitudinal and transverse phonons, respectively, and having in this case the form:

$$Q_{l\parallel}(x) = x^4 + \mu_{\parallel} x, \quad (3)$$

$$Q_{t\parallel} = (\mu_{\parallel} + 3.125\theta^3)x. \quad (4)$$

With regard to thermal conductivity dependence on material density, we note that formula (2) in this respect is precise for a simple cubic lattice with one atom in a unit cell. The real Bi_2Te_3 lattice is not of that kind, but we have to replace it by such, provided the real material density is maintained. Coefficient μ was approximately calculated for a simple cubic lattice by Leibfried and Shleman [10], but, according to experimental data given in [10], even for materials with such lattice it is not universal. Therefore, we will derive coefficient μ_{\parallel} from the real value of the respective component of Bi_2Te_3 thermal conductivity tensor [1], assuming that the latter coincides with the theoretical value (2) with regard to (3) and (4). At $\chi_{\parallel} = 1.45 \text{ W/m}\cdot\text{K}$, $\rho = 7859 \text{ kg/m}^3$, $\gamma = 1.5$, $v_{\parallel} = 2952 \text{ m/s}$, $T_D = 155 \text{ K}$ and $T = 300 \text{ K}$ we obtain $\mu_{\parallel} = 0.022$.

The ratio of nanoparticle thermal conductivity to single crystal thermal conductivity in this case is:

$$\frac{\chi_i^{(nano)}}{\chi_{l\parallel|m}} = 1.5 \int_0^1 \int_{-1}^1 \frac{z^2 x^4 \exp(x/\theta)}{\left[\exp(x/\theta) - 1\right]^2} \left(\frac{(r/L^*) \sqrt{z^2 - 2zy + 1}}{1 + (r/L^*) Q_{l\parallel}(x) \sqrt{z^2 - 2zy + 1}} + \right. \\ \left. + \frac{2(r/L^*) \sqrt{z^2 - 2zy + 1}}{1 + (r/L^*) Q_{t\parallel}(x) \sqrt{z^2 - 2zy + 1}} \right) dy dz dx \left\{ \int_0^1 \frac{x^4 \exp(x/\theta)}{\left[\exp(x/\theta) - 1\right]^2} \left(\frac{1}{Q_{l\parallel}(x)} + \frac{2}{Q_{t\parallel}(x)} \right) dx \right\}^{-1}. \quad (5)$$

In formula (5) $L^* = \rho \hbar^4 v_{\parallel}^6 / \gamma^2 (k_B T_D)^5$.

In this case, the ratio of the figure of merit of bulk nanostructured material to that of single-crystal material will be:

$$Z_n/Z_m = 1.5 \left[\int_0^1 \frac{(r/l_e) \sqrt{y^2 + 2zy + 1} y^2 dz dy}{(r/l_e) \sqrt{y^2 + 2zy + 1} + 1} \right] \left[\chi_l^{(nano)} / \chi_{l||m} \right]^{-1}. \quad (6)$$

In the case of micro semi-spheres contacting in a round area (spot) of radius r , formulae (5) and (6) take on the form [12]:

$$\begin{aligned} \chi_l^{(nano)} / \chi_{l||m} &= \pi^{-1} \int_0^1 \int_0^{2\pi} \frac{zx^4 \exp(x/\theta)}{\left[\exp(x/\theta) - 1 \right]^2} \left(\frac{(r/L^*) \sqrt{z^2 - 2z \cos \phi + 1}}{1 + (r/L^*) Q_{l||}(x) \sqrt{z^2 - 2z \cos \phi + 1}} + \right. \\ &\quad \left. + \frac{2(r/L^*) \sqrt{z^2 - 2z \cos \phi + 1}}{1 + (r/L^*) Q_{l||}(x) \sqrt{z^2 - 2z \cos \phi + 1}} \right) d\phi dz dx \left\{ \int_0^1 \frac{x^4 \exp(x/\theta)}{\left[\exp(x/\theta) - 1 \right]^2} \left(\frac{1}{Q_{l||}(x)} + \frac{2}{Q_{t||}(x)} \right) dx \right\}^{-1}. \end{aligned} \quad (7)$$

$$Z_n/Z_m = \pi^{-1} \left[\int_0^1 \int_0^1 \frac{(r/l_e) \sqrt{y^2 + 2y \cos \phi + 1} y^2 dz dy}{(r/l_e) \sqrt{y^2 + 2y \cos \phi + 1} + 1} \right] \left[\chi_l^{(nano)} / \chi_{l||m} \right]^{-1}. \quad (8)$$

Dependence of the ratio of thermoelectric figure of merit of bulk nanostructured material to that of single-crystal material based on Bi_2Te_3 $(ZT)_{nano}/(ZT)_{mono}$ on the radius of nanoparticles is shown in Fig 1.

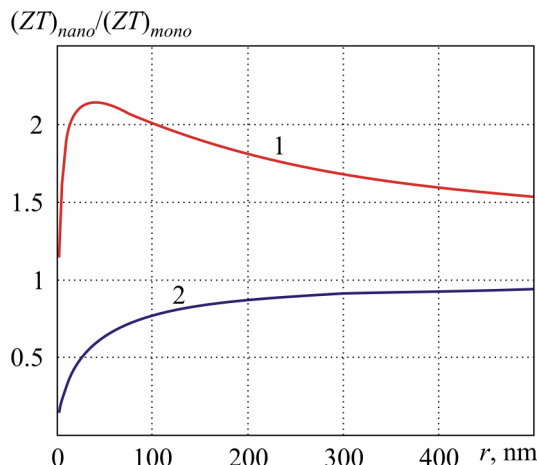


Fig. 1. Dependences of the ratio of thermoelectric figure of merit of bulk nanostructured material to that of single-crystal material $(ZT)_{nano}/(ZT)_{mono}$ on nanoparticle radius: 1 – with regard to frequency dependence of phonon relaxation time; 2 – in the approximation of constant mean free paths of electrons and phonons.

In the calculations, based on the reference data [1] it was assumed that $l_{ph} = 4.16$ nm, $l_e = 38.6$ nm at a temperature of 300 K. In connection with Fig.1, a question may arise as to the validity of transferring the properties of an individual nanoparticle to the properties of material as a whole. Therefore, we note that if pores in material structure are vacuum and separated from each other, and no tunneling of charge carriers takes place, then material porosity, both in the framework of percolation theory, and within the approach set forth, for instance, in [5], enters into the expressions for thermal conductivity and electric conductivity through the same multiplier, hence, it does not produce a direct effect on the thermoelectric figure of merit. Thus, abstracting from the size distribution of nanoparticles, the thermoelectric figure of merit of material as a whole is unambiguously determined through the kinetic coefficients of an individual particle.

From Fig. 1 it is evident that with regard to frequency dependence of phonon relaxation time the thermoelectric figure of merit of bulk nanostructured material in the range of nanoparticle radii $35 \div 40$ nm achieves a maximum which exceeds the thermoelectric figure of merit of single-crystal material by a factor of 2.14. However, such maximum is possible only with parallel cleavage planes of individual nanoparticles. With randomly oriented cleavage planes, the thermoelectric figure of merit of Bi_2Te_3 based bulk nanostructured material will be a factor of $\sqrt{3}$ lower, i.e. it will remain at a level of about 23 % higher than the thermoelectric figure of merit of single-crystal material. Even with nanoparticle radius of the order of 5 nm with correction for random orientation of cleavage planes, the thermoelectric figure of merit of bulk nanostructured material should remain at a level of at least 97 % of the thermoelectric figure of merit of a single crystal. These results are in qualitative, as well as quantitative agreement with the results of experimental works [13, 14], but contradict to the results of paper [6] according to which the thermoelectric figure of merit of Bi_2Te_3 based bulk nanostructured material of nanoparticles with the radius $5 \div 20$ nm at 300 K is as low as 82 % of the thermoelectric figure of merit of a single crystal. Thus, when passing from single-crystal material to bulk nanostructured material, power factor is scarcely ever retained, which permits calling in question the presence of energy filtration of current carriers that should have resulted in thermoEMF increase. Even if such filtration occurs, then, apparently, it does not always contribute to power factor retention, since electric conductivity reduction is not compensated by increase in squared thermoEMF. However, in the approximation of constant mean free paths of electrons and phonons the thermoelectric figure of merit values of the bulk nanostructured materials exceeding unity are mainly attributable to tunneling effects.

The results for a circular contact are identical, but slightly different in the numerical values.

Consider now the impact on these results of temperature and size distribution of the bulk nanostructured material particles. The impact of temperature on the scattering of electrons and phonons on the boundaries will be taken into account through temperature dependences of parameters L^* and l_e according to formulae [1, 10]:

$$L^* = \rho \hbar^4 v_{||}^6 / \gamma^2 \theta (k_B T_D)^5, \quad (9)$$

$$l_e = l_e(300) \frac{300}{T}. \quad (10)$$

According to the definition, adjustable parameter $\mu_{||}$ does not depend on temperature, since on evidence derived from [1] the Leibfried-Shleman evaluation formula reflects correctly the temperature dependence of Bi_2Te_3 lattice conductivity in the range from nitrogen to room temperatures and higher. The size distribution of particles will be taken into account based on the Rayleigh distribution for which the dependence of probability density $w(r)$ on particle radius r is given by:

$$w(r) = \frac{r}{r_0^2} \exp\left(-\frac{r^2}{r_0^2}\right). \quad (11)$$

In this case the generally effective material parameters σ_{ef} and χ_{lef} are determined by two methods. The first method lies in solving phenomenological equations for the distributions of temperature and electric potential in an individual particle based on simulation of its geometry. The second method lies in using the Odelevsky relations with averaging the equations for σ_{ef} and χ_{lef} over the volumetric share of “phases”, i.e. in this case, particles of various sizes [5]. However, our analysis shows that the latter case of determination of the effective electric conductivity and thermal conductivity of material with a high degree of precision is equivalent to their simple averaging over

the volumetric share of particles of various sizes. There is no need in conversion of thermoEMF value, since in the approximation of constant (with respect to energy) mean free path of charge carriers it does not depend on the boundary scattering. Based on this, we have determined the temperature dependence of optimal most probable radius R_{opt} of powder nanoparticle in the temperature range of 75 to 600 K and the temperature dependence of maximum thermoelectric figure of merit at these temperatures. The most probable nanoparticle radius was taken to be optimal when the ratio of thermoelectric figure of merit of bulk nanostructured material to that of single-crystal material at each investigated temperature reaches its maximum. The corresponding dependences are depicted in Fig. 2.

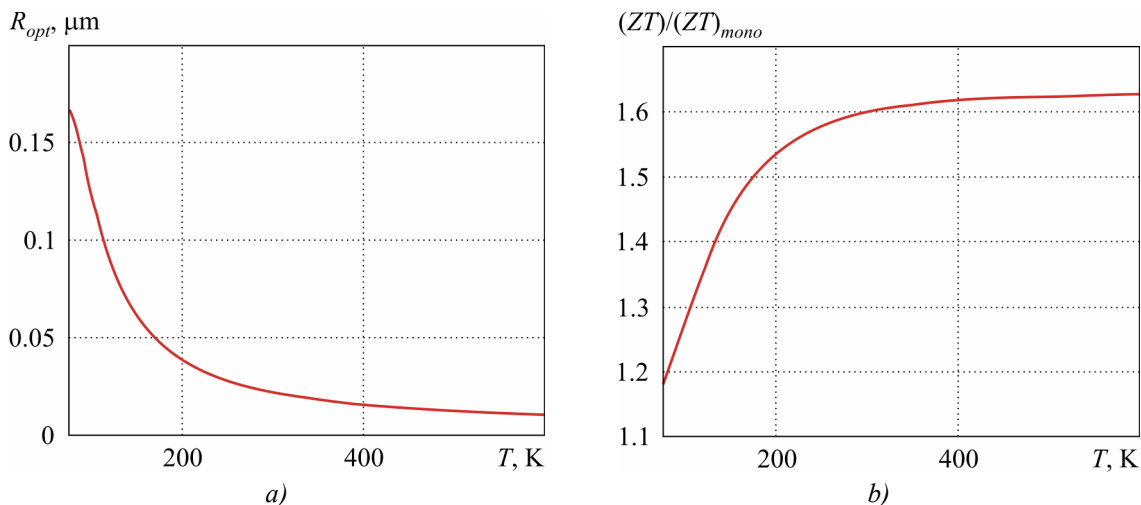


Fig. 2. Temperature dependences in the range of 75 to 600 K: a) – optimal most probable nanoparticle radius; b) – the ratio of thermoelectric figure of merit of bulk nanostructured material to that of single-crystal material.

From Fig. 2 it is seen that with temperature increase from 75 to 600 K, the optimal most probable nanoparticle radius decreases from 0.17 μm to 0.01 μm , and the ratio of thermoelectric figure of merit of bulk nanostructured material to that of single-crystal material (on condition of optimality of the most probable nanoparticle radius) increases from 1.19 to 1.63.

Conclusions and recommendations

1. In the approximation of constant mean free paths of charge carriers and phonons the thermoelectric figure of merit of bulk nanostructured material based on Bi_2Te_3 , calculated with regard to classical size effects does not exceed the thermoelectric figure of merit of single-crystal material.
2. With regard to frequency dependence of the relaxation time of mutually scattered phonons it turns out that in the range of nanoparticle radii 40 \div 500 nm the thermoelectric figure of merit of bulk nanostructured material based on Bi_2Te_3 can exceed by a factor of 1.5 \div 2.1 the thermoelectric figure of merit of single-crystal material. It is true, if cleavage planes of individual crystallites are oriented parallel to temperature gradient and electric current directions. However, if cleavage planes are randomly oriented, the thermoelectric figure of merit of such nanostructured material will remain on the level of 0.88 \div 1.23 of that of single-crystal material.
3. The lower values of thermoelectric figure of merit of bulk nanostructured materials are attributable to a drop in power factor due to thermoEMF reduction in these materials with respect to single-crystal material.

References

1. B.M. Goltzman, V.A. Kudinov, and I.A. Smirnov, *Semiconductor Thermoelectric Materials Based on Bi₂Te₃* (Moscow: Nauka, 1972), 320 p.
2. L.W. Da Silva, M. Cavany Micro-thermoelectric cooler: interfacial effect on thermal and electrical transport. *Int. J. of Heat and Mass Transfer* **47**, 2417 – 2435 (2004).
3. L.P. Bulat, I.A. Drabkin, V.V. Karataev, V.B. Osvensky and D.A. Pshenai-Severin, The Effect of Boundary Scattering on the Thermal Conductivity of Nanostructured Bi_xSb_{2-x}Te₃ Semiconductor Material, *Physics of the Solid State* **52**, 1712 (2010).
4. L.P. Bulat, V.V. Osvensky, Yu.N. Parkhomenko, and D.A. Pshenai-Severin, Study on the Possibilities of Thermoelectric Figure of Merit Improvement in Nanostructured Materials Based on Bi₂Te₃-Sb₂Te₃, *Physics of the Solid State* **54**, 20 – 26 (2012).
5. A.A. Snarskii, A.K. Sarychev, I.V. Bezsdunov, and A.N. Lagarkov, Thermoelectric Figure of Merit of the Bulk Nanostructured Composites with Distributed Parameters, *Semiconductors* **46**, 677 – 683 (2012).
6. S. Fan, J. Zhao, J. Guo, Q. Yan, J. Ma, H.H. Hang, Influence of Nanoinclusions on Thermoelectric Properties of *n*-type Bi₂Te₃ Nanocomposites, *Journal of Electronic materials* **40** (5), 1018 – 1023 (2011).
7. P.V. Gorsky, V.P. Mikhalchenko, Reduction of Thermoelectric Material Lattice Thermal Conductivity Using Shape-Forming Element Optimization, *J. Thermoelectricity* **1**, 18 – 25 (2013).
8. P.V. Gorsky, V.P. Mikhalchenko, On the Electric Conductivity of Contacting Particles of Thermoelectric Material, *J. Thermoelectricity* **2**, 12 – 18 (2013).
9. P.V. Gorsky, V.P. Mikhalchenko, Effect of Thermoelectric Material Anisotropy on the Electric Conductivity and Lattice Thermal Conductivity of its Contacting Particles, *J. Thermoelectricity* **3**, 5 – 10 (2013).
10. P.G. Klemens, Lattice Thermal Conductivity. In: *Solid State Physics. Advances in Research and Applications*. Vol. 7, pp. 1 – 98 (New York: Academic Press. Inc. Publishers, 1958), 526 p.
11. P. Klemens, Effect of Thermal and Phonon Processes on Ultrasound Attenuation, In: *Physical Acoustics, Vol 3, Part B, Lattice Dynamics*, Ed. By W. Mason, P. 244 – 284 (Moscow: Mir, 1968), 526 p.
12. P.V. Gorsky, V.P. Mikhalchenko, On the Issue of the Mechanism for Increasing the Thermoelectric Figure of Merit of the Bulk Nanostructured Materials, *J. Thermoelectricity* **5**, 5 – 9 (2013).
13. V.T. Bublik, I.A. Drabkin, V.V. Karataev, et al., Bulk Nanostructured Thermoelectric Material Based on (Bi, Sb)₂Te₃ Prepared by Spark Plasma Sintering Method (SPS), *Thermoelectrics and Their Applications: XIII Interstate Workshop* (Saint-Petersburg, 2012).
14. I.A. Drabkin, V.B. Osvensky, A.I. Sorokin, et.al., Anisotropy of Thermoelectric Properties of the Bulk Nanostructured Material Based on (Bi, Sb)₂Te₃ Prepared by Spark Plasma Sintering Method (SPS), *Thermoelectrics and their Applications: XIII Interstate Workshop* (Saint-Petersburg, 2012).
15. P.V. Gorsky, S.V. Melnychuk, Impact of Layered Structure Effects and Charge Ordering on ThermoEMF of Thermoelectric Materials in a Quantizing Magnetic Field, *J. Thermoelectricity* **6**, 7 – 12 (2013).

Submitted 25.09.2013.

P.I. Baranskii¹, G.P. Haidar²



P.I. Baranskii

¹V.E. Lashkaryov Institute of Semiconductor Physics,
NAS Ukraine, 45, Nauky Ave., Kyiv, 03028, Ukraine;

²Institute for Nuclear Research, NAS Ukraine,
47, Nauky Ave., Kyiv, 03680, Ukraine



G.P. Haidar

ANISOTROPY OF THERMOELECTRIC PROPERTIES OF MULTI-VALLEY SEMICONDUCTORS OF CUBIC SYMMETRY UNDER THE INFLUENCE OF EXTERNAL DIRECTIONAL EFFECTS

Analysis of electronic processes developed in multi-valley semiconductors of cubic symmetry under the influence of uniaxial elastic strain and magnetic (nonquantizing) field of arbitrary intensity has been performed. The relationships between thermoEMF anisotropy $\Delta\alpha = \alpha_{||} - \alpha_{\perp}$ and the anisotropy parameters of electron-phonon drag thermoEMF $M = \alpha_{||}^{ph}/\alpha_{\perp}^{ph}$ and mobility anisotropy $K = \mu_{\perp}/\mu_{||}$ in a single isoenergetic ellipsoid, as well as changes in resistivity $\Delta\rho$ in a field of directional pressure or in an external magnetic field have been investigated.

Key words: multi-valley semiconductors, kinetic phenomena, scattering anisotropy, electric and magnetic fields, directional elastic strain.

Introduction

The use of thermoelectricity and increase of its role in metrology and power engineering is related to creation of thermoelectric materials with maximum values of thermoelectric figure of merit ZT . In particular, semiconductors used as thermocouple legs with thermoelectric figure of merit $ZT \geq 1$ have been already synthesized [1, 2]. Certain advances have been made in the theory of thermoelectric effects, though for the anisotropic semiconductors of noncubic symmetry it is not sufficiently developed. The boundary values of thermoelectric figure of merit for such semiconductors have not been found yet, the influence of structural features on their thermoelectric properties has not been determined.

The electrophysical properties of semiconductors are largely dependent not only on microlevel anisotropy (anisotropy of dispersion law and mechanisms of carrier scattering on phonons and impurity centres, phonon-phonon scattering, etc), but also on macrolevel anisotropy, that is, on the natural (or induced, for instance, by means of directional elastic strain) anisotropy of the entire crystal.

Prior to the development of anisotropic scattering theory there had been no substantiated and consecutive analysis of the results of microlevel anisotropy transformation into macrolevel under the influence of external effects on the crystal.

The purpose of this paper is to perform a consecutive analysis of the influence of both internal characteristics (structural and anisotropic features) of crystals, and the external effects on their thermoelectric and thermomagnetic properties. Attention is focused on the mechanisms of formation and methods of revealing the macroscopic anisotropy of thermoelectric properties of multi-valley semiconductors of cubic symmetry under the influence of external directional effects.

Thermoelectric effects in semiconductors

In semiconductors with the anisotropic energy spectrum of carriers the kinetic coefficients in the general case are of tensor nature. In particular, the Seebeck coefficient α in the anisotropic semiconductor is a second-rank tensor ($\hat{\alpha}$). Unlike the tensors $\hat{\sigma}$, $\hat{\rho}$ and $\hat{\chi}$, the thermoEMF tensor is nonsymmetrical. Let us consider in more detail the properties and features of tensor $\hat{\alpha}$ in semiconductors and the physical factors that determine it.

The tensor nature of $\hat{\alpha}$ is first of all responsible for thermoEMF anisotropy. The primary reason for all peculiarities of thermoelectric effects, including origination of thermoEMF anisotropy, is, no doubt, the kind of dependence of carrier energy \mathcal{E} on quasi-pulse \vec{p} , that is the form of dispersion law $\mathcal{E}(\vec{p})$. The influence of dependence $\mathcal{E}(\vec{p})$ on the properties of tensor $\hat{\alpha}$ is defined by superposition of the internal and external (with regard to semiconductor) conditions which, in fact, assure transformation or joint exhibition of micro- and macrolevel anisotropies. Analyzing these factors, one can conclude that in each specific case the thermoEMF anisotropy arises only when a number of conditions are fulfilled.

1. Suppose that we have a single-valley semiconductor, and carriers of one sort take place in charge transport. Charge carrier scattering will be assumed to be nearly isotropic. The expression for the Seebeck coefficient in this case is of the form [2]:

$$\alpha_i = \frac{k}{e} \frac{\int \tau(\mathcal{E}) \frac{\partial n}{\partial \mathcal{E}} v_i^2 \left(\frac{\mathcal{E} - \xi_0}{kT} \right) d\mathcal{E}}{\int \tau(\mathcal{E}) \frac{\partial n}{\partial \mathcal{E}} v_i^2 d\mathcal{E}}, \quad (1)$$

where $\tau(\mathcal{E})$ is relaxation time, ξ_0 / kT is a reduced chemical potential. From (1) it follows that in the case when, for instance, the degree of nonparabolicity of quasi-pulse dependence of energy at least for two different directions is different (hence, the energy dependence of components of velocity v of charge carriers has a different form for these directions), the thermoEMF anisotropy can arise.

2. Let there be two sorts of carriers in a semiconductor and at least one of which (for instance, electrons) is characterized by the anisotropic effective mass. It can be shown [3] that under this condition the thermoEMF anisotropy is created

$$\Delta \alpha = \alpha_{||} - \alpha_{\perp} = \frac{\sigma_{\perp} - \sigma_{||}}{\sigma} \frac{\alpha_p - \alpha_n}{\left(1 + \frac{\sigma_{||}}{\sigma} \right) \left(1 + \frac{\sigma_{\perp}}{\sigma} \right)}, \quad (2)$$

where α_p and α_n are the Seebeck coefficients of holes and electrons, respectively, $\sigma_{||}$ and σ_{\perp} are components of the electric conductivity tensor of electrons, σ is the electric conductivity of holes.

3. Suppose that the energy spectrum of one sort of carriers in a single-valley semiconductor is anisotropic, and

$$\mathcal{E}(\vec{p}) = \frac{p_1^2 + p_2^2}{2m_1} + \frac{p_3^2}{2m_3}. \quad (3)$$

Here, m_1 and m_3 are the transverse and longitudinal effective masses of carriers in constant-energy ellipsoid, respectively; p_1 and p_2 ($p_1 = p_2$) are the components of the pulses in ellipsoid transverse section, and p_3 – in longitudinal section. Assuming that $m_3 > m_1$, the constant-energy surface in this case will have the form of an elongated ellipsoid of revolution. The effective mass anisotropy causes

in the general case the anisotropy of scattering [4], and the symmetry of differential mobility tensor corresponds to the symmetry of energy minimum. Let in the presence of one or several scattering mechanisms the dependence $\hat{\mu}(x)$ (of relaxation time tensor) on the reduced energy of charge carriers $x = \xi/kT$ be written as

$$\left. \begin{aligned} \mu_{\perp}(x) &= \mu_{\perp}(T) x^{-q} f_{\perp}(x) \\ \mu_{\parallel}(x) &= \mu_{\parallel}(T) x^{-q} f_{\parallel}(x) \end{aligned} \right\}, \quad (4)$$

(where $f_{\perp}(x)$ and $f_{\parallel}(x)$ are certain functions of x , effective masses and other semiconductor parameters). Then for the nondegenerate semiconductor

$$\left. \begin{aligned} \alpha_{\perp} &= \frac{\langle \alpha(x) \mu_{\perp}(x) \rangle}{\langle \mu_{\perp}(x) \rangle} \\ \alpha_{\parallel} &= \frac{\langle \alpha(x) \mu_{\parallel}(x) \rangle}{\langle \mu_{\parallel}(x) \rangle} \end{aligned} \right\}, \quad (5)$$

where angular brackets in (5) denote the generally accepted averaging over energy, and

$$\alpha(x) = \frac{k}{e} \frac{\xi - \xi_0}{k T} \quad (6)$$

has the meaning of the Seebeck coefficient of a group of electrons with the energy ξ .

Note that with the power energy dependence $\hat{\mu}(x)$ and $f_{\perp} = f_{\parallel} = 1$ the thermoEMF anisotropy disappears. For a more complicated than that expressed by formula (3) energy spectrum of charge carriers (for instance, the Kane one) the symmetry of tensor $\hat{\alpha}$ is reduced.

4. Suppose that the conditions of the previous item are fulfilled, but crystal temperature is considerably lower than the Debye temperature. In this case (in the presence of temperature gradient ∇T) of considerable importance will be the effect of charge carrier drag by the long-wave phonons. From the kinetic theory it follows that under these conditions even in the case of power dependence of $\hat{\mu}$ on x , components of the tensor of electron-phonon drag thermoEMF are not identical and are described by the expressions [5]

$$\alpha_{\perp}^{ph} = \frac{\langle \mu_{\perp}(x) \alpha_{\perp}^{ph}(x) \rangle}{\langle \mu_{\perp}(x) \rangle}, \quad (7)$$

$$\alpha_{\parallel}^{ph} = \frac{\langle \mu_{\parallel}(x) \alpha_{\parallel}^{ph}(x) \rangle}{\langle \mu_{\parallel}(x) \rangle}. \quad (8)$$

As long as with the drag of electrons by long-wave phonons the anisotropy parameter of the drag thermoEMF is $M = \alpha_{\parallel}^{ph}(x)/\alpha_{\perp}^{ph}(x) \sim m_3/m_1$ (m_3/m_1 is the ratio of the effective masses of charge carriers along the principal axes of isoenergetic ellipsoid), its numerical value can become considerable (for instance, in n -Ge $M = 9.7$).

5. Let us consider a multi-valley semiconductor with S valleys in the Brillouin zone, in each of which the law of dispersion is defined by expression (3). In this case the energy minima in crystal of cubic symmetry will be located on triad or tetrad axes, all the valleys under given conditions being energetically equivalent. Adding currents in each valley that are described by the generalized electric conductivity law

$$\vec{j} = \hat{\sigma}^{(k)} \left(\frac{\nabla \xi}{e} + \hat{\alpha}^{(k)} \nabla T \right), \quad (9)$$

where $\hat{\sigma}^{(k)}$ and $\hat{\alpha}^{(k)}$ are the tensors of the electric conductivity and thermoEMF in k -th valley, respectively, and ξ is electrochemical potential, it is easy to verify that due to cubic symmetry all kinetic tensors degenerate into scalars. So, not only thermoEMF, but even electric conductivity in a cubic semiconductor is isotropic.

The situation will be quite different if in the case of a cubic multi-valley semiconductor we remove, for instance, via uniaxial elastic strain the degeneration of isoenergetic ellipsoids in energy. Assuming that the only result of the influence of uniaxial elastic strain will be redistribution of electrons among the valleys, the nonequivalence of the latter can be conveniently characterized by the relative number of electrons $n_k = N_k/N$ in k -th valley of a strained semiconductor, where N_k is the absolute number of electrons in k -th valley of a strained semiconductor, and $N = SN_0$ is the total number of electrons in S valleys (N_0 is the number of electrons in one valley of an unstrained crystal). As a result of adding currents in the valleys, the tensors

$$\hat{\sigma} = \sum_{k=1}^S \hat{\sigma}^{(k)}, \quad \hat{b} = -\sum_{k=1}^S \hat{\sigma}^{(k)} \hat{\alpha}^{(k)}, \quad (10)$$

characterizing an uniaxially strained crystal, do not generate into scalars, but become proportional either to tensor

$$\hat{C} = \sum_{k=1}^S n_k \hat{Q}^{(k)} \quad (11)$$

(tensor \hat{C} is the phonon part of tensor \hat{b}), or to tensor \hat{C} and tensor

$$\hat{\bar{C}} = \sum_{k=1}^S n_k \ln \frac{n_0}{n_k} \hat{Q}^{(k)} \quad (12)$$

(tensor $\hat{\bar{C}}$ is the electron part of tensor \hat{b}).

Tensor $\hat{Q}^{(k)}$ in (11) and (12) is of geometric origin, since its components are assigned by the equality

$$Q_{ij}^{(k)} = g_{i3}^{(k)} g_{j3}^{(k)}, \quad (13)$$

where $g_{i3}^{(k)}$ is an element of transition matrix from a coordinate system related to the principal axes of k -th mass ellipsoid to a design coordinate system. As long as in a strained system $\hat{\sigma}$ (or $\hat{\rho}$) and \hat{b} are tensors, the Seebeck coefficient should also exhibit tensor properties, namely:

$$\hat{\alpha} = -\hat{\rho} \hat{b}. \quad (14)$$

Let us dwell in more detail on the analysis of thermoEMF anisotropy in uniaxially strained germanium and silicon of n -type. We will arrange strain axis in $(1\bar{1}0)$ plane, and its orientation will be assigned by angle γ which can be conveniently counted off (in the same plane $(1\bar{1}0)$ from direction $[00\bar{1}]$ toward the strain).

In the temperature range where electron-phonon drag is negligible, it gives rise to electron thermoEMF anisotropy that essentially depends on mechanical strain X and strain angle γ . Fig. 1 (n -Ge) and Fig. 2 (n -Si) show the dependences of electron (diffusion) thermoEMF anisotropy on strain angle.

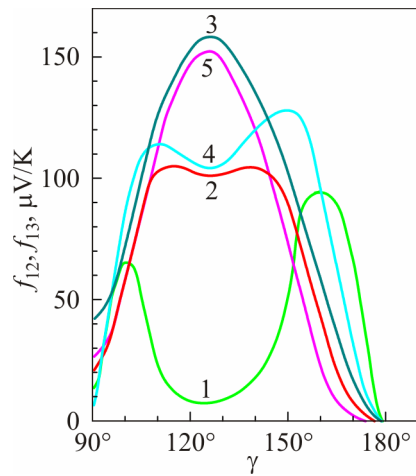


Fig. 1. Dependences of the difference in diagonal components of tensor $\hat{\alpha}$ on strain angle in n-Ge ($\alpha_{11} - \alpha_{22} = f_{12}$ and $\alpha_{11} - \alpha_{33} = f_{13}$) at $T = 300$ K. f_{13} , X (GPa): 1 – 2; 3 – 0.7; 4 – 1.2. f_{12} , X (GPa): 2 – 1.2; 5 – 0.7.

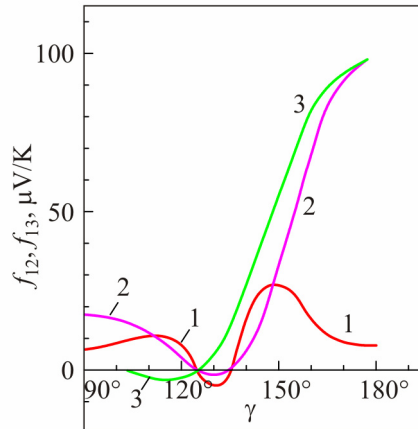


Fig. 2. Angular dependences of the difference in diagonal components $\alpha_{11} - \alpha_{22} = f_{12}$ and $\alpha_{11} - \alpha_{33} = f_{13}$ of tensor $\hat{\alpha}(X)$ in n-Si at $T = 300$ K. f_{12} , X (GPa): 1 – 2; 2 – 0.7. f_{13} , X (GPa): 3 – 0.7.

The electron thermoEMF anisotropy in n-Ge reaches its maximum under crystals strain along the volumetric diagonal $<111>$, and in n-Si – under strain along cube edge $<100>$ due to intermediate values of X . It can be shown that for the above orientations of strain axis in n-Ge

$$\Delta\alpha^e = \frac{4k}{e} \frac{K-1}{K} \frac{2K+1}{3K} \frac{n_1 n_2 \ln \frac{n_1}{n_2}}{\left(1 - \frac{4}{3}n_2 \frac{K-1}{K}\right) \left(\frac{1}{K} + \frac{8}{3}n_2 \frac{K-1}{K}\right)}, \quad (15)$$

and in n-Si

$$\Delta\alpha^e = \frac{4k}{e} \frac{K-1}{K} \frac{2K+1}{3K} \frac{n_1 n_2 \ln \frac{n_1}{n_2}}{\left(1 - 2n_1 \frac{K-1}{K}\right) \left(1 - 2n_2 \frac{K-1}{K}\right)}, \quad (16)$$

where n_1 is a relative number of electrons in a valley located along strain axis, n_2 – in each of the valleys located at an angle to strain axis, $K = \mu_\perp/\mu_\parallel$ is mobility anisotropy parameter.

Formulae (15) and (16) show that a) electronic thermoEMF anisotropy in uniaxially strained

multi-valley semiconductors (the microlevel electronic thermoEMF anisotropy) is exceptionally due to mobility anisotropy on a microlevel (that is, in isoenergetic ellipsoid taken individually); *b*) the thermoEMF anisotropy $\Delta\alpha^e$ value vanishes in *n-Ge* and in *n-Si* both in the absence of strain ($n_1 = n_2$), and in the presence of heavy strain providing full migration of electrons into one ellipsoid ($n_1 = 0$ or $n_2 = 0$).

Maximum value of drag thermoEMF anisotropy is observed under strain of *n-Ge* along <111> and *n-Si* along <001> (as in the case of electronic component), and change in $\Delta\alpha^{ph}$ under strain is basically different from the similar dependences for $\Delta\alpha^e$ which immediately follows from comparison of formulae (15) and (16) to relations (17) and (18) (where $\Delta\alpha^{ph}$ is the phonon component of thermoEMF in unstrained crystal).

For *n-Ge*

$$\Delta\alpha^{ph} = \alpha_0^{ph} \frac{M-1}{K} \frac{2K+1}{2K+M} \frac{n_1-n_2}{\left(1-\frac{4}{3}n_2 \frac{K-1}{K}\right)\left(\frac{1}{K}+\frac{8}{3}n_2 \frac{K-1}{K}\right)}. \quad (17)$$

For *n-Si*

$$\Delta\alpha^{ph} = 2\alpha_0^{ph} \frac{M-1}{K} \frac{2K+1}{2K+M} \frac{n_1-n_2}{\left(1-2n_1 \frac{K-1}{K}\right)\left(1-2n_2 \frac{K-1}{K}\right)}. \quad (18)$$

The reason for drag thermoEMF anisotropy in this case (see (17) and (18)) is not only drag thermoEMF in each of the valleys, but also strain-caused nonequivalence of the latter.

The specific feature of the anisotropy of the phonon part of thermoEMF $\Delta\alpha^{ph}$ is that unlike $\Delta\alpha^e$, with increase in crystal mechanical compression strain X , it continues to increase and with rather high values of X reaches the saturation, whereas $\Delta\alpha^e(X)$, on passing the maximum, with further increase in X tends to zero.

Under conditions whereby its contribution to thermoEMF anisotropy of a semiconductor with a damaged cubic symmetry (due to uniaxial elastic strain) is made by the nonequivalence of valleys (where the energy spectrum is anisotropic even in the absence of strain), the same nonequivalence of valleys leads to the anisotropy of $\hat{\rho}$, and the relation between tensors $\hat{\alpha}^{ph}$ and $\hat{\rho}$, according to reliable calculations, can be given as

$$\hat{\alpha}^{ph} = \alpha_0^{ph} \left[\frac{K-M}{K-1} \frac{2K+1}{2K+M} \hat{I} + \frac{M-1}{K-1} \frac{3K}{2K+M} \frac{\hat{\rho}}{\rho_0} \right]. \quad (19)$$

From this formula follows a linear dependence of the nondiagonal components of tensors $\hat{\alpha}$ and $\hat{\rho}$, and at sufficiently high X ($X \geq 0.6$ GPa) the electronic part of nondiagonal components vanishes. Hence, relation (19) allows experimental determination of parameter M .

Formula (19) yields two nontrivial and practically useful results. First, it implies that relative changes in $\Delta\alpha^{ph}/\Delta\alpha_0^{ph}$ and $\Delta\rho/\Delta\rho_0$ induced by uniaxial elastic strain are interrelated by boundary simple relation

$$\frac{\Delta\alpha^{ph}}{\alpha_0^{ph}} = \frac{M-1}{K-1} \cdot \frac{3K}{2K+M} \cdot \frac{\Delta\rho}{\rho_0}, \quad (20)$$

which makes it possible to measure the value of M (with known K) according to measured values $\Delta\alpha^{ph}/\Delta\alpha_0^{ph}$ and $\Delta\rho/\Delta\rho_0$. Second, formula (19) assures (with known K and M) producing the drag thermoEMF anisotropy $\Delta\alpha^{ph}/\Delta\alpha_0^{ph}$ according to the values of resistivity anisotropy $\Delta\rho/\Delta\rho_0$ for the same crystal.

Note that $\Delta\alpha^{ph}$ and $\Delta\rho$ in (20) correspond to the difference in diagonal components, since during

the experimental investigations of tensors $\hat{\alpha}^{ph}(X; \gamma)$ and $\hat{\rho}(X; \gamma)$ one usually restricts oneself to the most characteristic orientations of strain axis that assure at high X a realization of single- or double-valley model. In $n\text{-Ge}$ such orientations are matched by $\gamma = \delta$ (single-valley model) and $\gamma = 90^\circ$ (two-valley model), and in $n\text{-Si}$ – $\gamma = 0$ and $\gamma = 90^\circ$, respectively. In so doing, δ is the angle that determines a direction of strain axis along the volumetric diagonal of the cube, when $\tan \delta = \sqrt{2}$. At $\gamma < \delta$ the angle δ is between the directions $[00\bar{1}]$ and $[\bar{1}\bar{1}1]$.

Fig. 3 shows angular dependences of the components of tensor $\hat{\alpha}$ calculated and experimentally measured for $n\text{-Ge}$ crystals at $X = 1$ GPa and $T = 85$ K, and Fig. 4 shows the angular dependence of the drag piezothermoEMF $\alpha_{11} = f(\gamma)$, found for $n\text{-Si}$ crystals at $X = 0.8$ GPa and $T = 85$ K. The results presented in these figures testify to a good agreement between theory and experiment. Emphasis should be placed on the value of thermoEMF and its anisotropy in strained silicon that increases the respective values for other materials by two-three orders.

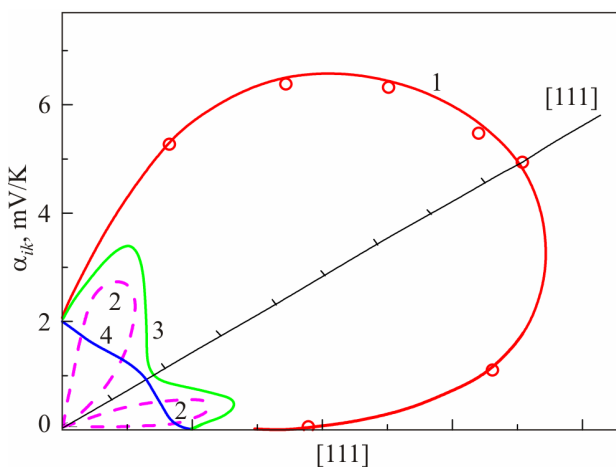


Fig. 3. Angular dependences of the components of tensor $\hat{\alpha}$ in plane $(1\bar{1}0)$ for $n\text{-Ge}$ with $n_e = 1.6 \cdot 10^{13} \text{ cm}^{-3}$ at $X = 1$ GPa and $T = 85$ K. 1 – α_{11} , 2 – α_{21} , 3 – α_{22} , 4 – α_{33} .
○ are for experimental data, the solid and dashed lines – for calculated data.

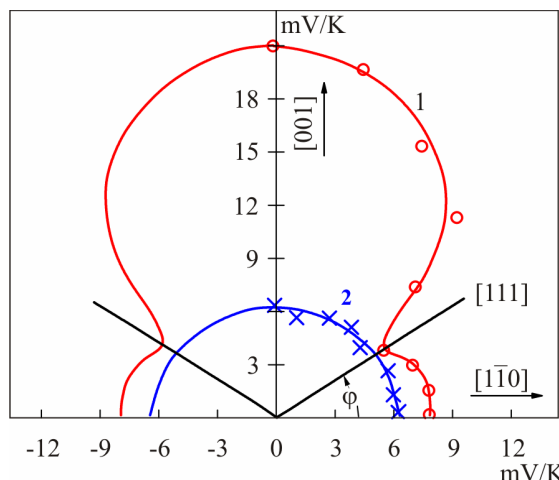


Fig. 4. Angular dependences of the drag piezothermoEMF $\alpha_{11} = f(\gamma)$ measured on strained (at $X = 0.8$ GPa – dependence 1) and unstrained ($X = 0$ – dependence 2) $n\text{-Si}$ crystals with $n_e = 6.55 \cdot 10^{14} \text{ cm}^{-3}$ at $T = 85$ K. ○, × – experimental results.

Using of microlevel anisotropic characteristics of multi-valley semiconductors for describing the macrolevel anisotropy of decisive importance are not only detail studies on the mechanisms of

origination of thermoEMF anisotropy within the microtheory, but also revealing the properties of transformation and total manifestation of anisotropies appeared on different levels, depending on crystal symmetry and its change due to the influence of external effects that have the assigned axial orientation (X , H , etc.).

Fig. 5 presents the results of measuring $\alpha_{ik}^{ph} / \alpha_0^{ph}$ and ρ_{ik} / ρ_0 versus X that fully confirm formula (19).

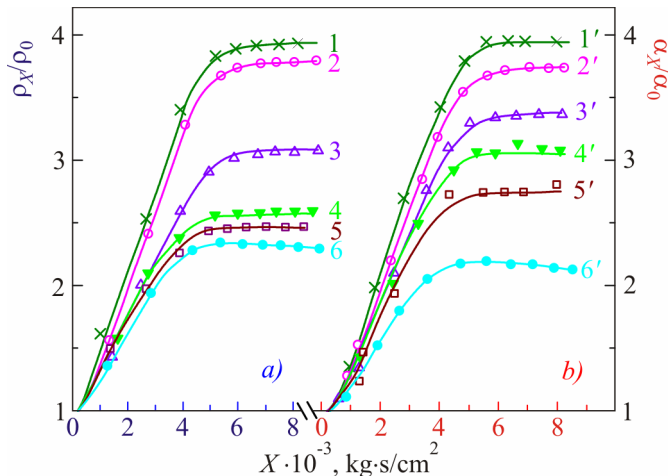


Fig. 5. Dependences of ρ_{11}/ρ_0 (dependence 1–6) and α_{11}/α_0 (dependence 1'–6') at $T = 85$ K on the value of $\vec{X} \parallel \vec{J}$, $\nabla T \parallel [001]$ for n -Si crystals with different concentration of electrons n_e , cm^{-3} :
 1 – $1.9 \cdot 10^{13}$, 2 – $1.29 \cdot 10^{14}$, 3 – $6.55 \cdot 10^{14}$, 4 – $2 \cdot 10^{15}$, 5 – $6.21 \cdot 10^{15}$, 6 – $2.6 \cdot 10^{16}$.

Thermomagnetic effects in semiconductors

Let us consider the thermoelectric properties of multi-valley semiconductors that are in a magnetic field. First of all we will study the symmetry properties of thermomagnetic sensor $\hat{\alpha}(\vec{H})$ in one valley. In semiconductors with a standard c -band (one valley, isotropic effective mass) components of the thermoelectric tensor in magnetic field $\hat{\alpha}(\vec{H})$ are interrelated by symmetry relations

$$\alpha_{ik}(\vec{H}) = \alpha_{ki}(-\vec{H}), \quad (21)$$

established by Onsager. We will show that due to the anisotropy of the energy spectrum of carriers the relation (21) in the presence of \vec{H} is not fulfilled. This gives rise to two points that are of basic importance, namely on the form of commutation relations that would replace (21), as well as on possible creation of conditions that assure realization of these relations. For further consideration it is convenient to present tensor $\hat{\alpha}(\vec{H})$ as a sum of paired $(\hat{\alpha}^+(\vec{H}))$ and unpaired $(\hat{\alpha}^-(\vec{H}))$ in magnetic field parts and to dwell on each of them separately.

Let us introduce a variable

$$\hat{\Delta}(\vec{H}) = \hat{b}(\vec{H})\hat{\rho}(\vec{H}) - \hat{\rho}(-\vec{H})\hat{b}(-\vec{H}) \quad (22)$$

or

$$\Delta_{ik}(\vec{H}) = \alpha_{ik}(\vec{H}) - \alpha_{ki}(-\vec{H}), \quad (23)$$

that will be called the measure of commutation effect.

It turns out that

$$\hat{\Delta}^+(\vec{H}) = \frac{k}{e} (\hat{\mathcal{H}} \hat{I}_3 - \hat{I}_3 \hat{\mathcal{H}}) F_+(\vec{H}), \quad (24)$$

where

$$\mathcal{H}_{ik} = h_i h_k, \quad \vec{h} = \frac{\hat{H}}{H}, \quad (\hat{I}_3)_{ik} = \delta_{i3} \delta_{k3},$$

and function $F_+(\vec{H})$ depends on scattering mechanisms. In the case of power dependence $\hat{\mu}(\mathcal{E})$ the function $F_+(\vec{H}) \sim \frac{K-1}{K}$. For the unpaired in \vec{H} part of tensor $\hat{\Delta}(\vec{H})$ the following relation will be valid

$$\hat{\Delta}^-(\vec{H}) = \frac{k}{e} [\hat{I}_3 (\hat{e} \vec{h}) - (\hat{e} \vec{h}) \hat{I}_3] F_-(\vec{H}) + \frac{k}{e} (\hat{\gamma} + \hat{\tilde{\gamma}}) f(\vec{H}), \quad (25)$$

where $\gamma_{ik} = \begin{vmatrix} h_1 h_2 h_3 & h_2^2 h_3 & 0 \\ -h_1^2 h_3 & -h_1 h_2 h_3 & 0 \\ 0 & 0 & 0 \end{vmatrix}$; \hat{e} is anti-symmetric Levi-Chivita pseudotensor of rank three; $\hat{\tilde{\gamma}}$ is a matrix transposed to $\hat{\gamma}$; $F_-(\vec{H})$ and $f(\vec{H})$ are known functions (combinations of average products) [6].

Assuming that $\hat{\mu}(\mathcal{E})$ has the form of (4) (that is, scattering is anisotropic), then $f(\vec{H}) \neq 0$, and it means that even the value of diagonal components of the tensor $\hat{\alpha}(\vec{H})$ depends on the sign (i.e., direction) of a magnetic field, and it is caused by anisotropic scattering.

In the case when $\hat{\mu}(\mathcal{E})$ is described by power dependence, the function $f(\vec{H}) = 0$, and for the electron part of $\hat{\alpha}(\vec{H})$ the following relations are valid:

$$\left. \begin{aligned} \alpha_{31}(-\vec{H}) &= K \alpha_{13}(\vec{H}) \\ \alpha_{32}(-\vec{H}) &= K \alpha_{23}(\vec{H}) \end{aligned} \right\}, \quad (26)$$

and the other components meet the symmetry relation (21).

In the region of electron-phonon drag the proportionality factor in commutation relations of the type (26) is equal to K/K_j , where $K_j = \frac{\alpha_{\parallel}^{(j)}}{\alpha_{\perp}^{(j)}}$ is the anisotropy parameter of the drag thermoEMF caused by the drag of electrons by polarization phonons j .

The above peculiarities of tensor $\hat{\alpha}$ in one valley, no doubt, should be also exhibited in the case of a multi-valley semiconductor located in a magnetic field, the more so in the presence of uniaxial elastic strain. Moreover, in a semiconductor with several valleys the multi-valley effects should be exhibited as well (in addition to the above peculiarities).

Let us consider those of them which vividly illustrate the role of micro- and macrolevel anisotropy (mobility and drag thermoEMF) under the influence of macroscopic external effects from magnetic fields and uniaxial elastic deformation. Typical in this respect are unpaired thermomagnetic effects in strained semiconductors of cubic symmetry in a weak magnetic field.

Let us consider as an example the strained *n*-Ge and *n*-Si. For a linear dependence $\hat{\alpha}^-(\vec{H})$ it can be written

$$\hat{\alpha}^-(\vec{H}) = -\hat{N}\vec{H}, \quad (27)$$

where \hat{N} is a generalized Nernst-Ettingshausen tensor (nonsymmetrical pseudotensor of rank three). Let us separate from tensor \hat{N} the anti-symmetrical and symmetrical parts, that is, present the tensor in the form

$$\hat{N} = \hat{e}\hat{Q} + \hat{S}. \quad (28)$$

Then, with regard to (27) and (28), the Nernst-Ettingshausen field

$$\vec{E}_{N-E} = [\hat{Q}\vec{H}, \nabla T] - \hat{S}\vec{H}\nabla T. \quad (29)$$

The presence of other summand in expression (29) means that the field \vec{E}_{N-E} is not perpendicular to vectors \vec{H} and ∇T . A deviation of field \vec{E}_{N-E} from the perpendicular in the plane that passes through \vec{H} and ∇T , occurs in the case when tensor \hat{Q} is nonsymmetrical. Indeed, separating from \hat{Q} the antisymmetrical part and comparing to its dual vector \vec{Q} for which the relation $Q_i = \frac{1}{2}e_{ikl}Q_{kl}^a$ is valid, expression (29) can be written as

$$\vec{E}_{N-E} = [\hat{Q}^s\vec{H}, \nabla T] + [[\vec{Q}\vec{H}]\nabla T] - \hat{S}\vec{H}\nabla T.$$

It turns out that in elastically strained *n*-Ge and *n*-Si both vector \vec{Q} and tensor \hat{S} are different from zero, the tensor \hat{S} describing the so-called commutation effect for the nondiagonal components of the tensor of thermoEMF which is reflected in the fact that under conditions when a magnetic field is not directed along the principal ellipsoid axis and does not lie in the plane which is perpendicular to it, $\alpha_{ik}(\vec{H}) \neq \alpha_{ki}(-\vec{H})$. If we introduce the measure of commutation effect

$$\Delta_{ik}^-(\vec{H}) = \alpha_{ik}^-(\vec{H}) - \alpha_{ki}^-(-\vec{H}),$$

then

$$\hat{\Delta}^-(\vec{H}) = 2\hat{S}\vec{H}.$$

Dissimilarity from zero of vector \vec{Q} is a direct consequence of the multi-valley character of semiconductor ($Q_i \sim \Phi$), since for $\vec{Q} \neq 0$ it is necessary that the Brillouin zone be characterized at least by three groups of nonequivalent valleys.

A basically different situation will be created when in quadratic with respect to components of vector \vec{H} approximation the strain nonequivalence of valleys will be imposed by the nonequivalence due to distinctions in the orientation of vector \vec{H} with respect to the principal axes of mass ellipsoids (orientation nonequivalence). Under these conditions, one can introduce the tensor

$$\hat{U} = \sum_{k=1}^s \bar{n}_k \hat{Q}^{(k)},$$

which is the analog of tensor \hat{C} , and the value

$$\bar{n}_k = n_k \operatorname{Sp} \hat{a}^{(k)} \hat{\mathcal{H}}$$

can be referred to as parameter of nonequivalence of k -th valley (in low-intensity magnetic fields). From the designation of tensor \hat{U} it follows that it does not degenerate into a scalar even in the absence of strain. It means that in quadratic with respect to H_i approximation the thermomagnetic effect (even in unstrained multi-valley semiconductors) should exhibit tensor properties. Exactly this accounts for the origination of paired Nernst-Ettingshausen effect and paired thermomagnetic analog of the Grabner effect, anticipated and experimentally measured in [7, 8].

However, under conditions in hand (i.e. at $X=0$) the relation $\alpha_{ik}(\vec{H})=\alpha_{ki}(-\vec{H})$ is still met. And it is violated at $X \neq 0$ (i.e. in the presence of strain). Here it should be noted that even in the absence of strain (i.e. at $X=0$), if in the expansion in H_i of tensor $\hat{\alpha}(\vec{H})$ we consider higher than quadratic terms, then the nonequivalence of valleys in a magnetic field ($\vec{H} \neq 0$) leads to origination of new effects, such as unpaired thermomagnetic analog of the Grabner effect, commutation effect, etc.

In a classically strong magnetic field a parameter of the nonequivalence of the valleys

$$\bar{n}_k = \frac{n_k}{1 + (K-1) \operatorname{Sp} \hat{a}^{(k)} \hat{\mathcal{H}}}$$

more drastically depends on the anisotropic characteristics of a semiconductor on the microlevel, so the thermomagnetic effects on the macrolevel in this case are characterized by the most pronounced anisotropy. Moreover, planar thermomagnetic effects arise in a classically strong magnetic field [9].

It should be noted that the nonequivalence of valleys caused by strain introduces even qualitative changes into the field dependence of thermomagnetic coefficients. For this same reason the thermomagnetic analog of the Grabner effect or the longitudinal Nernst-Ettingshausen effect under strong uniaxial elastic strain in a classically strong magnetic field essentially depends on the value of anisotropy parameter of the drag thermoEMF M (the electronic part of these effects is equal to zero). Moreover, the efficiency of electron drag by polarization phonons j depends differently on the value of mechanical strain X for phonons of different polarizations, which, if necessary, can be rather reliably substantiated.

The anisotropic thermoelectric effects (for instance, thermoEMF anisotropy in a multi-valley semiconductor of cubic symmetry under uniaxial elastic strain) are due to the deformation nonequivalence of valleys. In a classically strong magnetic field due to "magnetic" (or orientation) nonequivalence, there arises a longitudinal Nernst-Ettingshausen effect in a longitudinal magnetic field. Both in the former and the latter cases the same reasons bring about a change in resistivity.

Research on thermoEMF in semiconductors (as in metals) is inseparably related to the use of temperature gradient. As long as it is impossible to grow ideally homogeneous crystals (without any inhomogeneities in the volumetric distribution of doping and residual impurities and free from inhomogeneous distribution of internal mechanical strains), the question now arises as to whether it is possible to use a relation of thermoEMF tensor $\hat{\alpha}$ (or drag thermoEMF anisotropy $\Delta\alpha$) to a change in some less sensitive to the presence of parameter impurity inhomogeneities for a more detailed study of $\hat{\alpha}$ (or $\Delta\alpha$) according to a change in selected parameter.

As is shown by theory [2], for the case of strain nonequivalence of valleys in a multi-valley semiconductor (of $n\text{-Si}$ or $n\text{-Ge}$ type) caused by directional pressure, as well as for the case of "magnetic" (or orientation) nonequivalence of valleys (due to the use of an external magnetic field),

between the relative changes in electron-phonon drag thermoEMF ($\Delta\alpha^{ph}/\alpha_0^{ph}$) and resistivity ($(\Delta\rho/\rho_0)$ there is a linear relationship:

$$\frac{\Delta\alpha^{ph}}{\alpha_0^{ph}} = \frac{M-1}{K-1} \cdot \frac{3K}{2K+M} \cdot \frac{\Delta\rho}{\rho_0},$$

where

$$K = \frac{\mu_{\perp}}{\mu_{\parallel}} = \frac{3}{2} \frac{\rho_{\infty}}{\rho_0} - \frac{1}{2},$$

$$M = \frac{\alpha_{\parallel}^{ph}}{\alpha_{\perp}^{ph}} = \frac{2K}{(2K+1)\frac{\alpha_0^{ph}}{\alpha_{\infty}^{ph}} - 1} = \frac{2K}{(2K+1)\frac{\alpha_0 - \alpha_{(6)}^e}{\alpha_{\infty} - \alpha_{(2)}^e} - 1},$$

and the differences $\alpha_0 - \alpha_{(6)}^e = \alpha_0^{ph}$ and $\alpha_{\infty} - \alpha_{(2)}^e = \alpha_{\infty}^{ph}$ are used to mean the phonon components of the electron-phonon drag thermoEMF in an unstrained and in a heavily strained *n-Si* crystal, respectively.

For a practical use of thermoelectric characteristics of material one should not only know some of thermoEMF components, but have at one's disposal information on the thermoEMF anisotropy $\Delta\alpha$, typical of this material (if it is thermoelectrically anisotropic) or induced due to unidirectional elastic deformation or classically strong magnetic field.

In the case of multi-valley semiconductors (of the type *n-Ge* or *n-Si*), having the values of phonon components of thermoEMF for the unstrained (α_0^{ph}) and heavily strained crystal (α_{∞}^{ph}), as well as the values of the anisotropy parameters K and M , one can also calculate the thermoEMF anisotropy using the relation

$$\Delta\alpha = \alpha_{\infty}^{ph} \left(1 - \frac{1}{M} \right),$$

or

$$\Delta\alpha = (\alpha_{\infty}^{ph} - \alpha_0^{ph}) \left(1 + \frac{1}{2K} \right).$$

Conclusions

1. A universal relationship between the relative changes in electron-phonon drag thermoEMF $\Delta\alpha^{ph}/\alpha_0^{ph}$ and resistivity $\Delta\rho/\rho_0$ in a field of directional pressure or in a classically strong magnetic field has been established.
2. The results obtained are valid not only for conditions of carrier scattering on crystal lattice vibrations, but in the case of mixed scattering (on crystal lattice vibrations and on doping impurities). They also can experience only some quantitative modification, rather than qualitative changes.
3. The calculations cover the cases when under the influence of external effects only inter-minima migration of electrons takes place, but all of them remain in conduction band, i.e. neither strain nor magnetic carrier "freeze-out" of conduction band is present.
4. Under conditions when a magnetic field \vec{H} is directed at an angle to revolution axis of mass ellipsoid and does not lie in the plane normal to it, the symmetry relations for the nondiagonal components of tensor $\hat{\alpha}(\vec{H})$ even in the case of one valley are not fulfilled and, as a result, a commutation effect $\alpha_{ik}(\vec{H}) \neq \alpha_{ki}(-\vec{H})$ becomes apparent.

5. Significant role of scattering anisotropy in a one-valley semiconductor causes a dependence of the value of diagonal components of the tensor $\hat{\alpha}(\vec{H})$ on magnetic field direction, and in the presence of several valleys the multi-valley effects also make their contribution to the considered effect for the diagonal components.

References

1. L.I. Anatychuk, L.N. Vikhor. *Thermoelectricity, Vol. IV, Functionally Graded Thermoelectric Materials* (Chernivtsi: Bukrek, 2012), 180 p.
2. L.I. Anatychuk, *Thermoelements and Thermoelectric Devices. Handbook* (Kyiv: Naukova Dumka, 1979), 767 p.
3. P.I. Baranskii, I.S. Buda, and I.V. Dakhovsky, *Theory of Thermoelectric and Thermomagnetic Effects in Anisotropic Semiconductors* (Kyiv: Naukova Dumka, 1987), 272 p.
4. A.G. Samoilovich, M.V. Nitsovich, and V.M. Nitsovich, On the Theory of Anisotropic Thermoelectric power in Semiconductors, *Phys. Stat. Sol. (b)* **16** (2), 459 – 465 (1966).
5. A.G. Samoilovich, I.Ya. Korenblit, I.V. Dakhovsky, and V.D. Iskra, Anisotropic Scattering of Electrons on Ionized Impurities and Acoustic Phonons, *Physics of the Solid State* **3** (11), 3285 – 3298 (1961).
6. I.S. Buda, P.I. Baranskii, and V.S. Borenko, Effect of Connections in Uniaxially Deformed *n*-Silicon and *n*-Germanium, *Semiconductors* **20** (2), 221 – 226 (1986).
7. P.I. Baranskii, I.S. Buda, and V.V. Savyak, *Thermoelectric and Thermomagnetic Effects in Many-Valley Semiconductors* (Kyiv: Naukova Dumka, 1992), 268 p.
8. P.I. Baranskii, I.S. Buda, V.V. Kolomoyets, B.A. Sus', and V.V. Chernysh, Piezothermomagnetic Analog of Grabner Effect in *n*-Ge, *Semiconductors* **10** (1), 172 – 174 (1976).
9. P.I. Baranskii, I.S. Buda, I.V. Dakhovskii, and A.G. Samoilovich, Galvanothermomagnetic Effects in Anisotropic Media, *Phys. Stat. Sol. (b)* **67** (1), 291 – 299 (1975).
10. A.C. Beer, *Galvanomagnetic Effects in Semiconductors (Eds. F. Seitz and D. Turnbull), Suppl. 4. Solid State Physics* (New York and London: Academic Press Inc., 1963), 418 p.

Submitted 21.01.2014.

D.M. Freik¹, I.I. Chavyak¹, V.I. Makovishin¹, I.A. Arsenyuk²

¹Vasyl Stefanyk Precarpathian National University, 57, Shevchenko Str., Ivano-Frankivsk, 76018, Ukraine;

²Ivan Ohienko Kamyantsev-Podilsky National University, 61, Ohienko Str., Kamyantsev-Podilsky, 32300, Ukraine

THERMOELECTRIC VAPOUR-PHASE CONDENSATE OF P-TYPE TIN TELLURIDE

Structural and thermoelectric properties of p-SnTe thin films of different thickness $d = (40 - 800)$ nm, prepared by vapour condensation in open vacuum on fresh cleavages (0001) of muscovite mica have been investigated. Based on the statistical analysis of the experimental results, increase in conductivity σ , carrier mobility μ and some reduction of the Seebeck coefficient S and the hole concentration p with growing condensate thickness d has been established. It has been shown that maximum specific thermoelectric power $S^2\sigma$ is $\sim 18 \mu W/K$, which is important for creation of p-legs of thermoelectric micromodules. The stable p-type conductivity has been attributed to tin vacancies in the cation sublattice of SnTe crystal structure.

Key words: thin films, tin telluride, structure, thermoelectric properties, defects.

Introduction

Tin telluride $SnTe$ is a narrow-gap ($E_{g300K} \approx 0.2$ eV) semiconductor whose homogeneity region is fully displaced towards chalcogen, which is responsible for high carrier concentration ($\sim 10^{20} \text{ cm}^{-3}$) and stable p-type conductivity (Fig. 1 a) [1-2]. $SnTe$ is crystallized in $NaCl$ structure whose lattice parameter within the homogeneity region (50.1 – 50.9) at.% Te is reduced (Fig. 1 b) [2-4]. It is established that the predominant defects in $SnTe$ crystals are tin vacancies V_{Sn} of different ionization degrees (V_{Sn}^{2-} , V_{Sn}^{4-}). Recalculation of current carrier concentration p into atomic fraction of superstoichiometric tellurium can be done according to relationship [1]:

$$(X_{Te} - 0.5 = nM / 4Z\rho N) \approx 7.9325 \cdot 10^{-24} p, \quad (1)$$

where M is the molar mass of $SnTe$, Z is ionization degree of point defects, ρ is $SnTe$ density ($\rho = (6.445 \pm 0.01) \text{ g/cm}^3$ at 298 K), N is the Avogadro number.

From the results of calculations [5-6], when a metal is removed from the cation nodes of crystal lattice $SnTe$, it loses four electrons, and the valence band – only one level, thus leaving two vacant states, resulting in the appearance of two holes in the valence band, so tin vacancy V_{Sn} is an effective acceptor.

With this in mind, both pure $SnTe$ [7] and doped with different impurities [8], as well as solid solutions based on tin telluride [3-9, 10] are promising materials for p-legs of thermoelements in the medium temperature range (500 – 750) K. As regards thin-film $SnTe$ structures, they greatly expand the possibilities of practical application [11-13]. This paper presents the results of research on the structure and thermoelectric properties of tin telluride thin films prepared by vapour-phase deposition in vacuum on mica single crystal substrates.

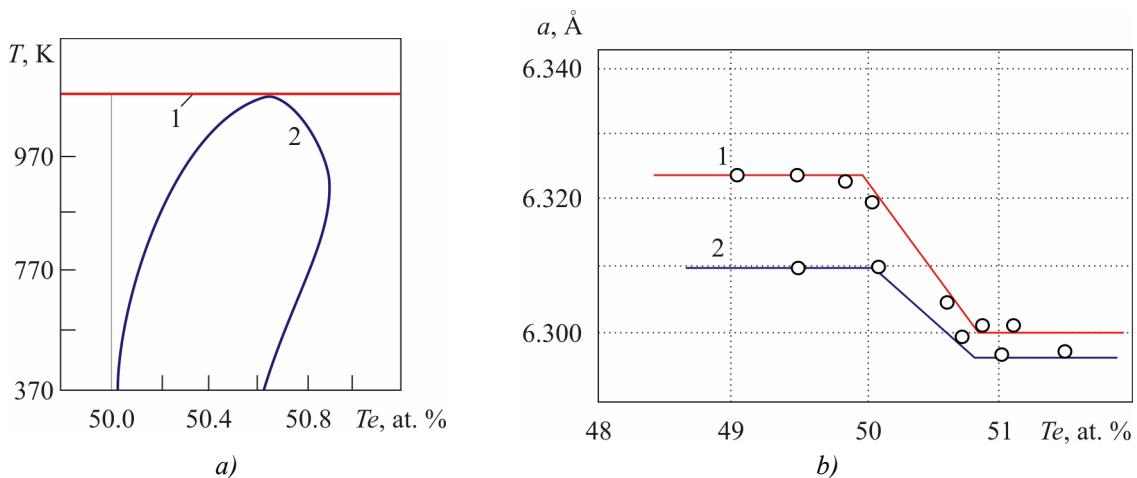


Fig. 1. Homogeneity region boundaries (a): (1 – liquidus, 2 – solidus) and (b): dependences of lattice parameter on tellurium content at T , K: 1 – 673; 2 – 973 in tin telluride (b) [1].

1. Experimental procedure

To obtain a condensate of different thickness d at the assigned deposition temperature T_n , use was made of a vacuum sectional heater with five micro heaters made of vacuum copper rods of size $40 \times 20 \times 8 \text{ mm}^3$ with openings provided for ceramic tubes with heating elements (Fig. 2). From the bottom of the case there is a platform with supports for the substrate. To reduce thermal losses from the surfaces of substrates and to shape the condensate, tantalum screens 0.3 mm thick were installed. All micro heaters were calibrated for equal temperature by selecting the resistance of nichrome wire of diameter 0.3 mm. Heater temperatures are measured by “chromel-copel” thermocouples placed in their cases close to substrates. A system of micro heaters is diagonally fixed to swinging arm, and heating elements are connected in parallel (Fig. 2).

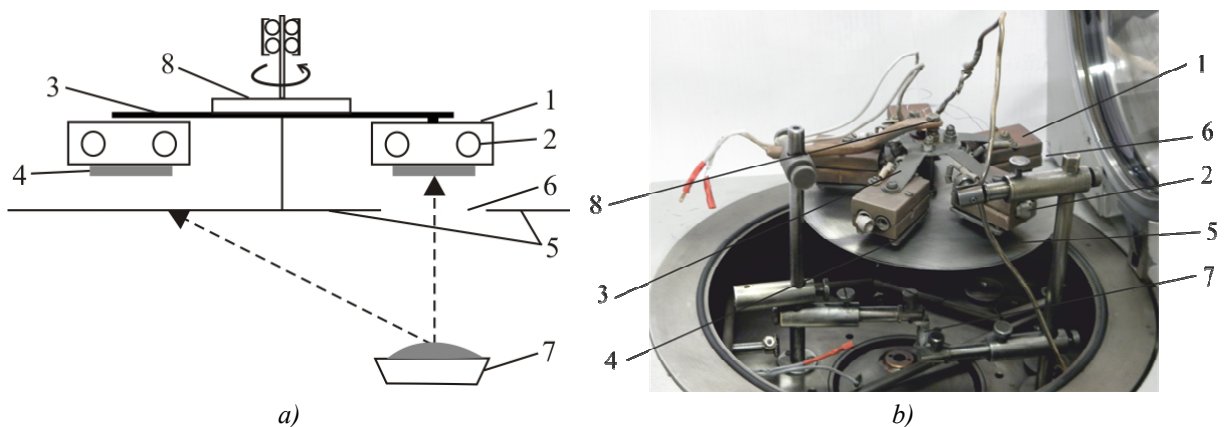


Fig. 2. Structural scheme (a) and picture (b) of sectional heater for preparation of vapour-phase films and nanostructures: 1 – micro heater system, 2 – heaters, 3 – radial arms, 4 – supports for vapour deposition, 5 – gate, 6 – asymmetrically arranged opening, 7 – evaporator, 8 – mechanical microheater pivot system.

Vapour-phase condensates are prepared in the following way (Fig. 2): evaporator 7 is loaded with a weight of substance under study (powder of synthesized tin telluride compound); prepared substrates 4 (fresh mica cleavages) are placed into heaters 1; with closed gate 5 micro heaters 1 with substrates 4 and evaporator with weight 7 are heated to assigned temperature; one of the heaters is brought under opening 6 in the gate above evaporator 7 and vapour is deposited on the substrate for a

certain fixed period; then vapour flow from the evaporator is closed with the gate, the next of sectional micro heaters with a substrate is pivoted, the gate is opened and deposition of a different duration is performed. The above process is repeated five times for each micro heater with substrates.

In our case, *SnTe* vapour was deposited on fresh cleavages (0001) of muscovite mica at weight evaporation temperature $T_e = 870$ K, the temperature of substrates (deposition) $T_s = 470$ K and different deposition periods $\tau = 5 - 360$ s, which assured condensate thicknesses within $d = 40 - 800$ nm.

The obtained nanostructures were studied by atomic force microscopy (AFM) methods Nanoscope 3a Dimension 3000 (Digital Instruments USA) in periodic contact mode. Measurements were performed in the central part of the samples using serial silicone probes NSG-11 with a nominal edge bending radius to 10 nm (NT0MDT, Russia). According to the results of AFM studies of vapour-phase condensates, the surface morphology and its profilographs were determined.

The electric parameters of films were measured in the air at room temperatures in constant magnetic fields on the elaborated automated installation that provides for measurement of electric parameters, as well recording and primary data processing, with the possibility of constructing the plots of temporal and temperature dependences. The sample under measurement had four Hall and two current contacts. As the ohmic contacts, silver films were used. Current through the samples was ≈ 1 mA. The magnetic field was directed normal to the surface of films at induction 1.5 T.

The results of AFM studies and the thickness dependences of electric conductivity σ , the Seebeck coefficient S and thermoelectric power $S^2\sigma$, as well as the Hall coefficient R_H , hole concentration p and their mobility μ for *p-SnTe* films are depicted in Fig. 3 – 4.

2. Experimental results and their analysis

2.1. Condensate structure

Analysis of AFM-studies (Fig. 3) indicates that deposition temperature T_s and deposition time τ are important technological factors that determine the mechanisms of *SnTe* nanocrystals growth on cleavages (0001) of muscovite mica with vapour deposition in open vacuum, their topology and dimensions. The general symptom, under conditions of optimal evaporation temperatures $T_e = 870$ K and deposition temperature $T_s = 470$ K, is the fact that with increasing the deposition time τ (thickness d), the shape and dimensions of individual nanoformations are changed (Fig. 3). Thus, in particular, individual nanoformations are formed with a tendency to cubic forms with lateral dimensions growing with increase in deposition time from ~ 250 nm ($\tau = 5$ s) to ~ 400 nm at $\tau = 10$ s and ~ 700 nm at $\tau = 210$ s, respectively (Fig. 3). In so doing, the height of nanostructures is reduced from ~ 25 nm to 18 and 9 nm, respectively for $\tau = 5$, 10 and 210 s (Fig. 3-II). The most pronounced cubic form of nanostructures takes place at deposition time $\tau = 10$ s (Fig. 3-I, b). In so doing, during the late growth stages there is a predominant orientation of nanocrystals with cube edges {100} parallel to substrate surface and their considerable disorientation (Fig. 3-I). However, during the initial growth stages there is orientation effect of substrate which causes formation of pyramidal structures with typical orientation (111) of *SnTe*(0001) mica (Fig. 3-1, a).

Note that with the heteroepitaxial growth there are three different nucleation mechanisms [14]: the Frank-van der Merve mechanism, when layer-by-layer (two-dimensional) material growth of condensate *B* takes place on substrate *A*; the Volmer-Weber mechanism, when island-type (three-dimensional) growth of *B* takes place on the open surface of substrate *A*; the Stransky-Krastanow mechanism, when, at first, layer-by-layer growth of *B* on *A* is realized with subsequent formation of three-dimensional islands *B* on the substrate already coated with condensate.

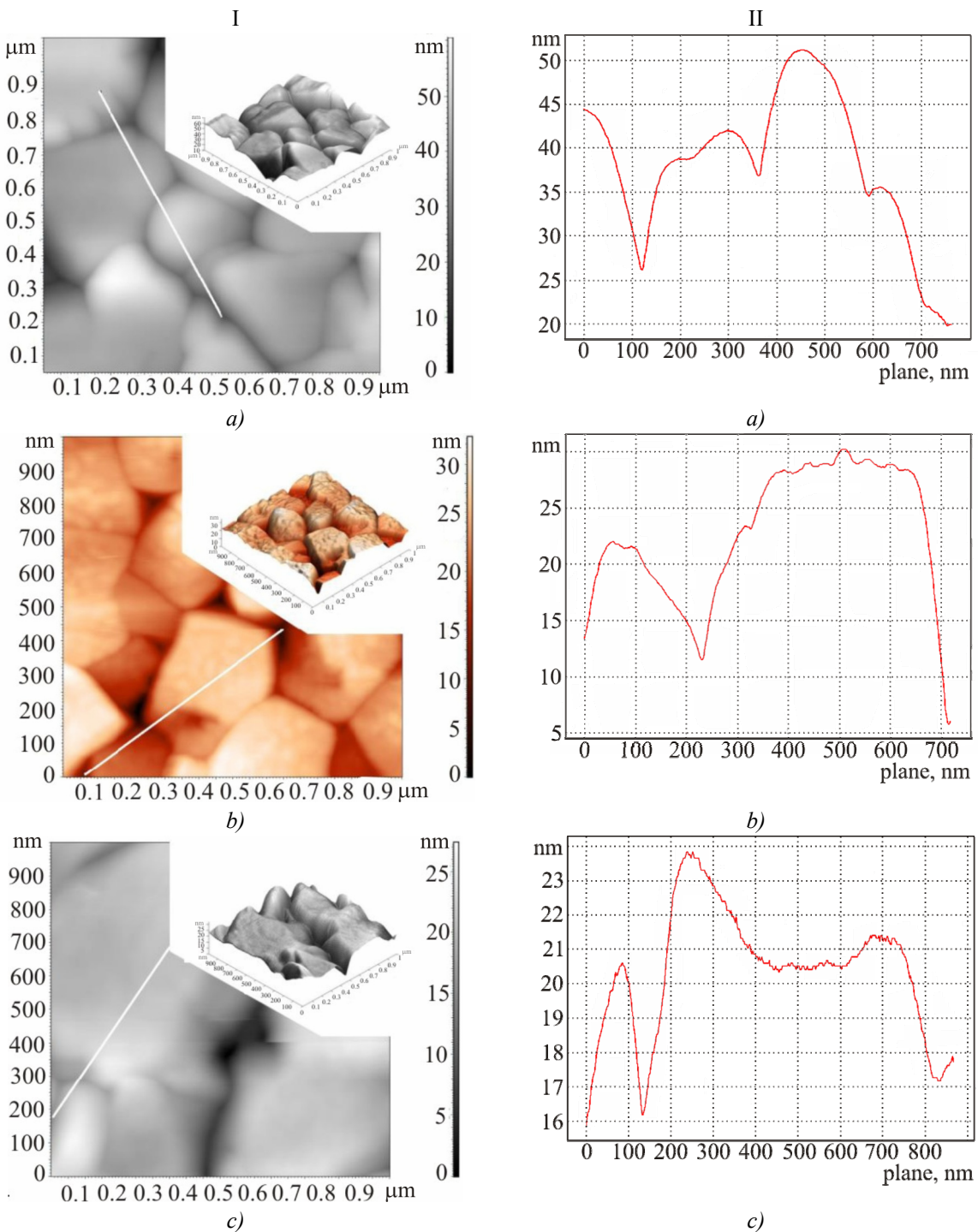


Fig. 3. 2D and 3D AFM images (I) and profilographs (II) of vapour-phase condensates SnTe/(0001) muscovite mica with different vapour deposition times τ, s : a – 5; b – 10; c – 210.

Realization of the former two mechanisms is determined by the energy ratio of the two surfaces (E_B, E_A) and the interface energy E_{BA} . If the sum of surface energy of epitaxial layer E_B and interface energy E_{BA} is smaller than the surface energy of substrate $E_B + E_{BA} < E_A$, that is, when substrate is wetted by condensate, then the Frank-van der Merve mechanism is realized. A change in $E_B + E_{BA}$ value can result in transition from the Frank-van der Merve mode to the Volmer-Weber mode. With certain mismatch in lattice constant between condensate and substrate, there occurs formation of isolated islands through relaxation of elastic stresses which is typical of the Stransky-Krastanow mode.

In our case, the heteroepitaxial growth of $\text{SnTe}/(0001)$ muscovite mica nanostructures is realized by the Volmer-Weber mechanism according to which individual nanocrystals with certain topological architecture are formed (Fig. 3).

2.2. Thermoelectric properties

It has been established that all SnTe films, irrespective of their preparation conditions, are characterized by *p*-type conductivity. In so doing, as is evident from Fig. 4 *a*, with increase in condensate thickness (d), conductivity (σ) increases with attainment of saturation and already at $d \approx 600$ nm reaches considerable values $\sigma = (5 - 8) \cdot 10^3 \Omega^{-1} \text{cm}^{-1}$. The Seebeck coefficient also increases to the value of $S = 70 - 75 \mu\text{V/K}$, but with reduction in condensate thickness $d < 100$ nm (Fig. 4, *b*). Such values cannot be reached for the bulk samples [1]. For thick films it does not depend on thickness and is $S \approx 40 \mu\text{V/K}$. Based on the obtained values of $\sigma(d)$ and $S(d)$ (Fig. 4, *a*, *b*), a dependence of power factor $P = S^2\sigma$ on SnTe thickness in condensate *p-SnTe/(0001)* mica was determined (Fig. 4, *c*). Here also one can see growth of thermoelectric power factor with a decrease in thickness which is $P \approx 18 \mu\text{W/K}^2 \text{cm}$ at $d < 100$ nm (Fig. 4, *c*).

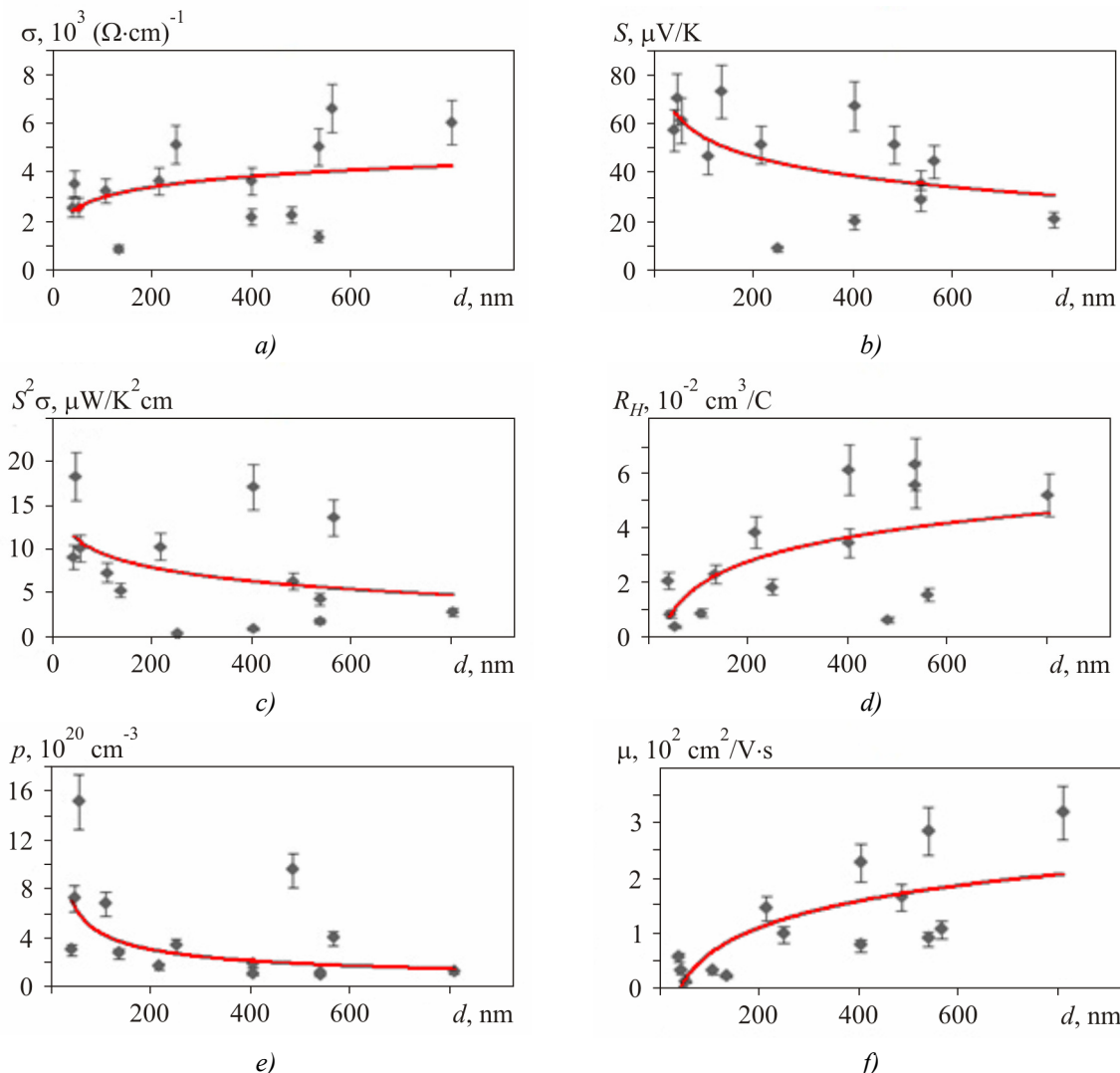


Fig. 4. Dependence of thermoelectric parameters (*a* – electric conductivity σ , *b* – the Seebeck coefficient S , *c* – thermoelectric power $S^2\sigma$, *d* – the Hall coefficient R_H , *e* – carrier concentration p , *f* – mobility μ on the thickness of vapour-phase condensates $\text{SnTe}/(0001)$ muscovite mica.

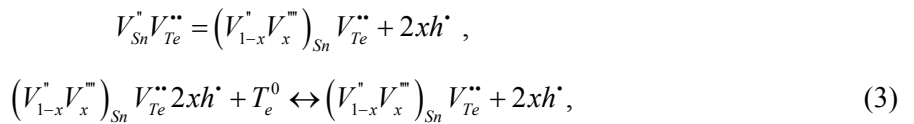
As regards other kinetic coefficients (the Hall concentration p and carrier mobility μ), their thickness dependences have the opposite character of changes: with increase in condensate thickness hole concentration decreases (Fig. 4, c), and mobility increases (Fig. 4,f). Note that the dominant role in the thickness dependence $\sigma(d)$ of condensates is played in our case by mobility ($\sigma = qp\mu$, where q is an elementary charge) (Fig. 4, a,f), rather than by carrier concentration p (Fig. 4, a, e).

3. Crystal chemistry of defective systems

The experimentally observed stable *p*-type conductivity and high intrinsic concentration of charge carriers in vapour-phase nonstoichiometric *p*-SnTe condensate in terms of crystal-chemical approach is related to completion of anion sublattice and formation of tin vacancies V_{Sn} of crystal structure [15]. Thus, in the case of existence of only two-charge tin vacancies V_{Sn}^{2-} crystal-chemical cluster will be presented as



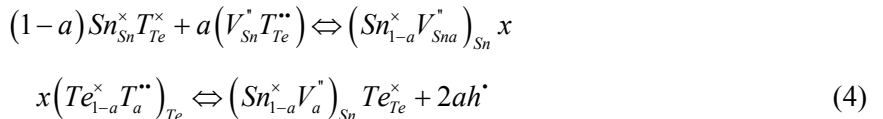
and in the presence of two- V_{Sn}^{2-} and four-charge V_{Sn}^{4-} vacancies



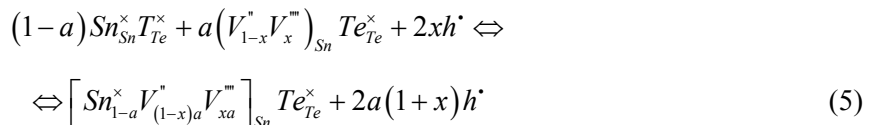
respectively.

Here, “ $\prime\prime$ ”, “ $\bullet\bullet$ ”, “ 0 ” are positive, negative and neutral charges, h^{\bullet} – hole, x – fraction of V_{Sn}^{4-} .

The superposition of the resulting clusters with crystal-chemical formula $Sn_{Sn}^{\times} T_{Te}^{\times}$ yields crystal-quasi-chemical formula of nonstoichiometric tin telluride:



in the first case (2) and



in the second case (3), respectively.

Full electroneutrality equations for crystals with the available charged point defects for (4) and (5) will be as follows:

$$2 \left[V_{aSn}^{2-} \right] = 2ap, \quad (6)$$

and

$$2 \left[V_{(1-x)aSn}^{2-} \right] + 4 \left[V_{xaSn}^{4-} \right] = 2a(1+x)p, \quad (7)$$

respectively.

Here a is a deviation from stoichiometry that corresponds to superstoichiometric tellurium in compound; p is hole concentration, [] are concentrations of respective charged defects.

Calculations performed on the basis of relations (4), (7) indicate that increase in the content of superstoichiometric tellurium in homogeneity region of SnTe compound causes increase in the concentrations of two-charge $[V_{\text{Sn}}^{2-}]$ (Fig. 5, a – curve 1) and four-charge $[V_{\text{Sn}}^{4-}]$ (Fig. 5, a – curve 2) tin vacancies, as well as in hole concentration (Fig. 5, b – curve 1). In so doing, for the values of (50 – 50.4) at.% Te the prevalent mechanism is formation of four-charge vacancies $[V_{\text{Sn}}^{2-}]$ (Fig. 5, b – curve 2), which is also indicated by drastic increase in the number of carriers which falls on one tin vacancy ($Z = p/[V_{\text{Sn}}]$) (Fig. 5, b – curve 2). In the concentration range (50.4 – 50.9) at.% Te the dominant process is formation of two-charge tin vacancies $[V_{\text{Sn}}^{2-}]$ (Fig. 5, a – curve 1), and the value Z varies only slightly (Fig. 5, b – curve 2).

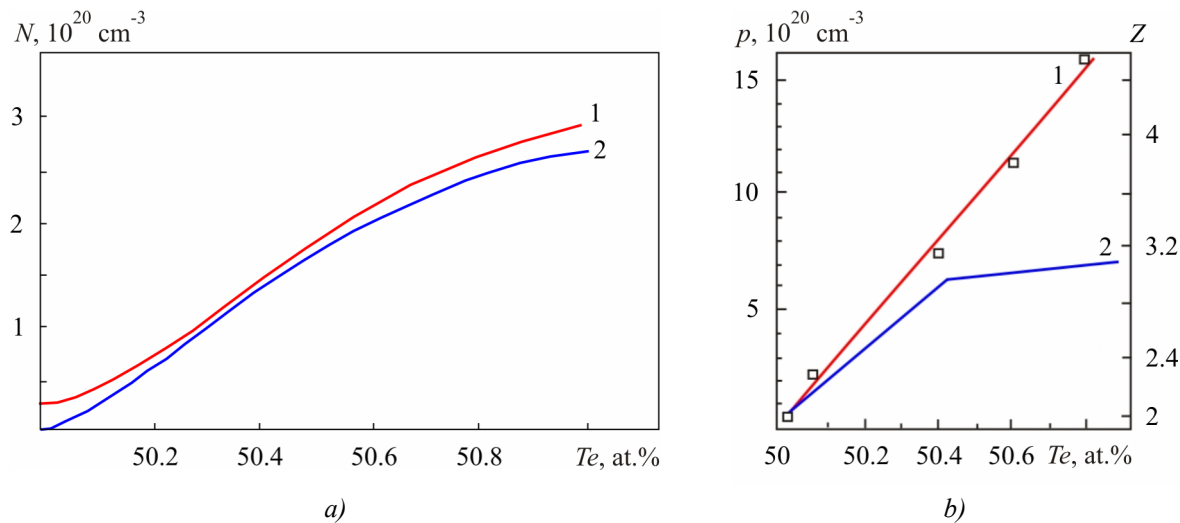


Fig. 5. Dependences a): of two-charge 1 – $[V_{\text{Sn}}^{2-}]$, four-charge 2 – $[V_{\text{Sn}}^{4-}]$ tin vacancies and b): 1 – hole concentration p and carrier number per one tin vacancy Z on tellurium content for SnTe crystals.

With regard to the foregoing, it can be unambiguously asserted that the intrinsic hole concentration in vapour-phase condensates $p\text{-SnTe}$ is due to a defective subsystem of crystalline structure, namely cation vacancies V_{Sn} . The experimentally observed reduction of carrier concentration with thickness increase (Fig. 4, e) can be also due to a change in the value of superstoichiometric tellurium, namely its reduction during evaporation of weight in the evaporator. The latter leads to prevalence of two-charge tin vacancies V_{Sn}^{2-} over tetravalent V_{Sn}^{4-} (Fig. 5, a), which is the reason for the Hall concentration decrease.

Conclusions

1. Results of research on the structure and thermoelectric properties of $p\text{-SnTe}$ thin films of different thickness (40 – 800) nm deposited in open vacuum on fresh cleavages (0001) of muscovite mica are presented.
2. It is shown that vapour-phase condensate is formed by the Volmer-Weber mechanism with formation of individual clusters with (100) and (111) orientations of $\text{SnTe}/(0001)$ muscovite mica.
3. The thickness dependences of thermoelectric parameters of condensates have been determined. High values of the Seebeck coefficient ($S \approx 70$) $\mu\text{V/K}$ and thermoelectric power $S^2\sigma \approx 18 \mu\text{W/K}^2\text{cm}$ have been revealed that are much in excess of similar parameters for the bulk crystals.

4. The stable *p*-type conductivity and high hole concentration ($10^{20} - 10^{21}$) cm⁻³ has been explained by formation of two-charge and four-charge cation vacancies (V_{Sn}^{2-}, V_{Sn}^{4-}) caused by deviation from stoichiometry towards tellurium.

The work has been performed in the framework of research projects of the NAS Ukraine (registration number 0113U000185), State Foundation for the Basic Research of the Ministry of Education and Science of Ukraine (registration number 0113U003689, and NATO's Public Diplomacy division according to "Science for Peace" program (NUKR, SEPP 984536).

References

1. V.M. Shperun, D.M. Freik, V.V. Prokopiv, *Tin Telluride, Physical and Chemical Properties*, Ed. by D.M. Freik (Ivano-Frankivsk: Plai, 2002), 152 p.
2. R.Kh. Achkurin, V.B. Ufimtsev, Calculation of the Boundaries of Homogeneity Range of Lead and Tin Tellurides, *Russian Journal of Physical Chemistry* **53** (6), 1441 – 1445 (1979).
3. N.Kh. Abrikosov, V.F. Bankina, L.V. Poretskaya., E.V. Skudnova, and S.N. Chizhevskaya, *Semiconductor Chalcogenides and Alloys on their Basis* (Moscow: Nauka, 1975), 219 p.
4. L.E. Shelimova, N.Kh. Abrikosov, *Sn-Te* system in the Region of *SnTe* Compound, *Russian Journal of Inorganic Chemistry* **9** (8), 1879 – 1882 (1964).
5. N.Y. Parada, G.W. Preat, New Model for Vacancy States in *SnTe*, *Phys. Rev. Lett.* **22** (5), 180 – 183 (1969).
6. G.W. Prat, Vacancy and Interstitial States in the Lead Salts, *Y. Nouwetals* **1**, 103 – 109 (1973).
7. E.P. Sabo, Technology of Chalcogenide Thermoelements. Physical Foundations, *J.Thermoelectricity* **4**, 57 – 65 (2003).
8. N.I. Dziubenko, E.I. Rogacheva, V.M. Kosevich, S.A. Laptev, and A.V. Arankin, Effect of Indium, Gallium, Antimony and Bismuth on the Properties of Tin Telluride, *Izvestiya AN SSSR: Inorganic Materials* **19** (9), 1457 – 1461 (1983).
9. N.I. Dziubenko, E.I. Rogacheva, Interaction in *SnTe-GaTe* and *SnTe-Ga₂Te₃* Systems, *Izvestiya AN SSSR: Inorganic Materials* **23** (6), 1736 – 1737 (1987).
10. D.M. Freik, I.M. Ivanishin, Physical and Chemical Properties and Dominant Defects in Crystals of *Sn-Sb-Te*, *Sn-Bi-Te* System, *Physics and Chemistry of Solid State* **7** (3), 289 – 296 (2006).
11. B.S. Dzundza, I.I. Chavyak, A.I. Tkachuk, G.D. Mateik, and O.L. Sokolov, Near-Surface Layers and Profiles of Electrical Parameters of *SnTe* Thin Films, *Physics and Chemistry of Solid State* **11** (3), 614 – 617 (2010).
12. I.K. Yurchishin, I.I. Chavyak, Yu.V. Lisyuk, and L.T. Kharun, Size Effects in Thermoelectric Parameters of Tin Telluride, *Physics and Chemistry of Solid State* **11** (4), 898 – 903 (2010).
13. I.I. Chavyak, Stannum Telluride Nanostructures on Muscovite Mica Cleavages, *Physics and Chemistry of Solid State* **13** (1), 62 – 68 (2012).
14. B.V. Ivansky, *Ostwald Ripening of Nanostructures under Conditions of Diffusion-Wagner Mass Transport Mechanism*, PhD Thesis, Chernivtsi, 2011, 152 p.
15. M.O. Galuschak, D.M. Freik, I.M. Ivanyshyn, A.V. Lisak, and M.V. Pyts, Thermoelectric Properties and Defective Subsystem in Doped Telluride of Tin, *J. Thermoelectricity* **1**, 43 – 51 (2000).

Submitted 06.02.2013.

**G.N. Kozhemyakin¹, S.Ya. Skipidarov², Yu.M. Krutov¹, A.N. Paraschenko¹,
O.N. Ivanov³, O.N. Soklakova³**

¹V. Dahl East-Ukrainian National University, 20 A, Molodyozhny kvartal, Lugansk, 91034, Ukraine;

²Closed JSC “SKTB “NORD”, Ferrotec Corp., 3, Peschanyi kar’er, Moscow, 109383, Russia;

³Belgorod State University, 85, Pobedy Str., Belgorod, 308015, Russia

NANOSTRUCTURED BISMUTH AND ANTIMONY TELLURIDES FOR THERMOELECTRIC HEAT PUMP

The microstructure of p- and n-type bismuth and antimony telluride solid solutions prepared by hot extrusion was investigated. It was shown that the ingots of extruded thermoelectric materials consisted of nanocrystals as big as 8 to 30 nm. The thermoelectric parameters of extruded nanomaterials were measured and microstructure effect on their value was considered. These nanomaterials were used to produce p- and n-type legs to manufacture thermoelectric modules. The efficiency of thermoelectric modules operating as thermoelectric heat pumps in the temperature range of +10 to +45 °C was investigated. Two methods were developed for the measurement of conversion factor of thermoelectric modules. Maximum value of conversion factor reached 6.8 to 8.2 for heat transfer by thermoelectric module at electric power consumption 0.75 W. Electric power increase to 40 W contributed to reduction of conversion factor of thermoelectric modules to 1.8.

Key words: thermoelectricity; bismuth and antimony tellurides; nanocrystals; heat pump; conversion factor; heat transfer.

Introduction

Heat pumps are known to be more efficient than electric heating elements for heating in the temperature range of +10 °C to +40 °C [1]. For space heating at these temperatures heat pumps should possess high efficiency. Typical air heat pumps have conversion factor 3 – 4 when used for space heating in mild climate. However, with ambient temperature reduction to –18 °C the efficiency of heat pump is reduced to 1.0. Evaporative compression refrigeration devices can be used for heat pumps of geothermal systems. Such heat pumps have moving parts, limited service life and create noises. Moreover, for their operation environmentally hazardous coolants are employed.

Thermoelectric heat pumps also can have high conversion factor under special conditions, but without the above drawbacks [2-5]. For commercial use as a heater, conversion factor of thermoelectric heat pump should be more than 5 in the range of room temperatures. Energy conversion efficiency depends on the value of thermoelectric figure of merit $ZT = S^2\sigma T/k$, where Z is figure of merit, S is thermoEMF, σ is electric conductivity, T is absolute temperature and k is thermal conductivity. According to recent results of research [6, 7, 8] on the nanostructured crystalline ingots of p-type $Bi_xSb_{2-x}Te_3$, owing to thermal conductivity reduction the value of ZT has increased from 1.0 to 1.2 at room temperature. On the other hand, ZT for n-type $Bi_2Te_{3-x}Se_x$ has a low value about 0.85, which reduces the device efficiency. The results of this research showed a promising way for increasing the figure of merit ZT of thermoelectric materials and the efficiency of thermoelectric devices. It should be noted that incomplete information in the scientific literature on thermoelectric

heat pumps does not determine clearly enough the prospects of their use for heating systems.

The purpose of this work is to study structural perfection of extruded samples of solid solutions of bismuth and antimony chalcogenides, the effect of structure on the thermoelectric properties and conversion factor in the region of room temperatures. In this paper we present new results of research on the microstructure, thermoelectric properties and conversion factor of thermoelectric modules based on nanostructured *p*- and *n*-type legs that can be employed as heaters in the temperature range of +17 to +45 °C.

1. Experimental procedure

Thermoelement legs were manufactured by extrusion method. Bismuth, antimony, tellurium and selenium of 99.99 % purity were melted and crystallized prior to extrusion in the form of *p*-type $(Bi_2Te_3)_x \cdot (Sb_2Te_3)_{1-x}$ ($x \approx 0.26$ mol.%) and *n*-type $(Bi_2Se_3)_x \cdot (Bi_2Te_3)_{1-x}$ ($x \approx 0.06$ mol.%) ingots. Hot extrusion method was used to produce ingots of these solid solutions of diameter 30 mm according to the technology of SKTB "Nord". Samples in the form of discs 2 mm thick were cut from the ingots perpendicular to ingot axis direction to study their microstructure. The surfaces of discs were ground and polished with abrasive Al_2O_3 having grain size from 200 μm to 40 μm , respectively. After washing in distilled water the samples were etched in 50 % HNO_3 at a temperature about 50 °C for 10 to 15 minutes.

Microcrystals typical of polycrystals were not discovered under optical microscope on the prepared surface of samples of *p*- and *n*-type extruded thermoelectric materials. Therefore, the morphology of samples microstructure was studied under scanning electronic microscope (SEM "Quanta-600 H"). Samples for the measurement of thermoEMF, electric resistivity, thermal conductivity and carrier concentration were cut from ingots shaped as parallelepipeds of size $3 \times 4 \times 23$ mm³ with their larger face oriented parallel and perpendicular to ingot axis. On their larger lateral face in depressions of diameter 0.3 mm and depth 0.4 mm iron-constantan thermocouples were secured whose wire diameter was about 100 μm .

The extruded *p*- and *n*-type ingots of diameter 30 mm were cut into thermoelement legs of size $1.6 \times 1.6 \times 1.6$ mm³ of which thermoelectric modules of series TM-127-1.4-6.0 with the overall dimensions $40 \times 40 \times 3.8$ mm³ were manufactured in SKTB "Nord".

The efficiency of heat transfer by these thermoelectric modules was studied. Conversion factor was measured by two methods under near-adiabatic conditions. Schematic of measurement by the first method using two copper plates is presented in Fig. 1. Heat input and transfer took place through the cold and hot heat spreaders of size $40 \times 40 \times 0.7$ mm³ that are contact surfaces of thermoelectric modules. Heat flux passing through the module was measured through use of two copper plates of size $40 \times 40 \times 10$ mm³.

The two surfaces of each copper plate were pre-polished with abrasive Al_2O_3 of size 40 μm . BeO paste was deposited to assure a reliable thermal contact between ceramic heat spreaders of thermoelectric modules and the surfaces of copper plates. The temperature of copper plates was measured by chromel-alumel thermocouples with the wire diameter 0.5 mm that were secured in the openings of diameter 1.0 mm and depth 1.5 mm on their lateral surfaces. A copper heat sink with running cold water was secured under the lower surface of cooled copper plate. The temperature of the hot upper copper plate was held constant during the experiment due to cooled copper heat sink. The thermoelectric modules and copper plates were thermally insulated with mineral wool. Such device design provided measurement of maximum temperature difference on thermoelectric modules with electric power requirement up to 45 W.

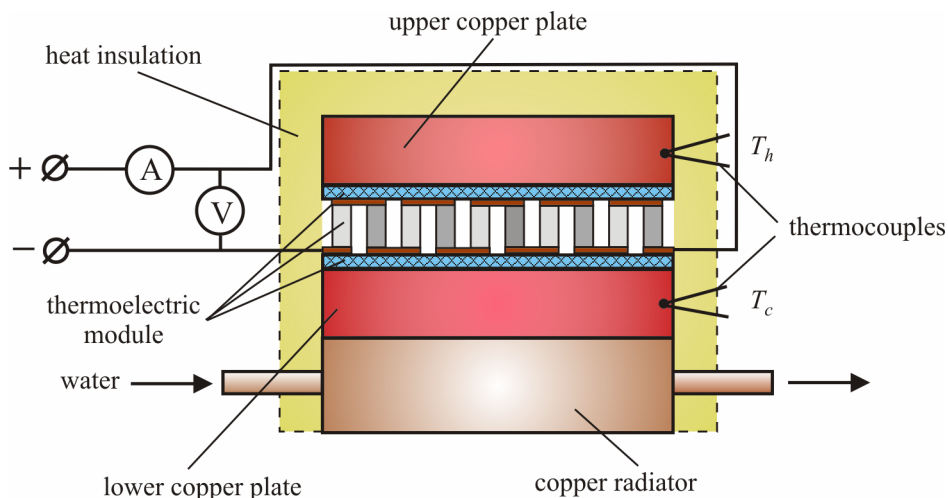


Fig. 1. Schematic of a device for conversion factor measurement by the method using two copper plates.

The second method of conversion factor measurement determined transfer of thermoelectric module heat from the electric heater to the copper plate. A device presented in Fig. 2 was developed for the second method. A thermoelectric module was secured on the electric heater of area $40 \times 40 \text{ mm}^2$ and 2 mm thick. The lower surface of the electric heater rested on a base made of material with low thermal conductivity. One copper plate of size $40 \times 40 \times 10 \text{ mm}^3$ and mass 174 g was used for heat flux measurement. This copper plate was secured on the upper heat spreader of thermoelectric module as an absorber of heat transferred to this module. A reliable thermal contact between the upper heat spreader of thermoelectric module and the copper plate was realized by means of BeO paste. The copper plate temperature was measured by copper-constantan thermocouple with the wire diameter 0.1 mm placed into opening of diameter 0.3 mm and depth 1 mm on the lateral surface of this plate. The air space between the copper plate, thermoelectric module, electric heater and metal case was filled with mineral wool for thermal insulation. Thermal flows from the five surfaces of the copper plate and thermoelectric module were compensated by two external heaters (lateral and upper). Temperature equality between the copper plate surfaces and the metal case walls was controlled by copper-constantan differential thermocouples. The conversion factor was measured 15 to 20 s after the thermoelectric module was switched on.

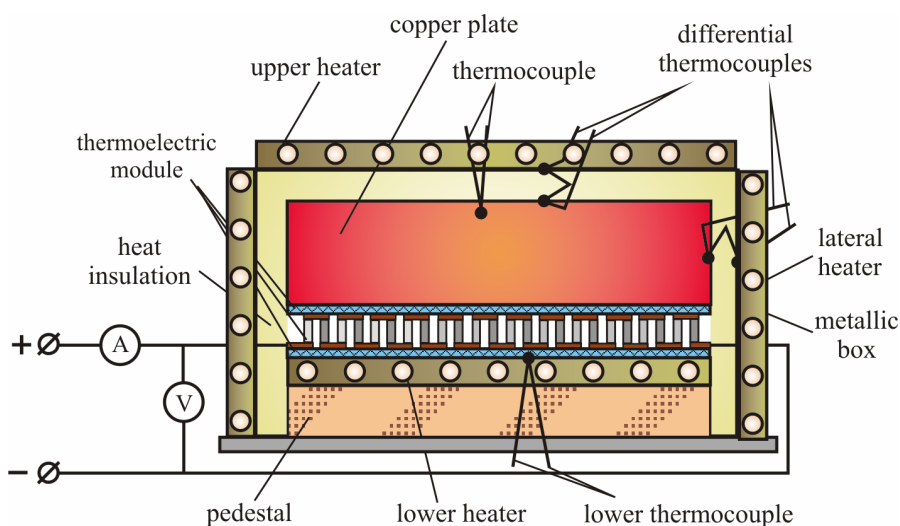
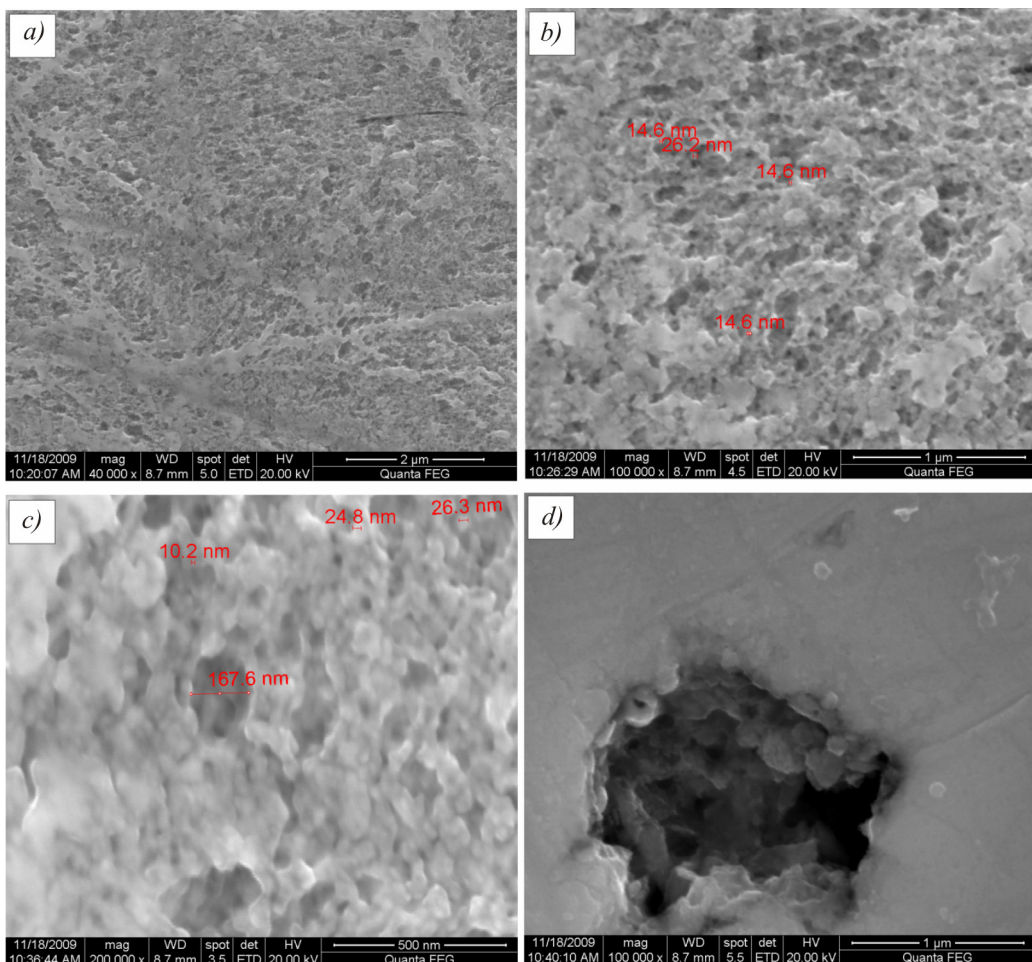


Fig. 2. Schematic of a device for conversion factor measurement by the method using a copper plate and a heater.

2. Structure of materials and their thermoelectric properties

Fig. 3 shows the pictures of structure morphology of *p*-type samples obtained by means of scanning electron microscope.

In *p*-type samples with a small magnification 40000 \times there were uniformly distributed crystallites and pores of size 20 to 260 nm and 60 to 260 nm, respectively (Fig. 3, *a*). The average size of crystallites was 150 nm, of pores – 130 nm. The shape of crystallites and pores was near-spherical. With a larger magnification 100000 \times and 200000 \times the structure morphology had a similar appearance (Fig. 3, *b*, *c*). However, there were finer nanocrystals of size about 10 nm. Fine nanocrystals were grouped into coarser ones of size 50 to 80 nm, 100 to 130 nm and 300 nm. The largest pores had the size about 1 μ m (Fig. 3, *d*).



*Fig. 3. The pictures of microstructure morphology of *p*-type thermoelectric material $(Bi_2Te_3)_x\text{-}(Sb_2Te_3)_{1-x}$ ($x \approx 0.26$ mol.%) obtained by scanning electron microscope.*

The situation was different in *n*-type samples (Fig. 4). The microstructure was made as fiber bundles oriented relative each other at different angles (Fig. 4, *a*). The fiber bundles were rolled at the angles of 120° – 180°, and at their bend points there were voids from 1 to 5 μ m. The transverse size of the fibers was close to 40 μ m (Fig. 4, *b*). Thin fibers were combined into larger fibers several μ m thick and several tens of μ m long. At larger magnification it is seen that the fibers consist of fine nanocrystals of size 8 to 30 nm (Fig. 4, *c*, *d*). Apart from the fibers, nanocrystals formed coarser crystals of average size 60 nm, 120 nm and 300 nm. However, pores in *n*-type samples were of larger size than in *p*-type samples.

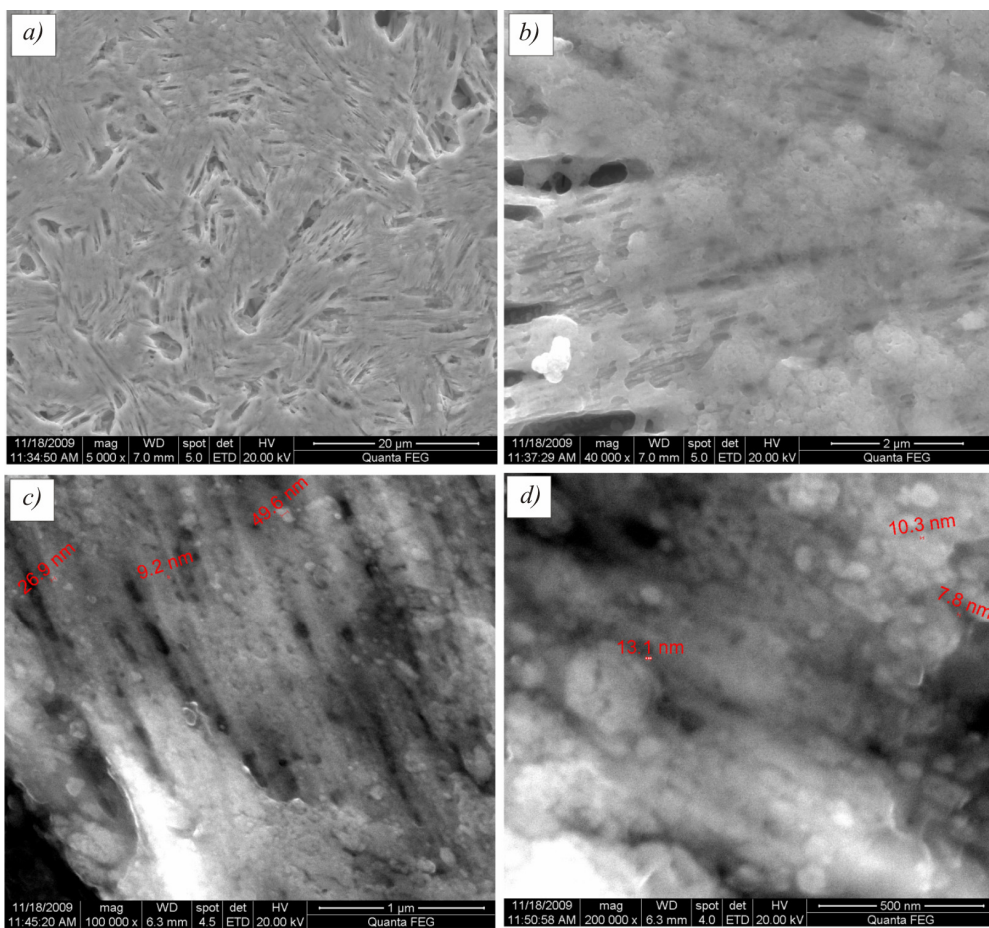


Fig. 4. Pictures of microstructure morphology of n-type thermoelectric material $(Bi_2Se_3)_x-(Bi_2Te_3)_{1-x}$ ($x \approx 0.06$ mol.%) obtained by scanning electron microscope.

The thermoelectric figure of merit of nanostructured thermoelectric materials was determined by the method of separate measurement of thermoEMF, electric resistivity and thermal conductivity. The electric resistivity was measured under isothermal conditions, and thermoEMF – at temperature gradient along the sample about 1 K/cm. The thermal conductivity was measured under transverse adiabatic conditions with temperature gradient along the sample 0.5 K/cm, and carrier concentration – by means of the Hall effect in a magnetic field with the induction of 0.24 T. The measured results are given in Table 1.

Table 1
Thermoelectric properties of extruded materials

Parameters	$(Bi_2Te_3)_x-(Sb_2Te_3)_{1-x}$ p-type	$(Bi_2Se_3)_x-(Bi_2Te_3)_{1-x}$ n-type
ThermoEMF, α , $\mu\text{V/K}$	224	225
Electric resistivity, $\sigma \times 10^{-5}$, $\Omega \cdot \text{m}$	0.95	1.06
Thermal conductivity k , $\text{W}/(\text{m} \cdot \text{K})$	1.6	1.7
Thermoelectric figure of merit $Z \times 10^{-3}$, K^{-1}	3.3	2.8
Charge carrier mobility, $\mu_n \times 10^4$, $\text{cm}^2/\text{V} \cdot \text{s}$	2.7	1.5
Charge carrier concentration $n \times 10^{18}$, cm^{-3}	2.2	4.0

These research results have shown that samples orientation relative to ingot axis produced no effect on the measured parameter values, unlike the results of [9]. This can be due to the difference in material production technologies and their structure. It is noteworthy that thermoelectric figure of merit of *n*-type nanostructured material is lower than that of *p*-type material. Moreover, lower carrier mobility and large concentration contribute to electric resistivity and thermal conductivity increase, though slight, but reducing the thermoelectric figure of merit of this solid solution by 15 %. Comparing the microstructure patterns of investigated materials, it can be noted that the reduction of thermoelectric figure of merit and carrier mobility in *n*-type nanostructured material is probably affected by the fibrous structure randomly oriented in space and the presence of large pores of size up to 5 μm .

3. Conversion factor measurement

3.1. Method with two copper plates

Conversion factor of thermoelectric module was calculated using the method with two copper plates with regard to experimental data as follows. For this purpose, the equations describing thermoelectric processes in thermoelectric modules were employed. Under thermal equilibrium the heat of the Peltier effect and half the Joule heat of thermoelectric module are equal to heat flow from the hot to cold side of the device [10]. This thermal equilibrium corresponds to constant heat flow at maximum temperature difference ($T_h - T_c$) and can be described as

$$\alpha_m \cdot T_h \cdot I + 0.5 \cdot R_m \cdot I^2 - k_m \cdot (T_h - T_c) = 0, \quad (1)$$

where α_m is thermoEMF of thermoelectric module; T_h is hot side temperature of thermoelectric module; T_c is cold side temperature of thermoelectric module; I is electric current flowing through thermoelectric module; R_m is electric resistance of thermoelectric module; k_m is thermal conductivity of thermoelectric module.

Voltage U on thermoelectric module can be calculated from the equality [9]

$$U = \alpha_m \cdot (T_h - T_c) + I \cdot R_m, \quad (2)$$

where α_m , k_m , R_m depend on temperatures T_h and T_c . These dependences can be described by equations

$$\alpha_m = \alpha_1 + \alpha_2 \cdot T + \alpha_3 \cdot T^2 \quad T_h - T_c = 0; \quad (3)$$

$$\alpha_m = (\alpha_m(T_h) - \alpha_m(T_c)) / (T_h - T_c) \quad T_h - T_c \neq 0; \quad (4)$$

$$R_m = R_1 + R_2 \cdot T + R_3 \cdot T^2 \quad T_h - T_c = 0; \quad (5)$$

$$R_m = (R_m(T_h) - R_m(T_c)) / (T_h - T_c) \quad T_h - T_c \neq 0; \quad (6)$$

$$k_m = k_1 + k_2 \cdot T + k_3 \cdot T^2 \quad T_h - T_c = 0; \quad (7)$$

$$k_m = (k_m(T_h) - k_m(T_c)) / (T_h - T_c) \quad T_h - T_c \neq 0. \quad (8)$$

Solution of Eq. (1) and (2), together with Eq.(3 – 8) allows determination of α_m , R_m , and k_m from the series of experiments performed. During each experiment, ΔT_{\max} was measured at constant T_h and a variation of voltage and current. The resulting values made it possible to determine α_m , R_m , and k_m with an error less than 3 %.

Heat N_h , transferred by thermoelectric module was calculated according to equation (1) under equilibrium conditions. Conversion factor of thermoelectric module η was determined as [2, 11]

$$\eta = \frac{N_h}{U \cdot I}. \quad (9)$$

The values of conversion factor at cold surface temperatures $T_c = 273$ K and $T_c = 323$ K in the first experiment are represented in Figs. 5 and 6.

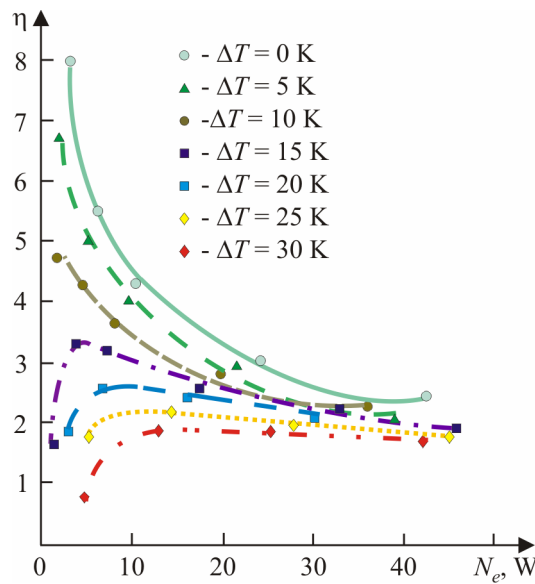


Fig. 5. Conversion factor η versus electric power N_e at temperature $T_c = 273$ K.

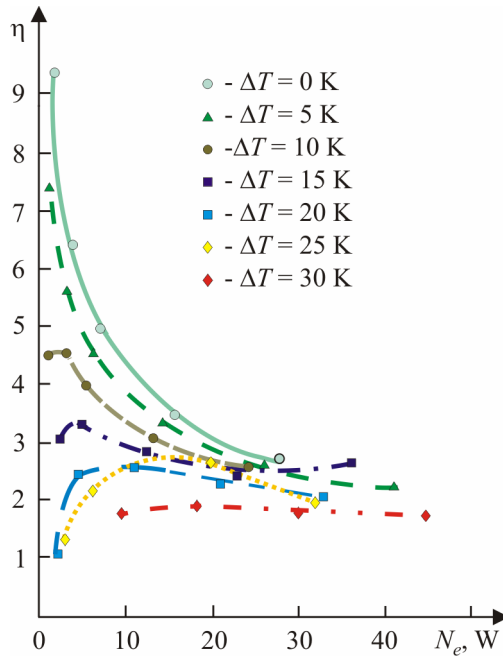


Fig. 6. Conversion factor η versus electric power N_e at temperature $T_c = 323$ K.

There was conversion factor reduction with increase in power and temperature difference for given values of T_c . For $T_c = 323$ K conversion factor increased with temperature difference up to 10 K. Maximum value of conversion factor $\eta = 9.3$ was at consumed electric power $N_e = 2$ W and $\Delta T = 0$. Minimum value of conversion factor was 1.8 at $N_e = 40$ W and $\Delta T = 30^\circ$.

3.2. Method with one copper plate and a heater

In this method, heat transferred by thermoelectric module to copper plate was determined at its temperature rise within 10 s. This time period of temperature variation was much in excess of the time of heat propagation in copper plate ($t \ll 1$ s). The quantity of heat transferred to copper plate N_h was

calculated by relationship [12]:

$$N_h = \frac{cm(T_2 - T_1)}{t}, \quad (10)$$

where c is copper heat capacity; m is copper plate mass; T_1 and T_2 are copper plate temperatures during the first and tenth seconds of measurement. Conversion factor in the second method was calculated according to Eq. (9).

During the second experiment, conversion factor was measured for three electric power values of thermoelectric module. The energy transferred to copper plate was measured and calculated according to Eq. (10) and used for the calculation of conversion factor according to Eq. (9). The measured results for temperature range of +17 °C to +45 °C are represented in Fig. 7. The minimum and maximum thermal power was reduced from 5 W to 4.8 W and from 21.6 W to 14.1 W at consumed electric power from $N_e = 0.75$ W to $N_e = 7.6$ W, respectively. Temperature difference ΔT between the hot and cold surfaces of thermoelectric module varied from 4 to 18 degrees. Conversion factor of this thermomodule reached 8. One should note sufficiently good agreement between the results of measurement of thermomodule conversion factor by both methods.

However, thermoelectric materials used for the manufacture of thermoelectric modules, had thermoelectric figure of merit $ZT \approx 1$ at room temperature. During these experiments we employed thermoelectric nanomaterials with nanocrystallite size 8 to 30 nm. Nanostructured solid solutions $(Bi_2Te_3)_x-(Sb_2Te_3)_{1-x}$ of p -type possess higher thermoelectric figure of merit as compared to n -type material. Therefore, one of the ways for increasing the operating efficiency of thermoelectric modules is to improve the thermoelectric figure of merit of n -type $(Bi_2Se_3)_x-(Bi_2Te_3)_{1-x}$ solid solutions. The results of research point to the following possibilities for improving the efficiency of nanostructured thermoelectric modules.

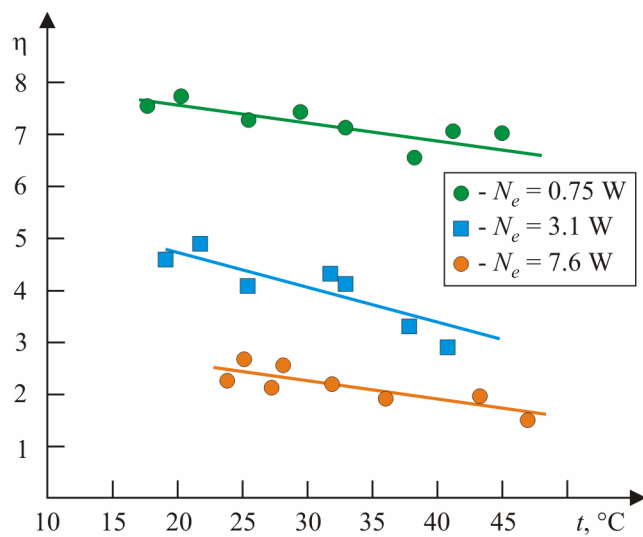


Fig. 7. Conversion factor versus temperature T_h for three values of electric power N_e .

First, apart from the known method of thermal conductivity reduction due to size reduction of nanocrystallites to nanometer units [7, 13, 14], good promise is shown by the development of extrusion method process conditions with a view to improve structural perfection of materials. In our opinion, size reduction of pores and orientation of fibers in n -type nanomaterial, structured in a particular direction, can assure figure of merit increase. Second, doping of solid solutions with a view to improve the thermoelectric properties and the effect of nanostructured materials on structural perfection.

Conclusions

The microstructure morphology of extruded ingots of *p*- and *n*-type thermoelectric materials based on solid solutions of bismuth and antimony chalcogenides was studied. The extruded thermoelectric materials had nanocrystalline structure. Nanocrystals in *p*-type samples were of spherical shape of size 8 to 30 nm combined into clusters of size 60 to 300 nm. Between crystallites there were pores as big as 1 μm . Nanocrystals in *n*-type samples were of similar spherical shape and dimensions, but formed fibers 30 to 60 nm thick. The fibers were combined into bundles of length up to several tens of μm with different orientation and bend by 120 to 180° where the pores of size 1 to 5 μm were observed. Apart from the fibers, nanocrystals formed coarser crystallites of the average size 60 nm, 120 nm and 300 nm.

Using the method of separate measurement of thermoEMF, electric resistivity and thermal conductivity it was established that the thermoelectric figure of merit of extruded nanocrystalline *p*-type materials is $Z = 3.3 \times 10^{-3} \text{ K}^{-1}$, and of *n*-type – $Z = 2.8 \times 10^{-3} \text{ K}^{-1}$.

The lower figure of merit of *n*-type material can be due to lower mobility and high carrier concentration than in *p*-type material.

The conversion factor of thermoelectric modules made of extruded telluride solid solutions was measured. For this purpose, two measurement methods were developed. In the first method, equations describing thermoelectric processes in thermomodules were used for the calculation of thermoelectric and electric parameters, namely thermoEMF, thermal conductivity, as well as electric current, electric resistance and voltage on thermoelectric modules. In the second method, conversion factor was measured under thermoelectric modules operation as heat pumps. These methods showed high efficiency of thermoelectric modules for heat transfer in the temperature range of +17 to +45 °C. Maximum conversion factor reached 6.8 to 8.2 for heat transfer at electric power 0.75 to 2 W and temperature difference 4 – 5 degrees. However, increase in electric power to 40 W and temperature difference to 30° reduced conversion factor to 1.8.

These results demonstrated the possibility of using thermoelectric modules for heating, as well as the necessity of increasing the efficiency of thermoelectric materials. The thermoelectric efficiency of thermoelectric materials can be increased considerably due to size reduction of nanocrystals to nanometer units, improvement of structure perfection and doping of extruded nanothermoelectric materials. Compactness, noiselessness and high efficiency with account of using new nanotechnologies will contribute to a wider application of thermoelectric power converters in new heating systems.

Acknowledgement. The Authors express their gratitude to Dr. A.Churilov for the helpful discussion.

References

1. S.W. Angrist, Direct Energy Conversion, 3d ed. (Boston, Allyn and Bacon Inc., 1976), 518p.
2. D.M. Rowe, CRC Handbook of Thermoelectrics (Boca Raton, CRC Press, 2010), 701p.
3. A.J. Mortlock, Simplified Experiment Demonstrating Interstitial Diffusion in Alpha Iron, *Am. J. Phys.* **33**, 1033 – 1035 (1965).
4. S.B. Riffat, X. Ma, Thermoelectrics: a Review of Present and Potential Applications, *Appl. Therm. Eng.* **23**, 913 – 935 (2003).
5. L. Chen, J. Li, and F.J. Sun, Heat Transfer Effect on Optimal Performance of Two-Stage Thermoelectric Heat Pumps, *Journal of Mechanical Engineering Science* **221**, 1635 – 1641 (2007).
6. B.C. Sales, Smaller Is Cooler, *Science* **295**, 1248 – 1249 (2002).

7. A. Majumdar, Thermoelectricity in Semiconductor Nanostructures, *Science* **303**, 777 – 778 (2004).
8. Q. Zhang, Q. Zhang, S. Chen, W. Liu, K. Lukas, X. Yan, X. Wang, D. Wang, C. Opeil, G. Chen, and Z. Ren, Suppression of Grain Growth by Additive in Nanostructured *p*-type Bismuth Antimony Tellurides, *Nano Energy* **1**, 183 – 189 (2012).
9. I.A. Drabkin, V.B. Osvensky, and Yu.N. Parkhomenko, Anisotropy of Thermoelectric Properties of *p*-Type Thermoelectric Material Based on $(Bi, Sb)_2Te_3$, *J.Thermoelectricity* **3**, 37 – 49 (2013).
10. Thermoelectric Technical Reference – Mathematical Modeling of TEC Modules. *FerroTec.*: <http://www.ferrotac.com> (2009).
11. A.F. Ioffe, *Semiconductor Thermoelements and Thermoelectric Cooling* (London: Infosearch, 1957), 188p.
12. T.I. Tofimova, *Course of Physics* (Moscow: Vyschaya Shkola, 1990), 478 p.
13. M.S. Dresselhaus, G. Chen, M.Y. Tang, R. Yang, H. Lee, D. Wang, Z. Ren, J.P. Fleurial, and P. Gogna, New Directions for Low-Dimensional Thermoelectric Materials, *Adv. Mater.* **19**, 1043 – 1053 (2007).
14. L.P. Bulat, D.A. Kossakovski, and D.A. Pshenai-Severin, Effect of Phonon Thermal Conductivity on Thermoelectric Figure of Merit of Bulk Nanostructured Materials with Tunneling Contacts, *J.Thermoelectricity* **2**, 37 – 44 (2013).

Submitted 09.04.2013.

**V.A. Romaka^{1,2}, P. Rogl³, V.V. Romaka², Yu.V. Stadnyk⁴, R.O. Korzh²,
A.M. Horyn⁴, V.Ya. Krajovsky², O.I. Lakh⁵**

¹Ya. Pidstryhach Institute for Applied Problems of Mechanics
and Mathematics National Academy of Sciences of Ukraine,
3-b, Naukova Str., Lviv, 79060, Ukraine;

²National University “Lvivska Polytechnika”, 12, S.Bandera Str., Lviv, 79013, Ukraine;

³Ivan Franko National University of Lviv, 6, Kyryla and Mefodiya Str., Lviv, 79005, Ukraine;

⁴Institut für Physikalische Chemie, Universität Wien, 42, Währinger Str.,
Wien, A-1090, Österreich;

⁵Closed JSC V.I. Lakh “NVO “Thermoprylad”, 3, Naukova Str., Lviv, 79060, Ukraine

OPTIMIZATION OF PARAMETERS OF THE NEW THERMOELECTRIC MATERIAL $HfNiSn_{1-x}Sb_x$

The crystalline and electronic structures, temperature and concentration dependences of resistivity and the Seebeck coefficient of n-HfNiSn intermetallic semiconductor doped with Sb were investigated in the temperature range $T = 80 \div 400$ K. The main mechanisms of conduction were established and they are in agreement with the results of theoretical studies of electronic structure of $HfNiSn_{1-x}Sb_x$. It was predicted and shown that the obtained thermometric material $HfNiSn_{1-x}Sb_x$ has high efficiency of thermal into electrical energy conversion.

Key words: electronic structure, Fermi level, resistivity, Seebeck coefficient.

Introduction

Intermetallic semiconductor *n*-HfNiSn is known to possess high efficiency of thermal into electric energy conversion, though insufficient for industrial application [1]. At the same time, optimization of parameters of thermoelectric materials to obtain maximum values of thermoelectric figure of merit depends on a number of factors, in particular, current carrier concentration, scattering mechanisms, thermal conductivity, the choice of crystallographic orientation, etc. One of the methods for improving the thermoelectric figure of merit of semiconductor materials is their doping [1, 2].

In [3] it was shown that in the intermetallic semiconductors of MgAgAs structural type (half-Heusler alloys) a pre-requisite for achieving maximum efficiency of thermal into electric energy conversion is semiconductor doping with such type of impurities that would coincide with the type of major carriers of base semiconductor matrix.

On the other hand, investigations [4] showed that crystalline structure of HfNiSn compound is disordered, namely position of Hf ($5d^26s^2$) atoms up to ~ 1 % is occupied with Ni ($3d^84s^2$) atoms, which generates donor defects in crystal structure. Exactly this structural feature of HfNiSn accounts for the mechanism of “a priori doping” the semiconductor with a donor impurity.

Thus, in conformity with conclusions of [3], to improve the efficiency of thermal into electric energy conversion, the semiconductor *n*-HfNiSn must be doped with such type of impurity which would generate donor-nature defects in the crystal. One of the variants of such doping is introduction into HfNiSn compound of Sb ($4d^{10}5s^{25}p^3$) atoms through substitution of Sn ($4d^{10}5s^{25}p^2$) atoms. As long

as Sb atom has one $5p$ -electron more than Sn atom, such substitution should have generated donor-nature structural defects in the crystal. In this case, one should expect increase in the efficiency of thermal into electric energy conversion in $HfNiSn_{1-x}Sb_x$ when the Fermi level approaches the level of semiconductor conduction band.

The purpose of this paper is to study the prospects of using the new thermoelectric material $HfNiSn_{1-x}Sb_x$ for thermal into electric energy conversion. The proposed complex work studies the mechanism and conditions for entry of Sb atoms into the structure of $HfNiSn$ compound with employment of experimental analysis methods, as well as calculations of its electronic structure. In particular, the dynamics of change in crystalline structure of $HfNiSn_{1-x}Sb_x$ will be investigated, the region of solid solution existence will be established, as well as simulation of electronic structure and thermodynamic calculations will be performed. Besides, the electrokinetic and energy characteristics of $HfNiSn_{1-x}Sb_x$ will be analyzed, as well as the experimental and calculated results will be compared, wherefrom will follow the degree of adequacy of the proposed models of crystalline and electronic structures of semiconductor.

Investigation methods

The object to be investigated included crystalline structure, electron density distribution (DOS), electrokinetic and energy characteristics of $HfNiSn_{1-x}Sb_x$. The samples were synthesized in the laboratory of Institute for Physical Chemistry, Vienna University. The X -ray structural analysis [5] with employment of Fullprof program [6] was used to obtain the values of $HfNiSn_{1-x}Sb_x$ crystal lattice periods. The data arrays obtained by powder method were used (diffractometer Guinier-Huber image plate system, $CuK\alpha_1$ -radiation; $8^\circ \leq 2\theta \leq 100^\circ$). The chemical and phase compositions of samples were controlled by scanning electron microscope (SEM, Zeiss Supra 55VP) and microprobe analyzer (EPMA, energy-dispersive X -ray analyzer). The electronic structure calculations were performed by the Korringa-Kohn-Rostoker (KKR) methods in coherent potential approximation (CPA), local density approximation (LDA) and plane wave approximation (FP-LAPW) in the framework of density functional theory (DFT) [7]. The temperature and concentration dependences of the electrical resistivity ρ and the Seebeck coefficient α of $HfNiSn_{1-x}Sb_x$ were measured in the ranges: $T = 80 \div 400$ K, $N_D^{Sb} \approx 9.5 \cdot 10^{19} \text{ cm}^{-3}$ ($x = 0.005$) $\div 1.9 \cdot 10^{21} \text{ cm}^{-3}$ ($x = 0.10$).

Research on structural features of $HfNiSn_{1-x}Sb_x$

To verify the above stated assumption as to the method of doping n - $HfNiSn$ for obtaining the new thermoelectric material with high thermoelectric power values, samples were synthesized where Sn atoms were substituted by Sb atoms. The microprobe analysis of the concentration of atoms on the surface and cleavages of $HfNiSn_{1-x}Sb_x$ samples has showed their conformity to the initial charge compositions, which is one of the experimental proofs of predicted substitution of Sn atoms by Sb atoms. In their turn, the X -ray phase and structural analyses have shown that all the investigated samples of $HfNiSn_{1-x}Sb_x$ have no traces of other phases, except for the basic one, up to the composition $x = 0.1$ inclusive (structural type $MgAgAs$, cubic syngony, space group $F\bar{4}3m$). According to X -ray phase analysis, the synthesized samples of solid solution $HfNiSn_{1-x}Sb_x$ are single-phase up to $x = 0.1$ inclusive. Research on the structure of $HfNiSn_{1-x}Sb_x$ detected the substitution of Sn atoms by Sb atoms, leading to a regular growth of unit cell period $a(x)$ (Fig. 1 a). These results agree with the difference in atomic radii of Sn ($r_{Sn} = 0.158$ nm) and Sb ($r_{Sb} = 0.160$ nm).

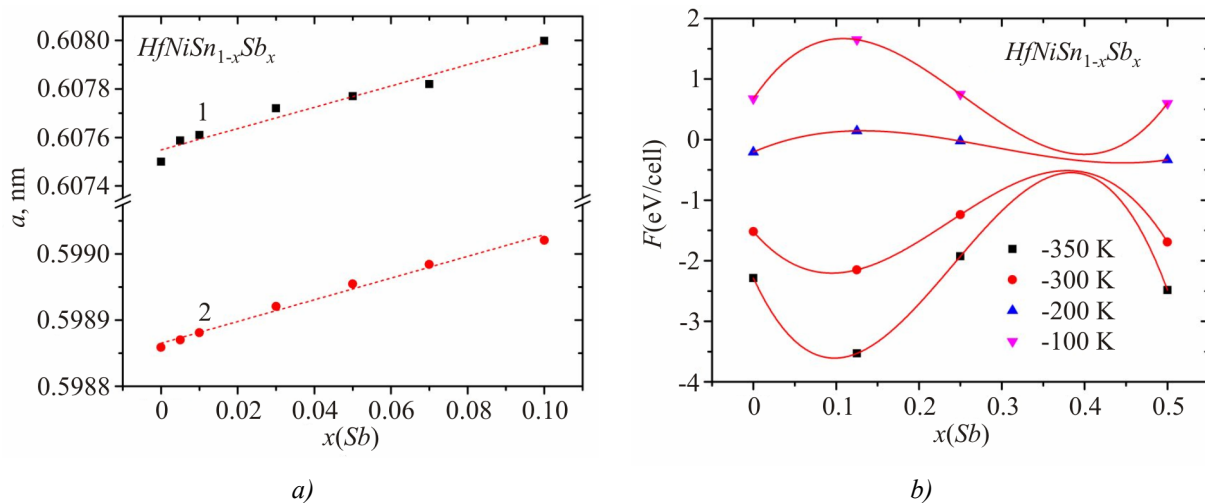


Fig. 1. a) Change in $a(x)$ period values: 1 – experimental value;
 2 – calculated values; b) free energy $F(x)$ of $HfNiSn_{1-x}Sb_x$.

The refinement of crystalline structure by powder method has shown that the degree of occupancy of atomic position $Sn(Sb)$ is 100 %, and the structure of $HfNiSn_{1-x}Sb_x$ is ordered, which creates prerequisites for obtaining semiconductor material with unambiguous characteristics that do not change during many cycles of samples heating and cooling. Note that the ordering of $HfNiSn_{1-x}Sb_x$ structure means that with the lowest concentrations of Sb atoms which occupy the position of Sn atoms, there is a parallel process of return of 1 % of Ni atoms that occupied the crystallographic position of Hf to their own crystallographic position [4].

Optimization of the values of unit cell period $a(x)$ of $HfNiSn_{1-x}Sb_x$ for the concentrations $x(Sb) = 0, 0.25$ and 0.5 yielded its concentration dependence (Fig. 1 a). Calculations confirmed growth of unit cell parameter, but with a positive deviation from linearity. As long as the use of local density approximation leads to underestimation of the values of energy and unit cell periods, the resulting calculated values of unit cell period $a(x)$ (Fig. 1 a) are systematically underrated with respect to experimental values, but the tendency remains practically the same.

In their turn, thermodynamic calculations with the use of DFT in the approximation of harmonic fluctuations of atoms have shown that dependence of free energy (Helmholtz potential) at a temperature of 350 K passes through the minimum (Fig. 1 b) at concentration $x(Sb) \approx 0.1$, thus indicating the restricted solubility of Sb atoms in crystalline structure of $HfNiSn$, which is experimentally confirmed, but differs essentially from the solubility of rare-earth metal atoms in $HfNiSn$ which makes ~ 0.3 [1]. Moreover, from Fig. 1 b it follows that with a rise in temperature the solubility of Sb atoms in $HfNiSn$ structure is increased.

On the other hand, calculations of the distribution of electron localization function (ELF) in the initial $HfNiSn$ and doped $HfNiSn_{1-x}Sb_x$ compounds point to additional electron density localization between Ni and Sb atoms (Fig. 2), which is indicative of electron density growth in crystal due to donor impurity nature. Based on this result it can be concluded that the substitution of p -element in crystal structure of $HfNiSn$ produces a much larger effect on its stability than the substitution of Hf or Ni atoms. This is because a system of tetrahedral ion-covalent bonds is formed due to tetrahedral hybridization of Sn atomic orbitals, and any essential changes in the number of valence electrons on p -orbitals will result in formation of more energetically beneficial chemical bonds and, as a consequence, in the destruction of $MgAgAs$ type structure [4, 8].

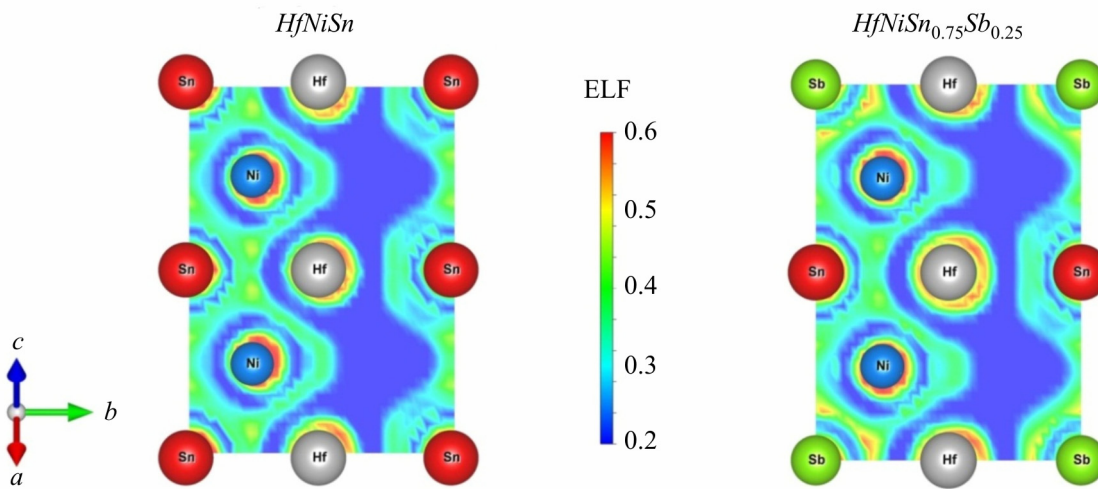


Fig. 2. Projection of electron localization function (ELF) on the plane [101] for the initial compound $HfNiSn$ and for compound $HfNiSn_{0.75}Sb_{0.25}$.

Therefore, structural investigations of n - $HfNiSn$ doped with Sb atoms have demonstrated that Sb atoms occupy exceptionally crystallographic position of Sn atoms, generating donor-nature structural defects in the crystal, and the solubility area of Sb atoms in $HfNiSn_{1-x}Sb_x$ matrix is $x \leq 0.10$.

Research on the electron structure of $HfNiSn_{1-x}Sb_x$

To predict the behaviour of the Fermi level ε_F , the energy gap ε_g and the electrokinetic characteristics of n - $HfNiSn$ doped with Sb atoms, the electron density distribution (DOS) of $HfNiSn_{1-x}Sb_x$ was calculated. In view of the fact that introduction into $HfNiSn$ compound of impurity Sb atoms puts in order its crystalline structure, calculations of DOS were performed for the case of ordered crystalline structure.

As indicated above, introduction of Sb atoms into crystalline structure of $HfNiSn$ compound is accompanied by generation of donor-nature structural defects. In this case, doping with donor impurities the intermetallic semiconductor n - $HfNiSn$ the structure of which already has donor defects will reduce the compensation degree, and the Fermi level will drift in the direction of conduction band that will be crossed at certain concentrations of Sb impurity atoms. Fig. 3 a shows the results of calculation of electron density distribution, variation in energy gap and the Fermi level position for the ordered variant of $HfNiSn_{1-x}Sb_x$ crystalline structure. It is obvious that on introducing into n - $HfNiSn$ the least attainable in the experiment concentrations of Sb donor impurity, the Fermi level ε_F moves from the energy gap where in n - $HfNiSn$ it was located near the bottom of conduction band at the distance of ~ 81.3 meV [9] to conduction band, i.e. dielectric-metal transition is realized, which is Anderson transition [10]. With increase in donor impurity concentration, the Fermi level drifts in the band of continuous energies. Apart from the drift caused by a reduction in semiconductor compensation degree, there is also a reduction in the values of semiconductor effective energy gap ε_g from $\varepsilon_g(x=0)=287.7$ meV to $\varepsilon_g(x=0.01)=181.7$ meV due to increase of band “tails” changing the profile of continuous energy bands (Fig. 3 a).

Such Fermi level behaviour caused by ordering semiconductor crystalline structure allows predicting the conductivity mechanisms and electrokinetic characteristics of semiconductor solid solution $HfNiSn_{1-x}Sb_x$. Having calculated the electron structure of $HfNiSn_{1-x}Sb_x$, one can predict the

behaviour of its electrokinetic characteristics, and Fig. 3 b, as a reference, shows a change in the Seebeck coefficient values of $HfNiSn_{1-x}Sb_x$ at different temperatures.

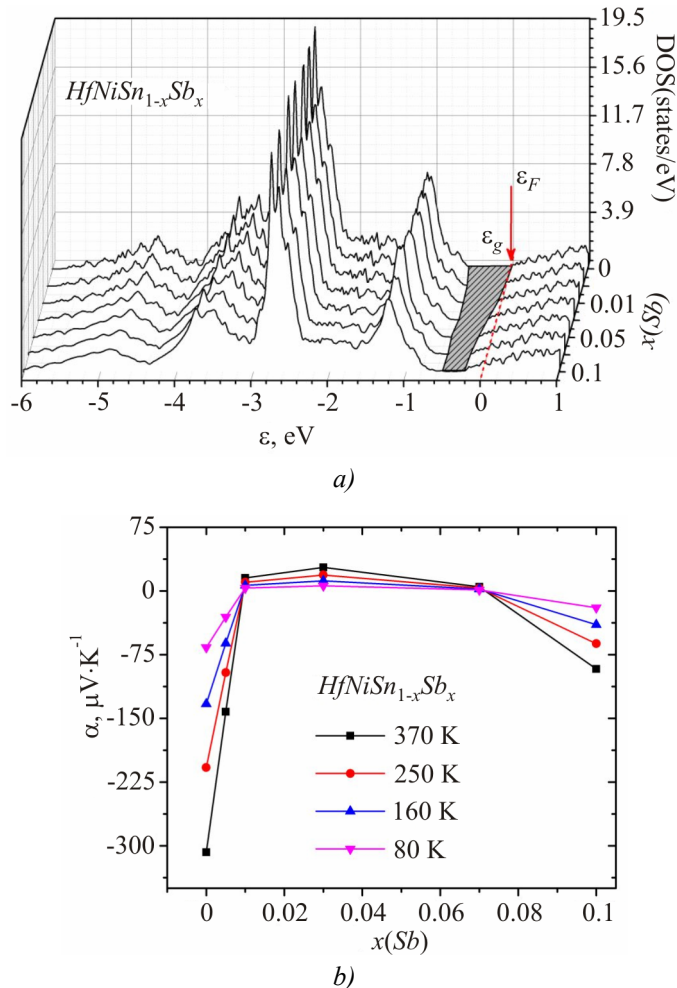


Fig. 3. Electron density distribution DOS (a) and calculations of variation in the values of the Seebeck coefficient $\alpha(x)$ at different temperatures (b) of $HfNiSn_{1-x}Sb_x$.

A low concentration of impurities whereby there is dielectric-metal transition allows purposeful getting in $HfNiSn_{1-x}Sb_x$ high values of the Seebeck coefficient α and electric conductivity σ , which will assure high values of thermoelectric power factor $Z^* = \alpha^2/\sigma$. Moreover, high values of the Seebeck coefficient α of $HfNiSn_{1-x}Sb_x$ in a wide temperature range make this solid solution also a promising thermometric material for the manufacture of sensitive elements of thermoelectric thermometers.

Thus, the results of calculations of electron density distribution of $HfNiSn_{1-x}Sb_x$ based on the results of structural investigations point to the donor nature of generated structural defects, and the experimental investigations will test the adequacy of calculated results, hence of selected model of semiconductor structure.

Research on the electrokinetic and energy characteristics of $HfNiSn_{1-x}Sb_x$

Fig. 4 presents the temperature dependences of electric resistivity ρ and the Seebeck coefficient $\alpha(1/T)$ for samples of $HfNiSn_{1-x}Sb_x$, $0 \leq x \leq 0.10$ which vary in full conformity with the results of calculations of electron density distribution.

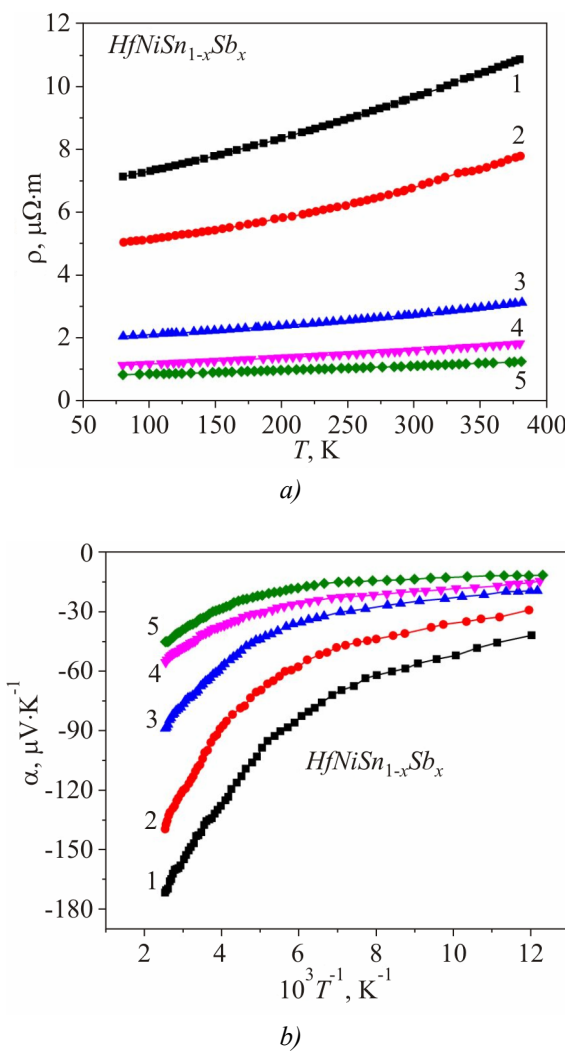
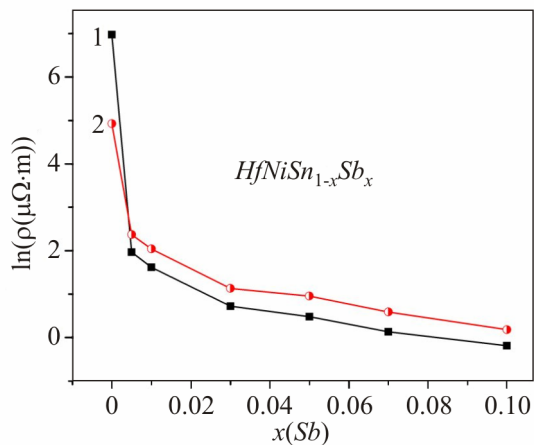


Fig. 4. Temperature dependences of electric resistivity ρ (a) and the Seebeck coefficient α (b) of $HfNiSn_{1-x}Sb_x$: 1 – $x = 0.005$; 2 – $x = 0.01$; 3 – $x = 0.03$; 4 – $x = 0.07$; 5 – $x = 0.10$.

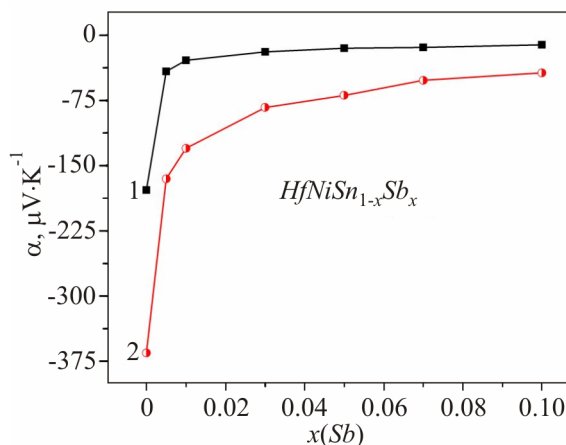
Adding the lowest concentration of Sb atoms leads to increase in the values of electric resistivity (ρ) with a rise in temperature and the absence of activation areas on its temperature dependences. Such behaviour of $\rho(T)$ is typical of metallic conductivity type, which is possible when the Fermi level ε_F approaches the edge of conductivity band by the value close to $k_B T$, or in the case of entry into the zone of continuous energies.

Moreover, the electric resistivity values drastically decrease (Fig. 5 a) with increase in the concentration of Sb impurity atoms in the structure of $HfNiSn$ compound, which is possible only with generation in crystal of donor-nature defects and increase in the concentration of free electrons. Thus, for instance, at $T = 80$ K the value of $\rho(x)$ drastically decreases from $\rho_{x=0} = 1071.1 \mu\Omega \cdot m$ to the value of $\rho_{x=0.005} = 7.14 \mu\Omega \cdot m$. Such behaviour of $\rho(x)$ is caused by increase in the values of density of states on the Fermi level with a decrease in semiconductor compensation degree, which was anticipated by the calculations of its electronic structure. The fact that the Fermi level is displaced exactly in the direction of conduction band on doping n - $HfNiSn$ with Sb donor impurity is shown by the dependences of variation in the Seebeck coefficient values over the entire temperature and concentration ranges (Fig. 5 b). Thus, the value of the Seebeck coefficient, for instance, at 80 K, varies

from $\alpha_{x=0} = -178.1 \mu\text{VK}^{-1}$ to the value of $\alpha_{x=0.005} = -41.5 \mu\text{VK}^{-1}$, which points to approaching by the Fermi level the edge of semiconductor conduction band.



a)



b)

Fig. 5. Change in the values of electric resistivity $\rho(x)$ (a) and the Seebeck coefficient $\alpha(x)$ (b) of $HfNiSn_{1-x}Sb_x$ at different temperatures: 1 – $T = 80 \text{ K}$; 2 – $T = 380 \text{ K}$.

One of the arguments that Sb impurity atoms generate donor defects in the structure of $HfNiSn$ compound is the character of variation in the amplitude of large-scale fluctuation of continuous-energy bands (ε_1^α) and the averaged amplitude of potential well of small-scale fluctuation (ε_3^α) (Fig. 6 a) of $HfNiSn_{1-x}Sb_x$, calculated by the high- and low-temperature areas of $\alpha(1/T)$ dependences, respectively [1].

Introduction into n - $HfNiSn$ of Sb donor impurity is accompanied by a reduction in semiconductor compensation degree [10], which will cause a reduction in the values of fluctuation amplitude (a reduction in the values of ε_1^α). Moreover, there is also a correlation between the amplitude values of large-scale fluctuation ε_1^α and the potential well depth of small-scale fluctuation ε_3^α , namely the lower the fluctuation amplitude, the smaller the potential well of small-scale fluctuation [10].

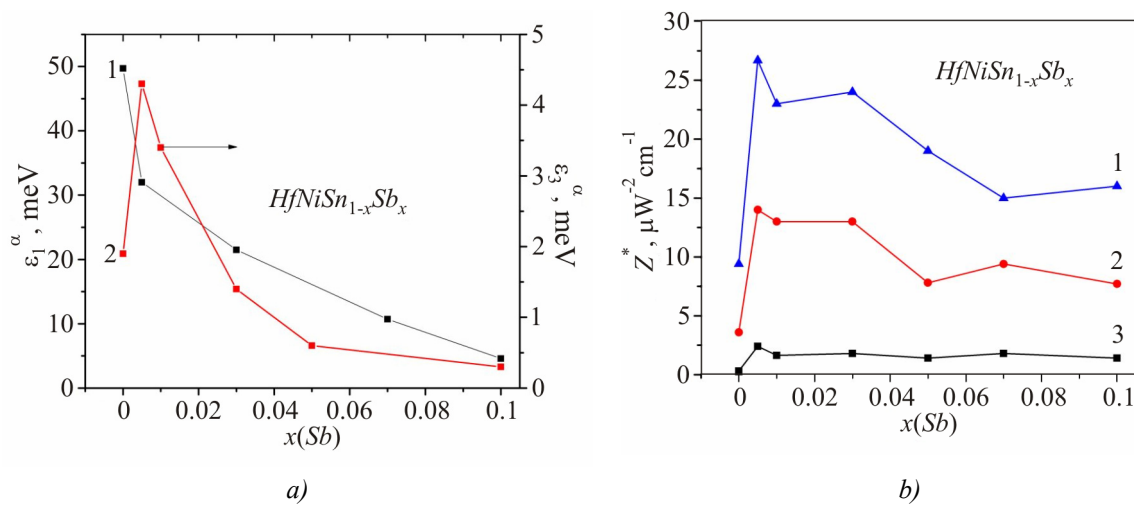


Fig. 6. Change in the values of activation energies ε_1^α (1) and ε_3^α (2) (a) and thermoelectric power factor Z (b) of $HfNiSn_{1-x}Sb_x$ at different temperatures: 1 – $T = 380$ K; 2 – $T = 250$ K; 3 – $T = 80$ K.

Thus, doping of intermetallic semiconductor n - $HfNiSn$ with Sb donor impurity is characterized by increase in electric conductivity values with relatively high values of thermopower factor. This is a guarantee of obtaining high values of thermoelectric power factor in a semiconductor solid solution $HfNiSn_{1-x}Sb_x$.

Research on thermoelectric power factor of $HfNiSn_{1-x}Sb_x$

Fig. 6 b represents the concentration dependences of change in thermoelectric power factor Z^* of $HfNiSn_{1-x}Sb_x$. We can see that exactly at the lowest concentration of donor impurity, $x = 0.005$, the values of thermoelectric power factor are maximum. Such a behaviour of $Z^*(x)$ of $HfNiSn_{1-x}Sb_x$ is understandable and was expected on the basis of calculations of semiconductor electron density distribution.

Conclusions

Thus, based on the foregoing results we can assert that the obtained solid solution $HfNiSn_{1-x}Sb_x$ is a new promising thermoelectric material, and in its characteristics, in particular, the values of thermoelectric power factor, it outperforms considerably n - $HfNiSn$. Moreover, the values of thermoelectric power factor increase with a rise in temperature, which expands the range of their possible application.

The work was performed in the framework of grant of the National Academy of Sciences, № 106U000594.

References

1. V.A. Romaka, V.V. Romaka, and Yu.V. Stadnyk, *Intermetallic Semiconductors: Properties and Applications* (Lviv, Lvivska Polytechnika, 2011), 488 p.
2. L.I. Anatychuk, *Thermoelements and Thermoelectric Devices* (Kyiv: Naukova Dumka, 1979), 768 p.
3. V.A. Romaka, D. Fruchart, Yu.V. Stadnyk, J. Tobola, Yu.K. Horelenko, M.G. Shelyapina, L.P. Romaka and V.F. Chekurin, Conditions for the Attainment of Maximum Values of Thermo-

- electric Power Factor in the Intermetallic Semiconductors of $MgAgAs$ Structural Type, *Semiconductors* **40** (11), 1289 – 1395 (2006).
- 4. V.V. Romaka, P. Rogl, L. Romaka, Yu. Stadnyk, A. Grytsiv, O. Lakh, and V. Krajovsky, Peculiarities of Structural Disorder in Zr - and Hf -Containing Heusler and Half-Heusler Stannides, *Intermetallics* **35**, 45 – 52 (2013).
 - 5. V.K. Pecharsky, P.U. Zavalij, *Fundamentals of Powder Diffraction and Structural Characterization of Materials* (NY, Springer, 2005), 713 p.
 - 6. T. Roisnel, J. Rodriguez-Carvajal, WinPLOTR: a Windows Tool for Powder Diffraction Patterns Analysis, *Mater. Sci. Forum, Proc. EPDIC7* **378 – 381**, 118 – 123 (2001).
 - 7. M. Schröter, H. Ebert, H. Akai, P. Entel, E. Hoffmann and G.G. Reddy, First-Principles Investigations of Atomic Disorder Effects on Magnetic and Structural Instabilities in Transition-Metal Alloys, *Phys. Rev. B* **52**, 188 (1995).
 - 8. V.K. Grigorovich, *Metallic Bond and Structure of Metals* (Moscow: Nauka, 1988), 296 p.
 - 9. V.A. Romaka, P. Rogl, V.V. Romaka, Yu.V. Stadnyk, E.K. Hlil, V.Ya. Krajovsky, and A.M. Horyn, Features of Conduction Mechanisms in n - $HfNiSn$ Semiconductor Heavily Doped with Rh Acceptor Impurity, *Semiconductors* **47** (9), 1145 – 1152 (2013).
 - 10. B.I. Shklovsky, A.L. Efros, *Electronic Properties of Doped Semiconductors* (Moscow: Nauka, 1979), 416 p.

Submitted 06.11.2013.



Yu.M. Lobunets

Yu.M. Lobunets

Institute of Thermoelectricity
of the NAS and MES Ukraine, 1, Nauky Str.,
Chernivtsi, 58029, Ukraine

**PERFORMANCE ANALYSIS OF HEAT-EXCHANGE
TYPE THERMOELECTRIC GENERATOR**

Performance analysis of a thermoelectric generator integrated into a compact plate heat exchanger is considered. The dependences of the generator technical and economic characteristics on the regime and geometrical parameters are determined. Design recommendations for such devices are given.

Key words: thermoelectric generator, low-grade heat source.

Introduction

One of the promising applications of thermoelectric generators (TEG) is their use for low-grade thermal into electric energy conversion. In the majority of cases heat transfer from low-grade sources takes place by means of liquid heat carriers, which predetermines possible TEG design. The most common for such TEG is a scheme where thermopiles are equipped with heat exchangers with direct current or counter current flow of heat carriers realizing supply and removal of heat. The main requirement to TEG of this type is to provide minimum mass-dimensional characteristics of a device with maximum possible efficiency. A scheme of TEG where thermopiles are integrated into a compact plate heat exchanger [1] seems to be rather promising for solving these problems. In this design the function of heat exchanger plates is performed by thermopiles with heat carrier flow channels arranged between them by means of gaskets. Due to high intensity of heat exchange in the slot channels between the thermopiles and doing away with the bulky and metal-consuming heat exchangers, such a design allows reducing the mass and dimensions of TEG practically by an order as compared to conventional devices.

In this work, the specific features of the design under study are analyzed and possible technical and economic characteristics of such thermoelectric generators are estimated.

Problem formulation

The problem consists in creation of a mathematical model describing correctly the relation between the regime and geometrical parameters of TEG, and in using it for performance analysis of system under consideration. A design scheme of the problem is represented in Fig. 1.

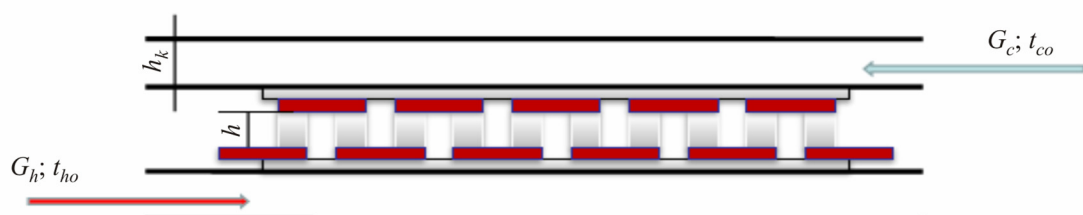


Fig. 1. Design scheme of TEG.

Heating and cooling heat carriers passing through the slot channels between thermopiles flow around the surface of the latter, keeping temperature difference ΔT on the thermoelements. It is obvious that due to irreversible heat exchange losses, as well as due to change in heat carrier temperature along the thermopile, the operating temperature difference on thermoelements will be always less than the available difference:

$$\Delta T < dt_o = t_{ho} - t_{co}; \quad (1)$$

here t_h and t_c are the initial temperatures of heat carriers; indices h и c refer to heating and cooling heat carriers, respectively.

Moreover, part of the energy generated by TEG is spent on circulating pump drive for pumping of heat carriers. It is necessary to minimize these losses and determine the conditions whereby the net power of TEG reaches maximum values under the existing restrictions.

As is known from heat exchange theory, with a counter current flow of heat carriers with the same mass specific heat, the difference in temperature between heat carriers is kept constant along the heat exchange surface

$$dt = t_h - t_c = const \quad (2)$$

As long as for TEG mode the influence of the Peltier heat on temperature distribution in heat carriers can be ignored, in the first approximation the temperature difference between heat carriers can be also considered to be constant and determined as [2]:

$$dt = \frac{dt_o}{1 + \frac{KF}{W}} \quad (3)$$

where $W = Gc_p$ is specific heat of heat carrier mass flow rate (water equivalent), W/K; F is heat exchange surface area, cm^2 ;

$K = \frac{1}{\frac{1}{\alpha_c} + \frac{1}{\alpha_h} + \frac{h}{\lambda}}$ is heat transfer coefficient, $\text{W/cm}^2\text{K}$; α_c and α_h are the effective coefficients of heat transfer from the cold and hot sides taking into account the packing density of thermoelements in the module and the presence of ceramic heat spreaders:

$$\alpha_c = \frac{S_m}{S_t} \frac{1}{\frac{1}{\alpha_{co}} + \frac{\delta}{\lambda_k}}; \quad \alpha_h = \frac{S_m}{S_t} \frac{1}{\frac{1}{\alpha_{ho}} + \frac{\delta}{\lambda_k}};$$

α_c and α_h are the heat exchange coefficients on the cold and hot thermopile surface; S_m is the module area; S_t is the cross-sectional area of thermoelements in the module; h is the height of thermoelements, cm; λ is the thermal conductivity of thermoelectric material, W/cmK ; δ is the thickness of ceramic heat spreader, cm; λ_k is the thermal conductivity of ceramics, W/cmK .

Expression (3) can be used to determine the temperature conditions for the assignment of the boundary conditions in the calculation of TEG. The dependence of temperature difference dt on heat carrier flow rate (W) and heat exchange conditions (KF) is illustrated in Fig. 2. As it follows from the figure, the temperature difference tends to its limiting value $dt \rightarrow dt_o$ with increase in heat carrier flow rate; it is due to a decrease in heat carrier temperature change along the channel. Heat exchange intensification (KF growth), on the one hand, leads to a reduction in temperature difference losses at heat exchange, and on the other hand – to an increase in heat flows and, respectively, to a change in

heat carrier temperatures along the thermopile. The latter factor has a great impact on the reduction of temperature difference.

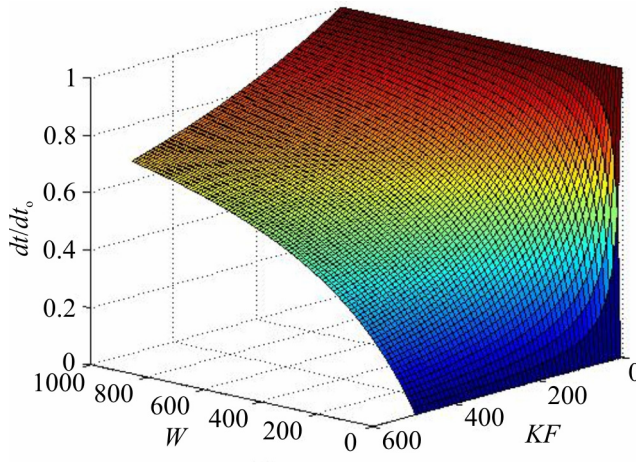


Fig. 2. Effect of heat transfer conditions on the temperature difference dt/dt_o .

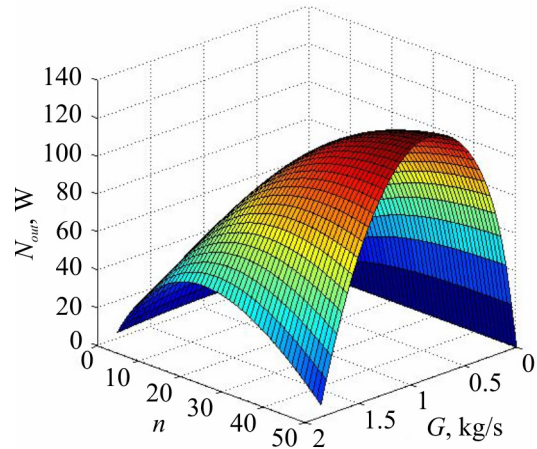


Fig. 3. Dependence of TEG net power on heat carrier flow rate (G) and thermopile area (n).

At the same time, as heat carrier flow rate increases, the hydraulic losses in channels increase, as a result of which the generator net power is reduced. That is, it can be supposed that there are optimal ratios of regime (heat carrier flow rate, TEG load conditions) and geometrical parameters (channel dimensions, the number and dimensions of modules in thermopiles) that assure the best technical and economical figures of TEG. This assumption is well illustrated in Fig. 3 which represents the dependence of net power of TEG thermopile as a function of heat carrier flow rate and thermopile area (the thermopile area is expressed through the number of modules n arranged along the heat carrier flow).

Mathematical model of TEG

The calculation data were obtained with the use of a mathematical model of TEG including:

- solving the equation of heat and electricity transfer in thermoelements with the boundary conditions of III kind in the form [3-5]:

$$\Theta(J, Y) = C_1 + C_2 Y - \frac{J^2}{2I_o} Y^2, \quad (4)$$

where

$$C_1 = \frac{(b_2 Bi_c \theta_c - b_1))}{(J - Bi_h + b_2 (J + Bi_c))};$$

$$C_2 = C_1 \frac{(J + Bi_c) - Bi_c \theta_c}{J^2 (J - Bi_h)};$$

$$b_1 = \frac{J^2}{I_o} - 2I_o + Bi_h \theta_h;$$

$$b_2 = J - Bi_h - 1;$$

Here $\Theta = T/t_o$ is the dimensionless temperature of thermoelement; $\theta_{c,h} = t/t_o$ is the dimensionless temperature of heat carrier; $Y = y/h$ is the dimensionless coordinate; $J = jeh/\lambda$ is the dimensionless

current density; $Bi = \alpha h/\lambda$ is the Biot criterion; $I_o = zt_o$ is the Ioffe criterion; $z = (e^2 \cdot \sigma)/\lambda$ is the thermoelectric figure of merit of material; h is the thermoelement height; $t_o = 300$ K is the governing temperature.

Criterion equations for the determination of heat transfer coefficients [2]

$$Nu = 0.022 Re^{0.8} Pr^{0.43} \quad (5)$$

and coefficients of friction with liquid flow in a plane channel:
for a laminar flow ($Re < 2300$)

$$\xi = \frac{96}{Re}; \quad (6)$$

for a turbulent flow ($Re > 2300$)

$$\xi = \frac{\left(\frac{Pr_f}{Pr_w} \right) 0.333}{1.82 \log(Re - 1.64)}; \quad (7)$$

Here $Nu = \alpha d/\lambda$ is the Nusselt criterion; $Re = Vd/\nu$ is the Reynolds criterion; Pr is the Prandtl criterion; d is the equivalent diameter of the channel.

As long as the properties of heat carriers are essentially dependent on temperature, the calculation of transfer coefficients was done with the interpolation of tabulated data through use of cubic splines.

The system of equations (2 – 7) allows us to calculate temperature distributions in thermoelements and heat carriers and, accordingly, to determine the characteristics of TEG as a function of the basic regime and geometrical parameters with the assigned properties of thermoelectric material and heat carriers. In the general form the TEG power is:

$$N = \frac{E^2}{R} \frac{m}{(m+1)^2}; \quad (8)$$

Here $E = ne\Delta T$ is the TEG EMF; n is the number of couples connected in series; R is the TEG internal resistance; m is the load factor.

The TEG net power is:

$$N_{out} = N - N_{pump}, \quad (9)$$

where $N_{pump} = \frac{G_c dP_c}{0.9\rho_c} + \frac{G_h dP_h}{0.9\rho_h}$ is energy consumption for pumping; $dP = \xi \frac{L\rho}{d} \frac{V^2}{2}$ is pressure loss in channels; L is channel length; $\rho_{c, h}$ is heat carrier density; $V = G/f$ is heat carrier velocity; f is cross-sectional area of channels.

The conversion efficiency of TEG and the total generator efficiency are, respectively

$$\eta = \frac{N}{Q} \quad (10)$$

$$\eta_{out} = \frac{N_{out}}{Q} \quad (11)$$

where $Q = KSdt$ is heat flow through generator thermopiles; S is the effective area of TEG thermopiles.

Analysis results

The basic problem parameters affecting the characteristics of TEG are the dimensions and number of thermoelectric modules, their properties, the flow rate and temperatures of heat carriers, the size of channels between thermopiles. The possibilities of variation of the majority of these parameters are limited. To the independent variables of the problem in hand that permit variation over sufficiently wide range one can refer heat carrier flow rate G , channel size h_k and, to a lesser extent, thermoelement height h .

From the standpoint of TEG efficiency of primary interest is the effect of these variables on temperature distribution in the system. It is obvious that the purpose of optimization of TEG parameters in the first approximation is to assure maximum possible operating temperature range on thermoelements. Maximum change of temperatures in the system is restricted by the available difference $dt_o = t_h - t_c$. Therefore, for generality of the results, we estimate the changes in governing temperatures with respect to maximum possible temperature difference dt_o . The effect of regime parameters on the temperature mode of TEG is illustrated in Fig. 4. The ranges of change in regime parameters correspond to the domain of definition of the problem under consideration. In this particular case we considered a TEG comprising thermopiles of size 150×800 mm. The thermopiles consist of three longitudinal rows 16 modules each, altogether 48 standard modules of size 40×40 mm.

For given temperature range of heat carriers (water) which is $t_c = 5^\circ\text{C}$; $t_h = 95^\circ\text{C}$, the permissible flow rate range is $G = 0 \dots 1 \text{ kg/s}$. The channel height varies within $h_k = 1 \dots 20 \text{ mm}$. Under given conditions the relative temperature difference between heat carriers varies within

$$dt = (0.22 \dots 0.97) dt_o;$$

the losses in temperature difference along the channel are

$$t_{in} - t_{out} = (0.03 \dots 0.78) dt_o;$$

the temperature difference on thermoelements varies within

$$\Delta T = (0.002 \dots 0.79) dt_o.$$

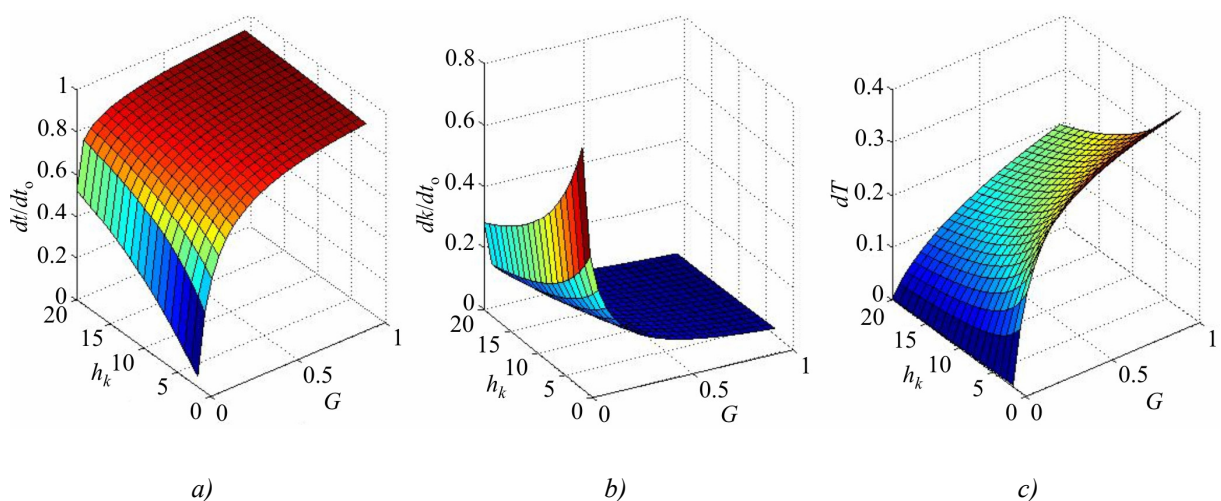


*Fig. 4. Effect of regime parameters on the temperature mode of TEG.
 a) –temperature difference between heat carriers; b) –temperature difference along the channel;
 c) –temperature difference on thermoelements.*

The net temperature difference ΔT monotonously increases with increase in consumption G and reduction of channel height h_k , since in this case the flow rate is increased and temperature difference along the channel is reduced; at the same time, heat exchange is intensified and the losses of temperature difference between heat carriers and thermoelement junctions are reduced. However, with increase in flow rate, the energy consumption on heat carrier pumping increase as well, which predetermines the presence of optimal values of parameters G and h_k , assuring the achievement of maximum TEG power and efficiency. The effect of regime parameters on the TEG power and efficiency is illustrated in Figs. 5 and 6.

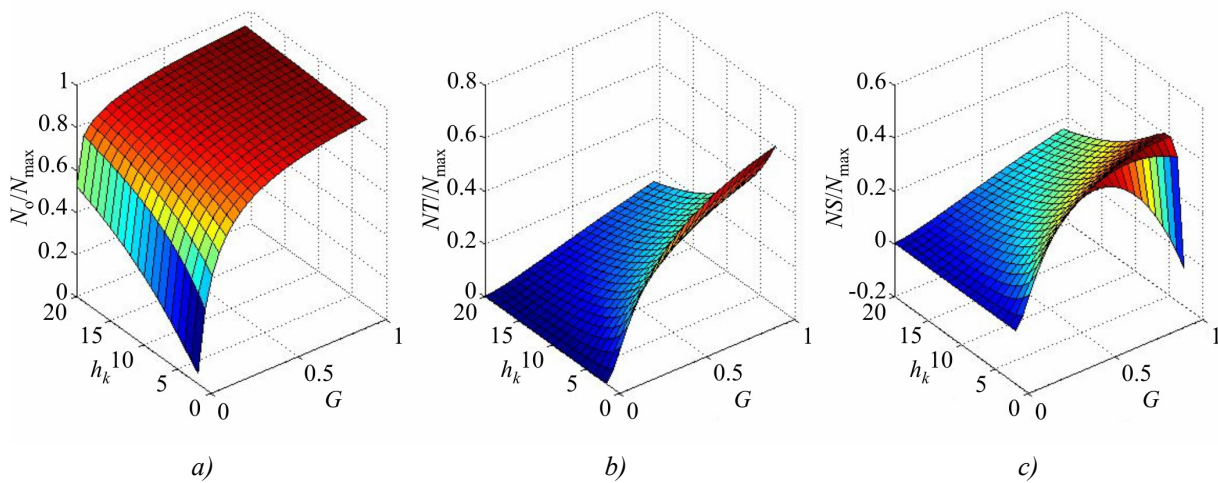


Fig. 5. Effect of regime parameters on the TEG power; a) – effect of heat exchange losses on the junctions; b) – effect of temperature difference along the channel; c) – effect of electricity consumption on heat carrier pumping.

Power losses due to irreversibility of heat exchange between the heat carrier and thermoelement junctions are of the order of 7 %; the losses from the reduction of temperature difference along the channel can reach 30 %; the losses for heat carrier pumping make 15 %...20 % from maximum possible generator power. As a result, maximum net power of TEG is of the order of 40 % of the theoretically possible.

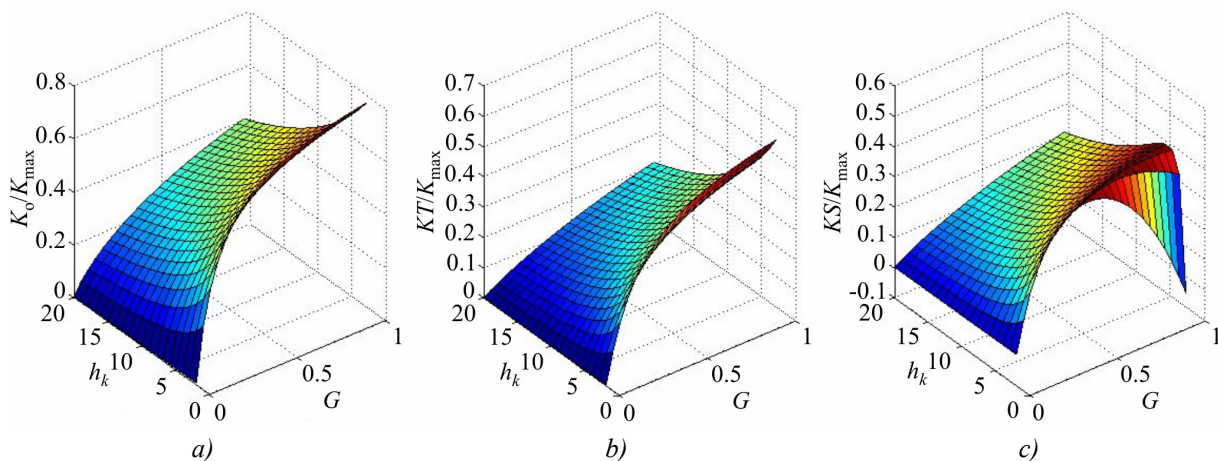
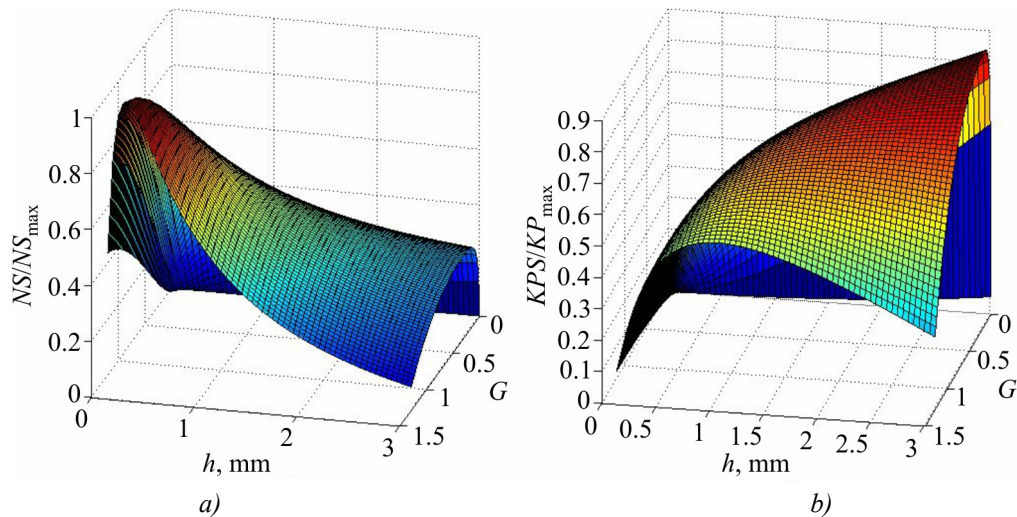


Fig. 6. Effect of regime parameters on the TEG efficiency; a) – effect of heat exchange losses on the junctions; b) – effect of temperature difference along the channel; c) – effect of electricity consumption on heat carrier pumping.

Efficiency reduction due to the losses in question amounts to nearly 60 % as compared to theoretical efficiency for the available temperature difference. The optimal channel height for given conditions is $h_k \approx 5$ mm, the optimal heat carrier flow rate is $G = 0.9$ kg/s. The dependences of the TEG power and efficiency on the height of thermoelements at the optimal G and h_k are given in Fig. 7.



*Fig. 7. Effect of thermoelement height on the TEG characteristics.
a) – dimensionless power of TEG; b) – relative efficiency of TEG.*

As is evident from the above data, there is an optimal value of h assuring maximum TEG power (in the case under study $h_{opt} \approx 0.3$ mm). However, the generator efficiency with increase in h grows monotonously. Hence it follows that the value of h optimal in terms of maximum economic efficiency of device should be selected with regard to cost characteristics of both generator and heat energy source.

Conclusions

A mathematical model of heat-exchange type thermoelectric generator is represented, assuring the possibility of calculation and optimization of such device parameters.

Performance analysis of a TEG integrated into a plate heat exchanger is made, the domain of problem definition is specified and the estimates of optimal TEG parameters are obtained.

References

1. Yu.M. Lobunets, Thermoelectric Generator, *Patent of Ukraine №8357* of 27.08.2013.
2. V.P. Isachenko, V.A. Osipova, and A.S. Sukomel, *Heat Transfer* (Moscow: Energiya, 1969), 440 p.
3. Yu.M. Lobunets, *Methods for Calculation and Design of Thermoelectric Power Converters* (Kyiv: Naukova Dumka, 1989), 175p.
4. Yu.M. Lobunets, Performance Evaluation of OTEC with Thermoelectric Power Converter, *J. Thermoelectricity* **1**, 62 – 67 (2013).
5. Yu.M. Lobunets, Solar Pond with Thermoelectric Energy Converter, *J. Thermoelectricity* **2**, 95 – 99 (2013).

Submitted 15.01.2014.

M.P. Volkov¹, I.A. Drabkin², L.B. Yershova¹, D.A. Kondratyev¹

¹“Company RMT” LTD, 22, Larin Str., Nizhniy Novgorod, 603152, Russia;

²State Scientific-Research and Design Institute of Rare-Metal Industry (“Giredmet” JSC),
5/1, B. Tolmachevsky lane, Moscow, 119017, Russia

DYNAMICS OF TRANSIENT PROCESSES IN MULTI-STAGE THERMOELECTRIC MODULES

The dynamics of reaching the operating mode by thermoelectric cooler (TEC) is an important characteristic for any device where it is employed, and the methods for computational and experimental determination of its parameters are rather relevant. In paper [1], the expressions for time relaxation of a unit leg and a single-stage TEC were derived and generalized for the case of a two-stage TEC under different thermal load and operating conditions. These results were experimentally verified in [2]. The purpose of this paper is to get a method for estimating the relaxation time of transient processes in TEC with any number of stages, to study theoretically and experimentally the dynamic curves of reaching the steady-state mode by TEC and to compare the measured and calculated results.

Key words: multi-stage thermoelectric module, time constant, relaxation time.

Introduction

The time necessary to reach the operating mode (relaxation time) of a multi-stage thermoelectric module is of significant applied relevance. We understand the module relaxation time as a time during which the temperature deviation from the equilibrium value of the module is reduced by the factor e .

Numerous attempts have been made to estimate the relaxation time of multi-stage modules [1, 2, 3], however, they are rather a matter of judgment, disregarding important design details of module. In paper [4] the method of calculation of non-stationary mode for multistage thermoelectric modules is offered. In this paper we also solve the one-dimensional time-dependent heat conduction equation for a multi-stage TEC as accurately as possible, give the method of calculation of a multistage module relaxation time and compare the results with experimental data.

Problem solution method

Let us consider a multi-stage module (Fig. 1).

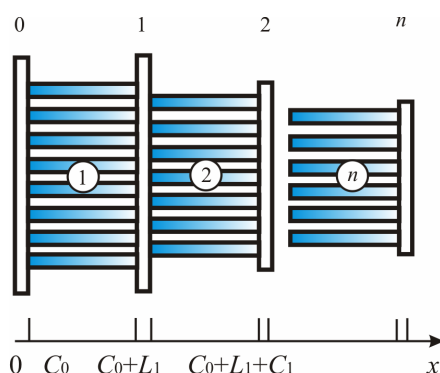


Fig. 1. Schematic of a multi-stage module.

In the figure, module stages are numbered, starting from the “hottest” stage. Stage numbers are indicated in circles. The hot side temperature of i -th stage will be denoted as T_i , the cold side temperature – T_{0i} . The first stage is connected to heat sink that has the temperature T_a . Heat spreader numbers start from 0 and are given at the top of the figure. The thickness of i -th heat spreader is C_i , the length of leg of i -th stage is L_i .

Let temperature distribution along the module be described by function $T(t, x)$, where t is time, x is coordinate. If (\cdot) x is in the region of heat spreader, then $T(t, x)$ meets the equation

$$\frac{\partial T_{i,c}(t, x)}{\partial t} = a_c^2 \frac{\partial^2 T_{i,c}(t, x)}{\partial x^2}, \quad (1)$$

where symbol i indicates ceramics number, and a_c – heat spreader thermal diffusivity:

$$a_c = \sqrt{\frac{\kappa_c}{c_c d_c}}, \quad (2)$$

where κ_c is thermal conductivity of heat spreader material, c_c is its heat capacity, and d_c is density.

If (\cdot) x is in the region of legs, then

$$\frac{\partial T_{i,ty}(t, x)}{\partial t} = a_{i,ty}^2 \frac{\partial^2 T_{i,ty}(t, x)}{\partial x^2} + \frac{J^2}{c_{i,ty} d_{i,ty} \sigma_{i,ty}}, \quad (3)$$

where i is stage number, symbol ty is used to designate the type of leg conductivity $ty = n, p$, respectively, $a_{i,ty} = \sqrt{\frac{\kappa_{i,ty}}{c_{i,ty} d_{i,ty}}}$ is temperature conductivity of the leg of ty type, and $\kappa_{i,ty}$, $c_{i,ty}$, $d_{i,ty}$ is thermal conductivity, heat capacity and density of the leg of ty type in i -th stage. For simplicity, all the legs will be assumed to be connected in series, so current density J depends neither on conductivity type ty , nor on stage number, $\sigma_{i,ty}$ is electric conductivity of the leg of i -th stage and ty type.

From the condition of continuity of temperatures it follows that at the boundary of ceramics and legs the following relations are fulfilled

$$T_{0,c}(t, C_0) = T_{1,ty}(t, C_0), \quad (4)$$

$$T_{k,c}\left(t, \left[C_0 + \sum_{i=1}^{i=k} (C_i + L_i) \right]\right) = T_{k,ty}\left(t, \left[C_0 + \sum_{i=1}^{i=k} (C_i + L_i) \right]\right), \quad k = 1, \dots, n, \quad (5)$$

$$T_{k-1,c}\left(t, \left[\sum_{i=1}^{i=k} (C_{i-1} + L_i) \right]\right) = T_{k,ty}\left(t, \left[\sum_{i=1}^{i=k} (C_{i-1} + L_i) \right]\right), \quad k = 1, \dots, n. \quad (6)$$

We will assume heat flow through the legs of thermoelectric module to be uniformly distributed along the heat spreader section. In this case the one-dimensional approximation remains valid. For the zero heat spreader or for the cold ends of legs of any one of stages such assumption seems quite natural, since the legs are distributed along the ceramic surface uniformly enough. As regards the hot ends of legs for stages starting from the second one, the legs there are distributed along the area which is appreciably smaller than the total area of the heat spreader and such an assumption for them looks somewhat non-natural. Condition for continuity of heat flows will yield on the heat spreader-leg contact with regard to (5), (6)

$$-S_{i-1} k_c \frac{\partial T_{i,c}(t, x)}{\partial x} + N_i s \sum_{ty=n,p} \left(k_{ty} \frac{\partial T_{i,ty}(t, x)}{\partial x} + \alpha J T_c(t, x) \right) \Big|_{x=C_0, C_0 + \sum_{i=1}^{i=k} (C_i + L_i)} = 0, \quad ty = n, p, \quad k = 1, \dots, n, \quad (7)$$

where S_{i-1} is the area of i -th heat spreader, N_i is the number of thermoelement pairs, s is cross-section of thermoelement legs (equal for both conductivity types). Introducing a designation for filling factor of k -th ceramics of i -th stage

$$K_{i,k} = \frac{2N_i s_i}{S_k}, \quad k = i, i-1, \quad (8)$$

we can write (7) in the form

$$\left(k_n \frac{\partial T_{i,n}(t,x)}{\partial x} + k_p \frac{\partial T_{i,p}(t,x)}{\partial x} \right) - \frac{2k_c}{K_{i,i-1}} \frac{\partial T_{i-1,c}(t,x)}{\partial x} + \bar{\alpha}_i J T_{i,c}(t,x) \Big|_{x=C_0, C_0 + \sum_{i=1}^{i=k} (C_i + L_i)} = 0, \quad (9)$$

where $\bar{\alpha}_i = (\alpha_{in} + \alpha_{ip}) / 2$.

Similarly, on the leg-heat spreader contact with regard to (4) we have

$$k_c \frac{\partial T_c(t,x)}{\partial x} - \frac{K_{i,i}}{2} \left(k_n \frac{\partial T_n(t,x)}{\partial x} + k_p \frac{\partial T_p(t,x)}{\partial x} \right) - K_{i,i} \bar{\alpha} J T_{ty}(t,x) \Big|_{\sum_{i=1}^{i=k} (C_{i-1} + L_i)} = 0, \quad k = 1, \dots, n. \quad (10)$$

The boundary conditions on the cold heat spreader of module:

$$\kappa_c \frac{\partial T_{n,c}(t, C_0 + \sum_{i=1}^{i=n} (C_i + L_i))}{\partial x} = q_0, \quad (11)$$

where q_0 is the density of heat flow to the cold heat spreader of module.

The initial conditions:

$$T_c(0, x) = T_a. \quad (12)$$

We will sought for the solution of (1) in the form

$$T(t, x) = \tau(t) \varphi(x) + \varphi_{st}(x), \quad (13)$$

where $\varphi_{st}(x)$ is a solution of the steady-state thermal conductivity equation with the same conditions (4) – (10) as for the non-steady solution of thermal conductivity. By virtue of definition (13), function $\varphi(x)$ satisfies Eq.(1) and Eq. (3), where the last term is equal to 0. Functions $\varphi(x)$ on the heat spreader and legs are sewn by means of Eqs. (4) to (10). On the cold heat spreader for the last stage $\varphi(x)$ satisfies Eq.(11) where $q_0 = 0$. The initial conditions for function $\varphi(x)$:

$$\varphi_0(x) = T_a - \varphi_{st}(x). \quad (14)$$

Characteristic numbers λ are found by the method of dividing variables from equation

$$\frac{\partial \tau(t)}{\tau(t) \partial t} = a^2 \frac{d^2 \varphi(x)}{\varphi(x) dx^2} = -\lambda_j^2. \quad (15)$$

The solution of Eq.(15) in the region of i -th heat spreader is of the form:

$$\varphi_{i,c}(x) = A_{i,c} \sin \frac{\lambda_j x}{a_c} + B_{i,c} \cos \frac{\lambda_j x}{a_c}, \quad i = 1, \dots, n, \quad (16)$$

where $A_{i,c}$ and $B_{i,c}$ are integration constants.

In the region of thermoelectric material

$$\varphi_{i,ty}(x) = A_{i,ty} \sin \frac{\lambda_j x}{a_{ty}} + B_{i,ty} \cos \frac{\lambda_j x}{a_{ty}}, \quad i = 1, \dots, n, \quad ty = n, p, \quad (17)$$

where $A_{i,ty}$, $B_{i,ty}$ are integration constants.

If the solution in the region of heat spreader is known, the solution in the region of legs can be found from (4) – (10) by solving a simple linear system of equations

$$\left\{ \begin{array}{l} A_{i,n} \sin \frac{\lambda_j L}{a_n} + B_{i,n} \cos \frac{\lambda_j L}{a_n} = T_{cer} \\ A_{i,p} \sin \frac{\lambda_j L}{a_p} + B_{i,p} \cos \frac{\lambda_j L}{a_p} = T_{cer} \\ A_{i,n} \sin \frac{\lambda_j (L + L_i)}{a_n} + B_{i,n} \cos \frac{\lambda_j (L + L_i)}{a_n} - A_{i,p} \sin \frac{\lambda_j (L + L_i)}{a_p} - B_{i,p} \cos \frac{\lambda_j (L + L_i)}{a_p} = 0 \\ A_{i,n} \frac{\kappa_n \lambda_j}{a_n} \cos \frac{\lambda_j L}{a_n} - B_{i,n} \frac{\kappa_n \lambda_j}{a_n} \sin \frac{\lambda_j L}{a_n} + A_{i,p} \frac{\kappa_p \lambda_j}{a_p} \cos \frac{\lambda_j L}{a_p} - B_{i,p} \frac{\kappa_p \lambda_j}{a_p} \sin \frac{\lambda_j L}{a_p} = \frac{\kappa_c}{K_{i-1,i}} D_{cer} \end{array} \right. \quad (18)$$

Here, the following designations are introduced:

$$L = \sum_{m=0}^{m=i} (C_m + L_m) \quad i = 0, 1, \dots, n; L_0 = 0,$$

$$T_{cer} = \varphi_{i-1,c}(L) \quad D_{cer} = A_{i-1,c} \frac{\lambda_j}{a_c} \cos \frac{\lambda_j L}{a_c} - B_{i-1,c} \frac{\lambda_j}{a_c} \sin \frac{\lambda_j L}{a_c}. \quad (19)$$

If the solution in the region of legs is known, in the region of heat spreader the solution will be found from expressions (4) – (10):

$$B_{i,c} = T_{mater} \cos \frac{\lambda_j L}{a_c} - q_{mater} \sin \frac{\lambda_j L}{a_c}, \quad A_{i,c} = T_{mater} \sin \frac{\lambda_j L}{a_c} + q_{mater} \cos \frac{\lambda_j L}{a_c}, \quad i = 1, \dots, n \quad (20)$$

where the following designations are used:

$$\begin{aligned} L &= \sum_{m=1}^i (C_{m-1} + L_m), \quad T_{mater} = A_{i,ty} \sin \frac{\lambda_j L}{a_{ty}} + B_{i,ty} \cos \frac{\lambda_j L}{a_{ty}}, \quad q_{mater} = \frac{a_c K_{i,i} (\kappa_{ni} D_{ni} + \kappa_{pi} D_{pi} + \bar{\alpha}_i J T_{mater})}{\kappa_c \lambda_i}, \\ D_{ty,i} &= A_{i,ty} \frac{\lambda_j}{a_{ty}} \cos \frac{\lambda_j L}{a_{ty}} - B_{i,ty} \frac{\lambda_j}{a_{ty}} \sin \frac{\lambda_j L}{a_{ty}} \quad ty = n, p. \end{aligned} \quad (21)$$

The solution for the 0 ceramics is given by:

$$\varphi_{0,c}(x) = \sin \frac{\lambda_j x}{a_c}, \quad x \in [0, D_0], \quad (22)$$

where coefficient $A_{0,c} = 1$, which does not restrict the generality of solution, since the equation for finding λ_j includes the ratio of coefficients.

Solving consecutively the equations (18) and (20) for all the stages, we can obtain the equation for finding characteristic numbers

$$tg \left[\frac{\lambda_i \left(C_0 + \sum_{i=1}^n (C_i + L_i) \right)}{a_c} \right] - \frac{A_{n,c}}{B_{n,c}} = 0 \quad (23)$$

Relaxation times are related to characteristic numbers in conformity with (15):

$$\tau_i = \left(\frac{1}{\lambda_i} \right)^2. \quad (24)$$

The resulting relaxation time of module is selected as the largest of the set of times (24).

In the above equations the temperature dependences of thermoelectric parameters are disregarded. To take into account the temperature dependences, an approximate compromise decision was taken. The values of thermoelectric parameters for each stage were assumed to be constant, but their values were taken for i -th stage at the temperature of legs on the “hot” heat spreader T_i .

Experimental results

The calculated relaxation time was compared to the experimentally obtained data, as well as to the data of previous works. In Table 1 are listed the values obtained for two-stage modules 2MC06-023-12 and 2MC06-043-05. Here I is measuring current, τ is the value of relaxation time calculated by the foregoing method, τ_{exp} is the measured relaxation time, τ_{appr} is the approximate value of relaxation time calculated as the sum of maximum stage-by-stage times at zero current [1, 2]. All the values were obtained in vacuum at the temperature of the hot heat spreader 50 °C.

Table 1
Experimental and calculated values of relaxation times

TE module	I , mA	τ_{exp} , s	τ , s	τ_{appr} , s
2MC06-023-12	300	9.94	9.50	12.7
2MC06-043-05	700	3.19	3.68	3.22

The following parameters were used in the calculations: for thermoelectric material the heat capacity was 0.13 J/g, the density – 7.5 g/cm³, for ceramics – 0.8 J/g and 3.5 g/cm³, for solder – 0.17 J/g and 9.3 g/cm³, respectively, ceramics thickness was 0.5 mm.

The measurements were performed as follows. At given current, the temperature on thermoelectric module was measured as a function of time and maximum temperature difference ΔT_{max} was found. After that we constructed the dependence $\ln\left(1 - \frac{\Delta T}{\Delta T_{max}}\right)$, and τ_{exp} was determined by the inverse value of linear approximation slope ratio.

Figs. 2 and 3 explain experimental determination of the relaxation time.

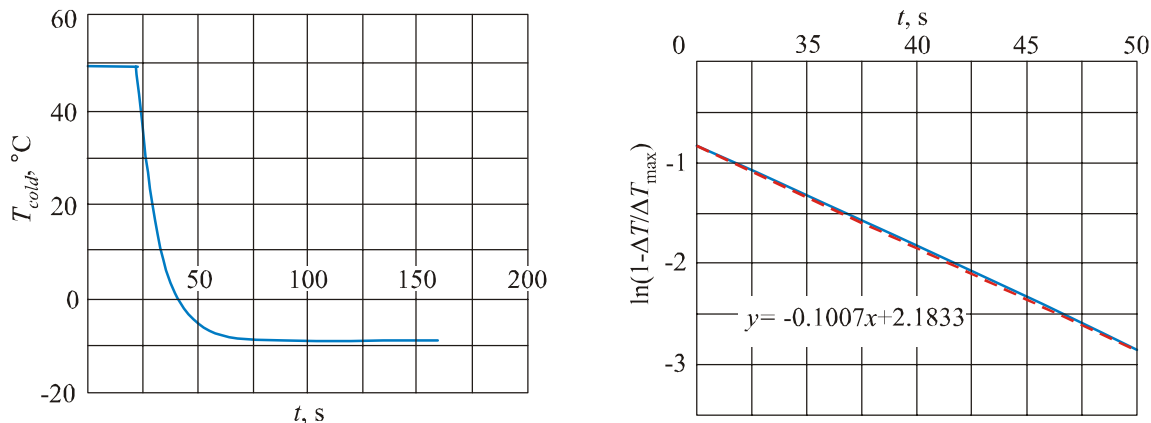


Fig. 2. Finding the relaxation time τ_{exp} of TE module 2MC06-023-12.

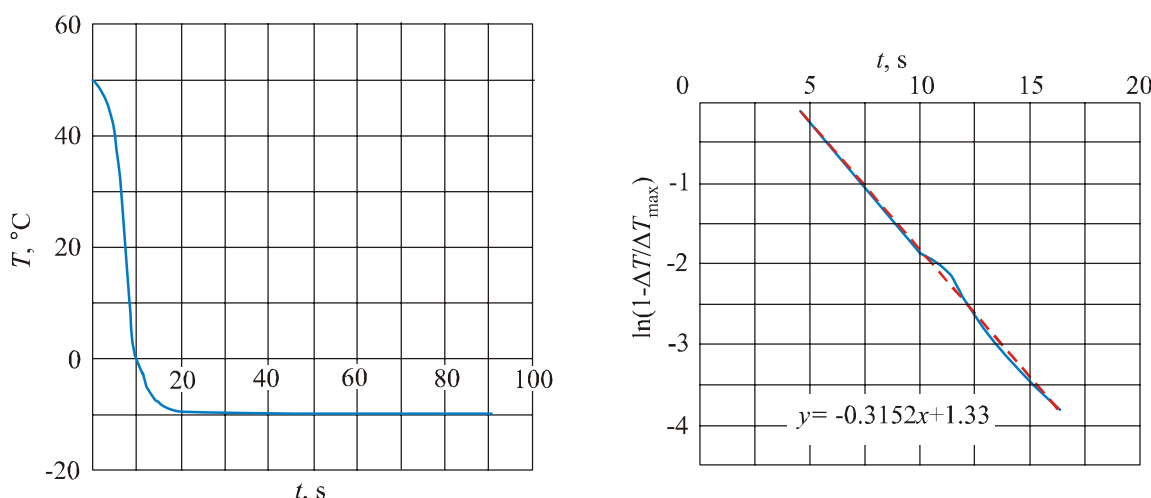


Fig. 3. Finding the relaxation time τ_{exp} of TE module 2MC06-043-05.

It is important to note the specificity of measuring the relaxation time of multi-stage modules. For this purpose the method of measurement on setting the steady-state voltage [2] is, generally speaking, not legitimate, though for a single-stage module where thermoEMF voltage is proportional to temperature difference, it certainly works. On setting the steady-state voltage value, the multi-directional variation of leg temperatures still takes place for some time, so the relaxation time measured by the thermoEMF voltage proves to be underrated.

Conclusion

The elaborated technique is a general method for calculation of the relaxation time of thermoelectric module with any number of stages for arbitrary current.

The calculated results were compared to the relaxation time values measured for two-stage modules. The calculated values are in satisfactory agreement with theoretical ones. Note, however, that it is necessary to supplement the experimental data for modules with more than two stages and perform further comparative analysis.

An important point is that we succeeded in showing that the approximate value of relaxation time calculated as the sum of maximum stage-by-stage times at zero current [1, 2] is rather good approximation. This approximate method can be easily used for solving urgent practical problems of estimating the dynamics of transient processes in thermoelectric modules.

References

1. I.A. Drabkin, Transient Processes in Cooling Thermoelectric Modules and Devices, In: "Thermoelectrics and Their Applications" (Saint-Petersburg, 2002, p. 287 – 295).
2. V.V. Volodin, I.A. Drabkin, L.B. Yershova, and D.A. Kondratyev, Methods for Research on Temporal Dynamics of Thermoelectric Modules in Z-metering, In: "Thermoelectrics and Their Applications" (Saint-Petersburg, 2002, p. 264 – 269).
3. Yu.I. Ravich, A.I. Gordienko, Method for Calculation of Transient Process Time of Multi-Stage Cooling Thermopile, *Semiconductors* **41** (1), 112 – 116 (2007).
4. A.L. Vainer, V.I. Perepeka, Unsteady operating mode of thermopiles, *J. Thermoelectricity* **2**, 15 – 20 (2008).

Submitted 24.02.2013.



Yu.M. Lobunets

Yu.M. Lobunets

Institute of Thermoelectricity of the NAS and MES Ukraine,
1, Nauky Str., Chernivtsi, 58029, Ukraine

OPTIMIZATION OF THERMAL SCHEMES OF THERMOELECTRIC GENERATOR WITH CONSTANT-POWER HEAT SOURCE

A scheme of thermoelectric generator (TEG) with constant-power heat source (radiating surface with fixed temperature) is considered. With specific reference, the peculiarities of scheme presented here caused by strict restrictions on device thermal conditions are analyzed. A solution is proposed assuring the possibility of drastic improvement of techno-economic and mass-dimensional characteristics of TEG due to transformation of heat fluxes at heat supply and removal.

Key words: thermoelectric generator, heat scheme of TEG, TEG efficiency.

Introduction

The specific features of heat source employed have a considerable impact on the performance of thermoelectric generators (TEG) and largely determine the choice of device thermal scheme and its techno-economic figures. In the classification of TEG by the heat source type, a method of heat supply to thermopiles, namely due to convection, radiation or thermal conductivity, is commonly used as a governing criterion [1, 2]. One of particular cases of this problem is the use of heat sources with given power of heat release, such as radioisotope sources of thermal energy [3] or radiation sources [4]. In some cases the problem is complicated by introducing additional restrictions, such as restrictions on the temperature of radiating surface [5], narrowing problem definition domain. This creates additional rigid relations in the heat source-TEG-heat sink system determining the peculiarities of solving the optimization problems of TEG parameters. The purpose of this paper is to analyze the characteristics of TEG with constant-power heat source under additional restrictions on the temperature conditions.

Problem formulation

Let us consider the problem of calculation and optimization of TEG with constant-power heat source under given restrictions on the temperature of radiating surface and the temperature of heat-absorbing junctions. Conditions for the uniqueness of the problem: $T_o = \text{const}$ is radiator temperature; $q = \text{const}$ is heat flux on heat absorber surface; $T_h = \text{const}$ is heat absorber temperature; $t_x = \text{const}$ is heat sink temperature.

Such problem formulation severely restricts heat transfer conditions in the heat source-TEG-heat sink system. In [5], a problem in similar formulation is considered in detail and the conditions of equilibrium in the heat source (cement kiln surface) – heat absorber system are determined. As the initial data, we will use the values and results given in this paper:

$$\begin{aligned}
 q &= 4.5 \text{ kW/m}^2; \\
 T_o &= 300 \text{ }^\circ\text{C}; \\
 T_h &= 80 \dots 170 \text{ }^\circ\text{C}; \\
 t_x &= 30 \text{ }^\circ\text{C};
 \end{aligned} \tag{1}$$

The specific feature of scheme under consideration is that to maintain given boundary conditions it is also necessary to assure strictly defined value of thermal resistance on the heat absorbing surface-heat sink area, otherwise it would be impossible to fulfill the condition of constant radiator temperature ($T_o = \text{const}$) and heat flux

$$q = K(T_h - t_x) = \text{const}, \tag{2}$$

where $K = \frac{1}{\frac{1}{\alpha_x} + \frac{h}{\lambda} + \frac{2\delta}{\lambda k}}$ is heat transfer coefficient; α_x is coefficient of heat exchange at heat removal; h is thermoelement height; λ is thermal conductivity coefficient of thermoelectric material; δ is heat spreader thickness; λ_k is heat spreader thermal conductivity.

The values of heat transfer coefficient K satisfying conditions (1, 2) are shown in Fig. 1.

As is seen from (2), the ratio between the net temperature difference on thermoelements, $\Delta T = (T_h - T_x)$, and the available difference $(T_o - t_x)$ is proportional to the ratio between thermal resistance of thermoelement legs (h/λ) and thermal resistances.

The thermoelement height satisfying conditions (2) is:

$$h_{opt} = \lambda / q[(T_h - t_x) - 1/\alpha_x - 2\delta/\lambda k] \tag{3}$$

That is, under known cooling conditions (α_x) there is always only one value of thermoelement height satisfying the conditions of the problem. The permissible values of h_{opt} versus α_x for the initial data (1) are illustrated in Fig. 2.

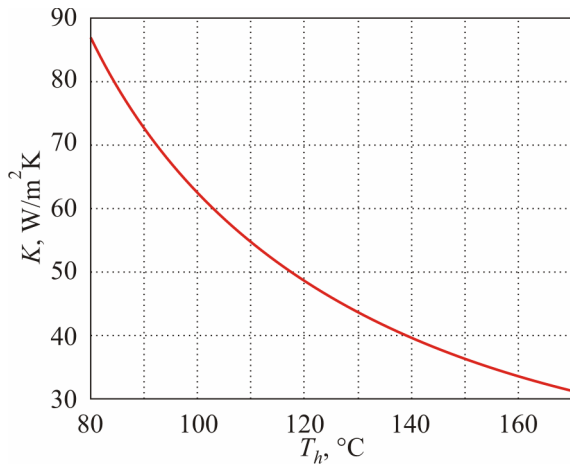


Fig. 1. Dependence of heat transfer coefficient K on temperature T_h .

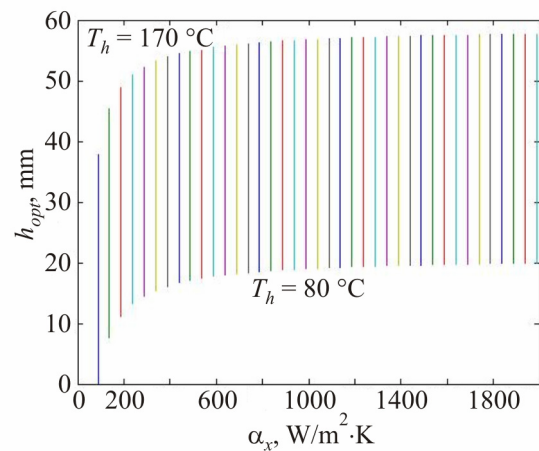


Fig. 2. Dependence of permissible thermoelement height h_{opt} mm, on heat exchange intensity α_x W/m²K for $T_h = 80 \dots 170$ °C.

As it follows from the data given in the figure, the problem definition domain lies in the zone of unacceptably high values of h_{opt} . Whereas the use of thermoelements of standard height will reduce considerably the net temperature difference and TEG power, respectively. For instance, for

thermoelements 1.5 mm high (typical height for standard thermoelectric modules) the established restrictions are matched by heat exchange coefficient $\alpha_x = 35 \text{ W/m}^2\text{K}$. In so doing, the net temperature difference will make of the order of 3.5 K, and the specific power of TEG will not exceed $N = 3 \text{ W/m}^2$. In the limiting case, at $h \rightarrow 0$, the equilibrium in the system is assured at $\alpha_{x\min} = q/(T_h - t_x)$; $\Delta T = 0$, $N = 0$. The dependences of TEG specific power on heat exchange intensity and the temperature of heat absorbing surface T_h at the optimal height of thermoelements is illustrated in Fig. 3.

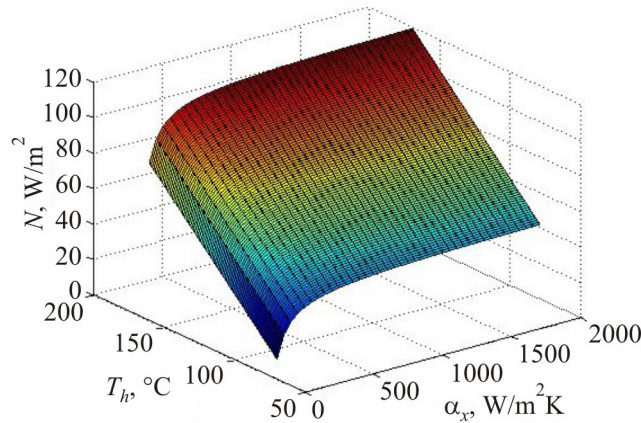


Fig. 3. Dependence of TEG specific power N , W/m^2 , on the temperature of heat-absorbing layer T_h and heat exchange coefficient α_x , $\text{W/m}^2\text{K}$.

An important feature which largely determines the cost of TEG is specific consumption of thermoelectric material per unit power g , kg/W .

In the first approximation, this parameter can be found from the known relations

$$N = \frac{E^2}{4R} = \frac{(e\Delta T)^2}{4\rho h},$$

In the limiting case

$$\Delta T \rightarrow (T_h - t_x) \rightarrow \frac{qh}{\lambda},$$

whence we get

$$g = \frac{4\lambda v}{zq^2} \quad (4)$$

where λ , v and z is thermal conductivity, density and figure of merit of thermoelectric material, respectively.

That is, in the problem formulation under study the specific consumption of thermoelectric material g depends only on heat flux q . For the initial data assumed this parameter calculated by (4) is equal to 1.2 kg/W. In fact, Eq.(4) yields maximum possible value of g , since it does not take into account the irreversible losses at heat removal. Actually, this value for given conditions (1) over a wide range of α_x variation is of the order of 4.7 kg/W. It is clear that despite possible achievement of the acceptable values of specific power and efficiency, such a TEG cannot find practical application because of too large consumption of thermoelectric material.

To reduce material consumption of TEG, measures must be taken to increase the density of heat fluxes at heat supply to thermoelements. For this purpose, intermediate coolant circuit can be used, which, on the one hand, will allow heat removal from the source under given restrictions, and, on the other hand, intensification of heat supply to TEG. For instance, for a design described in [5] it is reasonable to use a water jacket, namely vapour generator, the assigned temperature of which is easily stabilized by maintaining the necessary pressure of saturated vapours in the loop. The resultant vapour is directed to heat exchanger-thermoelectric generator [6]. This helps to release rigid relationship between the characteristics of heat source, TEG and heat sink. Due to high intensity of heat exchange at vapour condensation, the density of heat flows at heat supply to TEG increases by several orders, which allows a drastic reduction of mass-dimensional and cost characteristics of TEG. Preliminary evaluation of such device characteristics under the above formulated restrictions shows that at $T_h = 170$ °C the specific power of TEG will make of the order of 12 kW/m^2 , and material consumption – not more than 0.33 g/W . The generating part proper of such 200 kW TEG will represent a compact device of dimensions $500 \times 1000 \times 500$ mm, which is quite acceptable for the application discussed.

Conclusions

A scheme of thermoelectric generator with a constant-power heat source and restrictions on the temperature conditions is considered. Analysis of the scheme is made and it is shown that a decisive influence on techno-economic characteristics of similar TEG is produced by heat flux density restrictions. A decision is proposed assuring the possibility of drastic improvement of techno-economic and mass-dimensional characteristics of TEG due to transformation of heat fluxes at heat supply and removal.

References

1. L.I. Anatychuk, *Thermoelements and Thermoelectric Devices: Handbook* (Kyiv: Naukova Dumka, 1979), 768 p.
2. G.K. Kotyrlo, Yu.M. Lobunets, *Calculation and Design of Thermoelectric Generators and Heat Pumps: Handbook* (Kyiv: Naukova Dumka, 1980), 328 p.
3. *Radioisotope Sources of Electric Energy*, Ed. by G.M. Fradkin (Moscow: Atomizdat, 1978), 304 p.
4. L.I. Anatychuk, Yu.M. Mochenyuk, and A.V. Prybyla, Solar Thermoelectric Energy Converters, *J. Thermoelectricity* **4**, 75 – 82 (2013).
5. L.I. Anatychuk, Jenn-Dong Hwang, and V.V. Lysko, Thermoelectric Heat Recuperators for Cement Kilns, *J. Thermoelectricity* **5**, 41 – 48 (2013).
6. Yu.M. Lobunets, Thermoelectric Generator, *Patent of Ukraine №8357* of 27.08.2013.

Submitted 06.02.2014.

T.A. Ismailov¹, O.V. Yevdulov¹, M.A. Khazamova¹, R.A.-M. Magomadov²

¹Federal State Budget Educational Institution of Higher Professional Education “Dagestan State Technical University”, 70, Ave. Imam Shamil, Makhachkala, 367015, Russia;

²Federal State Budget Educational Institution of Higher Professional Education “Grozny State Oil Technical University”, 100, Ordzhonikidze Sq., Grozny, 364051, Russia

MATHEMATICAL MODEL OF A THERMOELECTRIC SYSTEM FOR LOCAL THERMAL EFFECT ON HUMAN HAND

The paper is concerned with a mathematical model of a thermoelectric system for thermal effect on human hand. The model is based on the numerical solution of a system of differential thermal conductivity equations for irregular-shaped bodies. Two-dimensional and one-dimensional plots of temperature variation in different zones of affected object are presented.

Key words: human hand, physiotherapy, thermal effect, temperature field, thermal model, mathematical model.

Introduction

Methods of local thermal effect are widely used in medical practice in the therapy and prophylaxis for stimulation of physiological processes. Thermal effect exerts significant influence on the energy balance of human organism. The reaction of vessels to thermal procedure propagates over the entire body surface, but it is most extensively expressed at a point of immediate application of heat. Under a local temperature effect, skin whose receptors sense pain (mechanical, thermal), temperature (cold, heat) and tactile stimulation is in the intimate contact with the temperature irritant. In so doing, blood flow in skin vessels varies by a factor of 100 to 180, and heat transfer regulation takes place mostly due to a change in blood flow, especially in the tissues of hands and feet [1].

This serves the basis for a number of methods employed in physiotherapeutic practice to which we can refer baths with gradually increased temperature (the Hauffe baths), contrast baths, partial (hand) baths, etc., as well as using various media, such as paraffin, ozokerite and others [2].

Partial or local baths include hydropathic procedures affecting certain part of the body. Wide application is enjoyed by hand baths with corresponding vessels made of galvanized iron [3]. In the process, a forearm, one or both hands, as well as the entire arm are immersed in water. The administered baths are of different temperature and duration, namely warm baths at water temperature 37 – 38° C of duration up to 20 – 30 minutes, hot baths at water temperature 40 – 44° C of duration from 10 to 20 minutes and cold baths at water temperature 8 – 14° C of duration from 5 to 12 minutes.

To intensify the irritant action, baths of contrast temperatures can be administered [4]. In so doing, two baths are used, one of which is filled with hot (40 – 45° C), and the other – with cold water (8 – 10° C). A patient alternatively immerses his hand first into hot water for 1 – 2 minutes, and then to cold water for 10 – 15 seconds, repeating this procedure several times. Cold hand baths are generally recommended at acute inflammatory processes on the hand, contrast baths – at hyperhidrosis, acrocyanosis, etc., hot baths – for infiltrate resolution, etc.

The disadvantages of the above methods of physiotherapeutic procedures include their low

efficiency and discomfort, complexity and inconvenience of realization, insufficient accuracy of thermal effect dosing.

The method of thermal effect discussed above can be realized through use of thermoelectric power converters [5]. In this case the above disadvantages are largely eliminated.

The purpose of this study is mathematical simulation, as well as theoretical studies of a thermoelectric system (TES) for thermal effect on human hand with a view to perform efficient physiotherapeutic and rehabilitation procedures.

Zone model

The object of study is a device in the form of a construction comprising a flexible elastic base with embedded thermoelectric modules that have flexible metal heat leveling plates on their junctions (Fig. 1). The device is brought into intimate thermal contact with the affected object (human hand zone).



Fig. 1. The appearance of TES for a local thermal effect on human hand.

A thermal model of TES realizing physiotherapeutic procedures on the middle third of the arm is given in Fig. 2. In conformity with the specific operation of TES realizing thermal effect so that thermal flux from the device is directed normal to the surface of hand, the thermal model of affected zone on which basis the system is calculated, has the appearance shown in Fig. 2. Here, the following parts should be pointed out: 1 – skin cover, 2 – muscular tissue and 3 – bone tissue, distinguished by thermophysical parameters and the level of internal heat release.

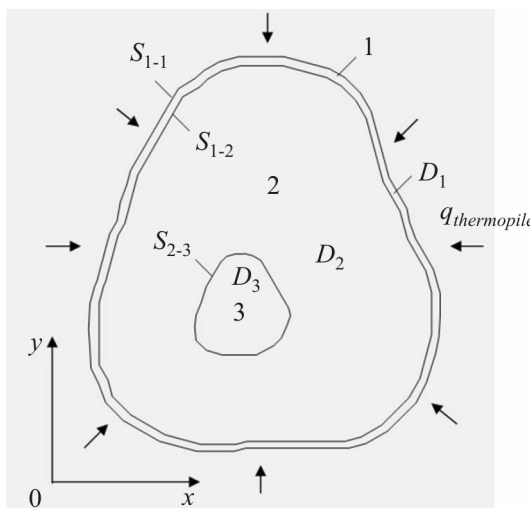


Fig. 2. Thermal model of TES realizing physiotherapeutic procedures on the middle third of the arm.

Let the area restricted by skin cover be denoted as D_1 , by muscular tissue – as D_2 , by bone tissue – as D_3 , the surface of skin cover contacting to TES – as S_{1-1} , to muscular tissue – as S_{1-2} , the surface of muscular tissue contacting to bone tissue – as S_{2-3} , S'_{2-3} . Then a description of thermophysical processes occurring in human arm thermally affected by TES in the generalized mathematical form can be represented as follows:

– with effect on the middle third of the arm

$$\begin{aligned} a_1 \frac{\partial^2 T_1}{\partial x^2} + a_1 \frac{\partial^2 T_1}{\partial y^2} + \frac{Q_{vn1}}{c_1 \rho_1} &= \frac{\partial T_1}{\partial \tau} \quad \text{at } x, y \in D_1; \\ a_2 \frac{\partial^2 T_2}{\partial x^2} + a_2 \frac{\partial^2 T_2}{\partial y^2} + \frac{Q_{vn2}}{c_2 \rho_2} &= \frac{\partial T_2}{\partial \tau} \quad \text{at } x, y \in D_2; \\ a_3 \frac{\partial^2 T_3}{\partial x^2} + a_3 \frac{\partial^2 T_3}{\partial y^2} + \frac{Q_{vn3}}{c_3 \rho_3} &= \frac{\partial T_3}{\partial \tau} \quad \text{at } x, y \in D_3; \end{aligned} \quad (1)$$

$$T_1, T_2, T_3 = 309.6 \text{ K} \text{ at } \tau = 0;$$

$\lambda_1 \frac{\partial T_1}{\partial n_1} = \alpha (T_1 - T_{thermopile})$ at $x, y \in S_{1-1}$ – with a non-perfect contact between skin cover and the operating surface of TES;

$\lambda_1 \frac{\partial T_1}{\partial n_1} = q_{thermopile}$ at $x, y \in S_{1-1}$ – with a perfect contact between skin cover and the operating surface of TES;

$$\lambda_1 \frac{\partial T_1}{\partial n_1} = \lambda_2 \frac{\partial T_2}{\partial n_2} \text{ at } x, y \in S_{1-2};$$

$$\lambda_2 \frac{\partial T_2}{\partial n_2} = \lambda_3 \frac{\partial T_3}{\partial n_3} \text{ at } x, y \in S_{2-3};$$

where T_1, T_2, T_3, T'_3 are the temperatures of skin cover, muscular and bone tissue; a_1, a_2, a_3 are thermal diffusivity coefficients of skin cover, muscular and bone tissue; $\lambda_1, \lambda_2, \lambda_3$ are thermal conductivity coefficients of skin cover, muscular and bone tissue; c_1, c_2, c_3 is specific heat of skin cover, muscular and bone tissue; ρ_1, ρ_2, ρ_3 is the density of skin cover, muscular and bone tissue; $Q_{vn1}, Q_{vn2}, Q_{vn3}$ is the specific amount of heat released in skin cover, muscular and bone tissue; α is coefficient of heat exchange between skin cover and the operating surface of TES; $T_{thermopile}$ is the temperature of the operating surface of thermopile; $q_{thermopile}$ is the density of heat flux on the operating surface of thermopile; n_1, n_2, n_3 are normals to surfaces $S_{1-1}, S_{1-2}, S_{2-3}$, respectively; $n_i = (xh_i + yz_i)$; h, z are unit vectors; $i = 1 \dots 3$.

The system of equations (1) was solved by finite-element numerical method in conformity with procedure set forth in [6] and implemented in the Elcut applied software package. The results obtained make it possible to determine temperature variation at different points of the biological object, namely human arm, as well as to follow up its variation versus the value of heat flux from TES (cooling capacity and heating capacity of thermopiles) and the ambient conditions.

Simulation results

The numerical experiment was performed in conformity with the required conditions of physiotherapeutic procedures, namely the range of temperatures achieved by the biological object from 277 to 317 K, the duration of effect – from 10 to 30 minutes, possible alternation of cooling and heating the respective zone of a biological object.

The initial data was assumed as follows: $\lambda_1 = 0.407 \text{ W}/(\text{m}\cdot\text{K})$, $\lambda_2 = 0.439 \text{ W}/(\text{m}\cdot\text{K})$, $\lambda_3 = 0.34 \text{ W}/(\text{m}\cdot\text{K})$; $\rho_1 = 1036 \text{ kg}/\text{m}^3$, $\rho_2 = 1050 \text{ kg}/\text{m}^3$, $\rho_3 = 1036 \text{ kg}/\text{m}^3$; $c_1 = 3458 \text{ J}/(\text{kg}\cdot\text{K})$, $c_2 = 4020 \text{ J}/(\text{kg}\cdot\text{K})$, $c_3 = 3127 \text{ J}/(\text{kg}\cdot\text{K})$; $Q_{vn1} = 0$, $Q_{vn2} = 30 \text{ J}/(\text{kg}\cdot\text{s})$, $Q_{vn3} = 0$. The basic geometric dimensions of affected zones are shown in Fig. 3. The data is given in mm.

The calculated results are represented in Figs. 4 – 13.

Fig. 4 shows a two-dimensional temperature field of the middle third of the arm section exposed to cooling by TES under study with the value of thermal flux on the lateral surface of the biological object equal to $2500 \text{ W}/\text{m}^2$.

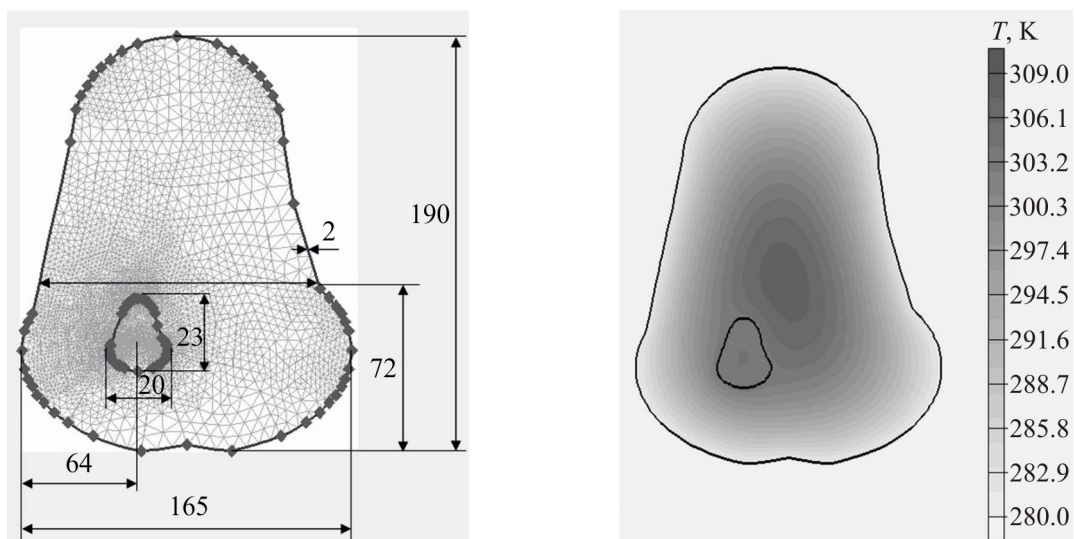


Fig. 3. A model of section of the middle third of the arm assumed in the calculation with the finite-element network and the basic dimensions.

Fig. 4. Two-dimensional temperature section field of the middle third of the arm in steady-state mode under cooling effect for $q_{thermopile} = 2500 \text{ W}/\text{m}^2$.

Figs. 5 and 6 show the respective one-dimensional plots of temperature distribution along the lateral axis on the section of the middle third of the arm, as well as along the lateral axis passing through the bone axis, in the steady-state mode. In so doing, for the case corresponding to Fig. 5 the values are considered for different heat flux values on the lateral surface of affected object equal to $q_{thermopile} = 2500 \text{ W}/\text{m}^2$, $q_{thermopile} = 2250 \text{ W}/\text{m}^2$, $q_{thermopile} = 2000 \text{ W}/\text{m}^2$. According to the data obtained, the temperature of the biological object is reduced with increase in $q_{thermopile}$. In this case maximum temperature reduction is approximately the same and is observed on skin cover layer at $q_{thermopile} = 2500 \text{ W}/\text{m}^2$, making 280 K. Accordingly, the temperature in the centre of the biological object varies only slightly by about 0.5 K which is due to the presence of internal heat release in thermally affected object, as well as due to its low thermal conductivity and relatively high heat capacity.

According to the above plots, the temperature distribution in the affected object depends in a certain way on the presence of bone tissue in its bulk. Under the assumed conditions that determine the absence of internal heat release in the bone tissue, such temperature variation is about 1 – 2 K with respect to the case when this object is absent in the bulk of the tissue.

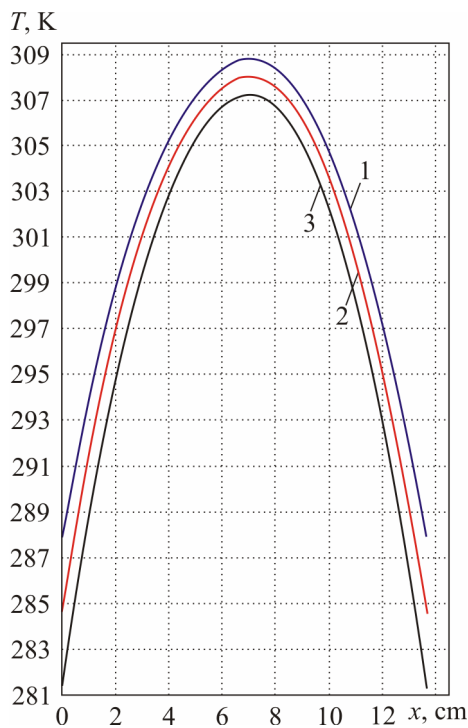


Fig. 5. Temperature distributions along the lateral axis of the middle third of the arm under cooling effect for different values of $q_{\text{thermopile}}$

$1 - q_{\text{thermopile}} = 2500 \text{ W/m}^2$, $2 - q_{\text{thermopile}} = 2250 \text{ W/m}^2$,
 $3 - q_{\text{thermopile}} = 2000 \text{ W/m}^2$.

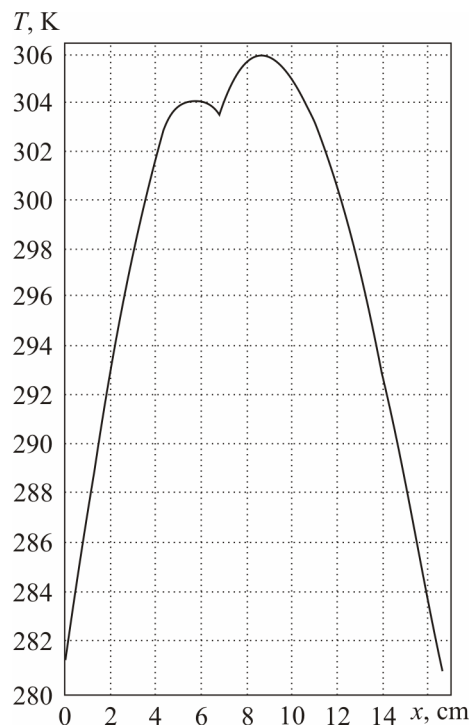


Fig. 6. Temperature distribution along the lateral axis of the bone tissue of the middle third of the arm under cooling effect for $q_{\text{thermopile}} = 2500 \text{ W/m}^2$.

Fig. 7 depicts a two-dimensional temperature field on the section of the middle third of the arm thermally affected by TES under study with the heat flux value on the lateral surface of the biological object equal to 700 W/m^2 . The respective one-dimensional plots are given in Fig. 8. These dependences are mainly similar to those given for the case of TES operation in cooling mode. The difference lies in temperature rise of the affected object with increase in $q_{\text{thermopile}}$ value, as well as in the lower values of thermopile power requirement for keeping temperature mode of the biological object corresponding to performance of physio-therapeutic procedures. Under the conditions discussed above the maximum temperature rise on skin cover of the middle third of the arm was obtained at $q_{\text{thermopile}} = 700 \text{ W/m}^2$, making 315 K. For the case of TES operation in heating mode the availability of bone tissue in the bulk of the biological object also introduces relevant changes into the structure of its temperature field. The above influence is identical to the case of TES operation in cooling mode and amounts to 1 – 2 K.

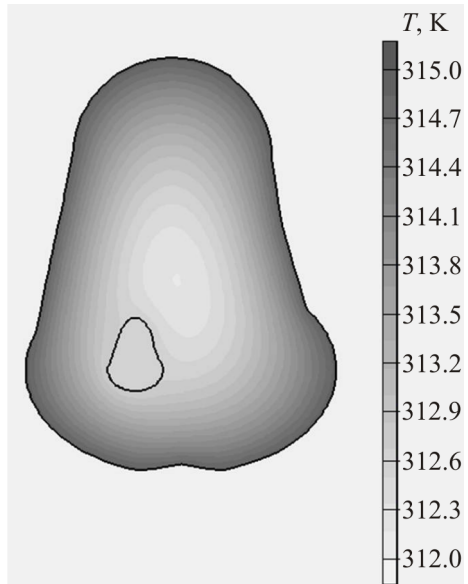


Fig. 7. Two-dimensional temperature field on the section of the middle third of the arm in steady-state mode under heating effect for $q_{\text{thermopile}} = 700 \text{ W/m}^2$.

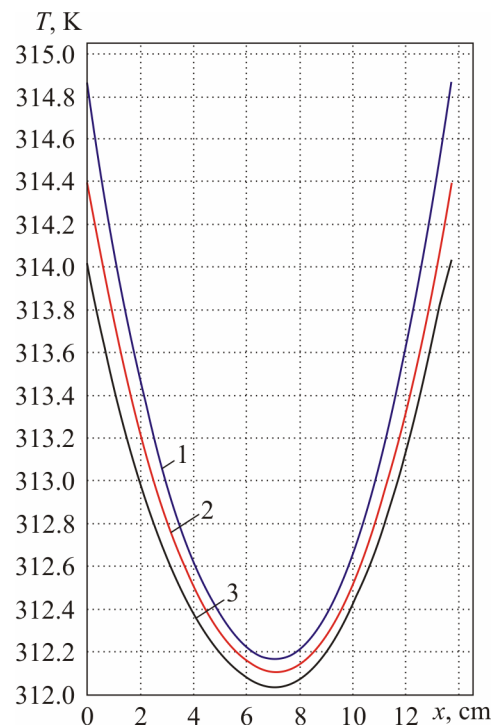


Fig. 8. Temperature distribution along the lateral axis of the middle third of the arm under heating effect for different $q_{\text{thermopile}}$ values 1 – $q_{\text{thermopile}} = 700 \text{ W/m}^2$, 2 – $q_{\text{thermopile}} = 650 \text{ W/m}^2$, $q_{\text{thermopile}} = 600 \text{ W/m}^2$.

Fig. 9 depicts a two-dimensional steady-state temperature field on the section of the middle third of the arm for the case corresponding to contrast thermal effect, when heat flux $q_{\text{thermopile},c} = -3500 \text{ W/m}^2$ is directed to the right surface of the biological object, and $q_{\text{thermopile},h} = 1000 \text{ W/m}^2$ – to the left surface. The respective one-dimensional plots showing temperature distribution on the above hand zone along the lateral axis for different values of $q_{\text{thermopile},c}$ and $q_{\text{thermopile},h}$, are represented in Fig. 10. In conformity with these dependences, the presence on the opposite lateral surfaces of unlike heat fluxes changes considerably the thermal field of the object with respect to the case when heat flux of the same sign is distributed along the lateral surface. The temperature value decreases from the lateral surface corresponding to heat flux $q_{\text{thermopile},h}$ to the surface affected by heat flux $q_{\text{thermopile},c}$. In so doing, a change in $q_{\text{thermopile},c}$ from the value of 3500 W/m^2 to 2500 W/m^2 at a constant value of $q_{\text{thermopile},h} = 1000 \text{ W/m}^2$ increases the temperature along the lateral axis by about 4 K. Thus, when performing contrast thermal procedures, under conditions corresponding to these dependences, to achieve the required temperature of skin surface which is a direct object of physiotherapeutic effect, one should take into account the mutual influence of $q_{\text{thermopile},h}$ and $q_{\text{thermopile},c}$ values. Selection of $q_{\text{thermopile},h}$

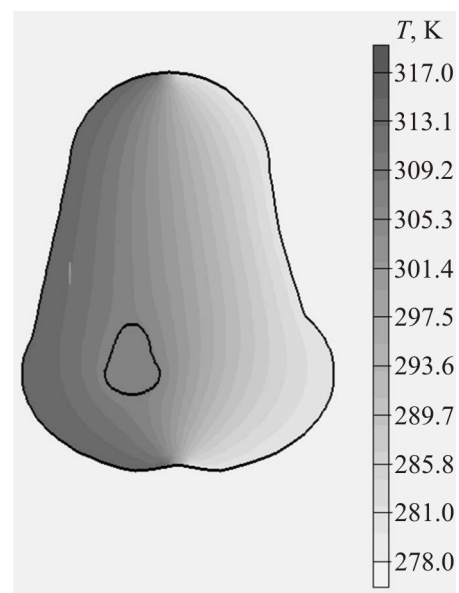


Fig. 9. Two-dimensional temperature field on the section of the middle third of the arm in the steady-state mode under contrast thermal effect for $q_{\text{thermopile},c} = 3000 \text{ W/m}^2$, $q_{\text{thermopile},h} = 1000 \text{ W/m}^2$.

and $q_{thermopile,c}$ values with the respective analysis of the temperature field of the object according to the model proposed will make it possible to optimize the energy characteristics of TES under study.

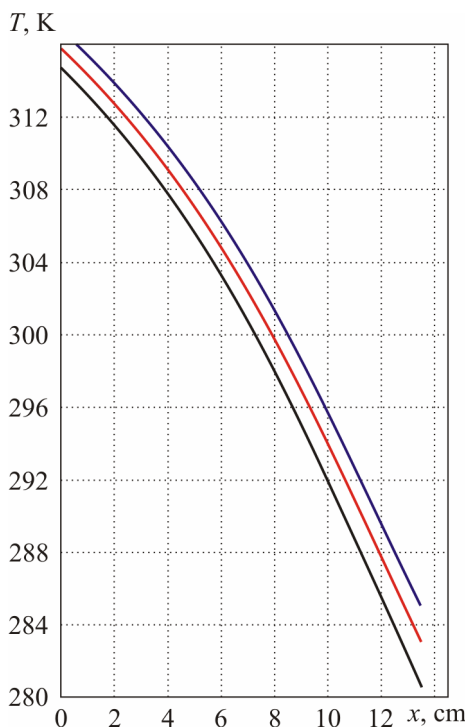


Fig. 10. Temperature distributions along the lateral axis of the middle third of the arm under contrast thermal effect for different values of $q_{thermopile}$. 1 – $q_{thermopile,c} = 3500 \text{ W/m}^2$, $q_{thermopile,h} = 1000 \text{ W/m}^2$; 2 – $q_{thermopile,c} = 3000 \text{ W/m}^2$, $q_{thermopile,h} = 1000 \text{ W/m}^2$; 3 – $q_{thermopile,c} = 2500 \text{ W/m}^2$, $q_{thermopile,h} = 1000 \text{ W/m}^2$.

For the analysis of the dynamic characteristics of TES a change in temperature at different points of a biological object under cooling and heating effect of TES was investigated. Fig. 11 represents temperature variation in time at different points of the middle third of the arm on cooling, and Fig. 12 – on heating for $q_{thermopile,c} = -2500 \text{ W/m}^2$ and $q_{thermopile,h} = 800 \text{ W/m}^2$, respectively. A variation in time of skin cover, muscular and bone tissue of biological object has been studied. According to calculated results, the time required to bring TES to the steady-state operating mode lies within relatively narrow limits. For the case corresponding to Figs. 11 – 12, the time required for stabilization of biological object temperature is about 1200 s (20 min.). The above factor should be taken into account when performing physiotherapeutic procedures. It is worthwhile to switch the device on prior to thermal exposure with a view to bring it to operating mode.

It is interesting to study the operation of TES in the mode of contrast thermal effect related to alternative cooling and heating of a biological object. Fig. 13 shows temperature variation on the skin cover of the middle third of the arm in time for such procedure mode. One cycle of contrast effect has been considered, namely object temperature reduction and then its rise and vice versa. Depending on the method of performing physiotherapeutic procedures, the cycle can be repeated several times. In conformity with the data obtained, through use of TES the treatment procedure of contrast thermal effect can be implemented to the full extent. The duration of change from one mode of exposure to another is relatively short. On the dependences shown in Fig. 13 it is of the order of 8 to 9 minutes. It should be noted that to accelerate a change in the modes of exposure, one can use short-time forced operation mode of TES, i.e. increase in thermopile supply current and, accordingly, the value of $q_{thermopile}$ in transient operating mode of device.

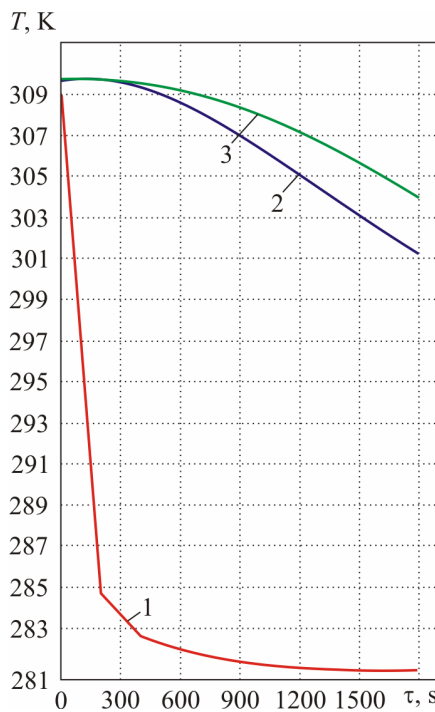


Fig. 11. Temperature variation at different points on the section of the middle third of the arm in time on cooling for $q_{\text{thermopile},c} = 2500 \text{ W/m}^2$. 1 – skin cover, 2 – bone tissue, 3 – muscular tissue.

Based on the analysis of the obtained values of heat flux on the lateral surface of biological object, equivalent to cooling power and calorific power of thermopile, the latter is subject to calculation. The sought-for values in this case are the geometrical dimensions of thermoelements (TE) forming part of thermopile, the value of supply electrical current, electrical energy consumption. In the majority of cases, as a thermopile in thermoelectric system (TES) one can use thermoelectric modules (TEM) of standard type that can be selected with the use of special applied software packages.

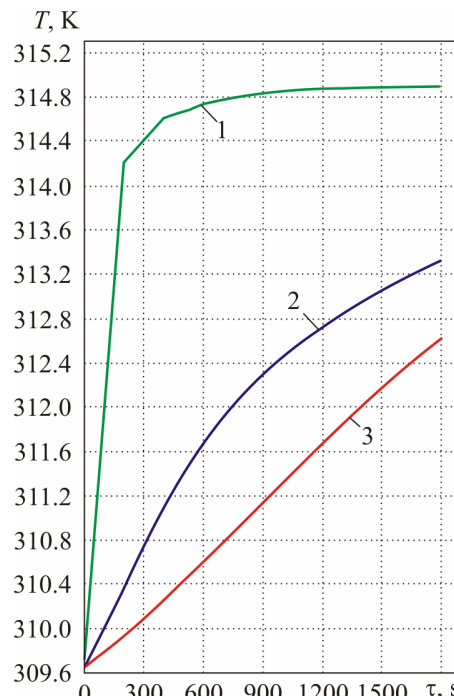


Fig. 12. Temperature variation at different points on the section of the middle third of the arm on heating for $q_{\text{thermopile},h} = 800 \text{ W/m}^2$. 1 – skin cover, 2 – bone tissue, 3 – muscular tissue.

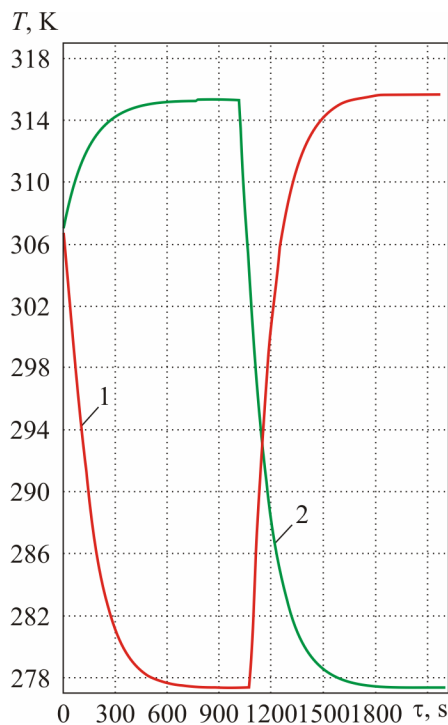


Fig. 13. Time variation of biological object under contrast procedures for $q_{thermopile,c} = 4000 \text{ W/m}^2$, $q_{thermopile,h} = 1200 \text{ W/m}^2$. 1 – cooling-heating, 2 – heating-cooling.

For TES variant under study one can use four standard TEMs of the type TB-127-1.0-1.5 produced by Engineering and Production Firm Kryotherm (Saint-Petersburg), realizing in full measure the required conditions of therapeutic procedures. For their selection a package of software programs “Thermoelectric system calculation” was used [7]. The specifications of this type of TEM are given ibidem.

Conclusions

1. Local thermal effect is widely used in medical practice in the therapy and prophylaxis of various diseases.
2. The above treatment method can be realized through use of TES distinguished by environmental safety, high reliability, efficiency and small overall dimensions.
3. The thermoelectric device studied in the paper is designed as a construction comprising a flexible elastic base with embedded thermoelectric modules that have flexible metal heat leveling plates on their junctions.
4. A thermal model of TES for performing thermal physiotherapeutical procedures on the middle third of the arm is a three-layered structure (skin cover, muscular and bone tissue) of complicated configuration. A thermal flux from thermopiles forming part of the system is directed to the external surface of the skin cover.
5. A mathematical model of TES is system of differential equations in partial derivatives with the boundary conditions of the second, third and fourth kind that has been solved with the aid of a numerical finite-element method.
6. In the numerical experiment, two-dimensional and one-dimensional plots of temperature variation at different points of device-object system have been obtained with different thermopile powers, as well as device operation conditions.
7. It has been established that with increase in thermopile power when operated in cooling mode, the

temperature of a biological object is reduced, and in heating mode – increased. In so doing, in the investigated range of thermopile powers the temperature of skin cover varies most strongly, whereas the temperature of muscular tissue in the centre of a biological object varies only slightly.

8. According to the plots, the temperature distribution in the target object is in a certain manner affected by the presence of bone tissue in its volume. Under the accepted conditions, such temperature variation is about 1 to 2 K as compared to the case when given object is absent throughout the tissue.
9. The presence on different areas of the lateral surface of unlike thermal fluxes changes considerably the thermal field of the object as compared to the case when a thermal flux of the same sign is distributed along the lateral surface. In so doing, there is practically monotonous temperature increase from cooling to heating zone.
10. The plots of temperature variation of different points of human hand with time have been obtained with a local thermal effect through use of TES. In accordance with the data obtained, the time necessary for temperature stabilization on cooling and heating of a biological object is about 20 minutes, and the duration of transient mode with contrast procedures is 8 to 9 minutes.
11. To realize the required conditions of performing thermal procedures, it is sufficient to use standard TEM commercially produced by manufacturing companies.

References

1. A.N. Kolushkin, *Curative Cold of Water* (Moscow: Fizkultura i Sport, 1996), 137 p.
2. G.L. Magazanik, *Thermal Therapeutic Agents* (Leningrad: Medgiz, 1961), 223 p
3. L.A. Komarova, L.A. Blagovidova, *Manual for Physical Methods of Treatment* (Leningrad: Meditsina, 1983), 264 p.
4. V.V. Kenz, A.I. Sukhenko, and T.M. Duca, Local Cold Effects in Physiotherapy, *Voprosy Kurortologii (Balneotherapy Issues)* 2, 83 – 87 (1983).
5. T.A. Ismailov, O.V. Yevdulov, G.I. Aminov, and M.A. Khazamova, *Patent of the Russian Federation for invention №2299711*, Thermoelectric Semiconductor Device for Local Temperature Effect on Human Hand. Publ. 27.11.2007, Bul. № 15.
6. A.V. Rumyantsev, *Finite-Element Method in Thermal Conductivity Problems* (Kalininograd: Kaliningrad State University, 1995).
7. <http://www.kryotherm.ru>.

Submitted 29.10.2013.

NEWS



INTERNATIONAL THERMOELECTRIC ACADEMY

Oleksandr Petrovych Huk

(DEDICATED TO 60th BIRTHDAY)

March 3 this year is the 60-th birthday of Oleksandr Petrovych Huk, PhD in Engineering, corresponding member of the International Thermoelectric Academy, a well-known specialist in the area of basic research on electric temperature measurement, Director General of Closed Joint-Stock Company "V. Lakh Scientific-Production Association "Thermoprylad"" (Lviv, Ukraine).

O.P. Huk's scientific research activity is inseparably related to his successful production activities. He is at the head of "Closed Joint-Stock Company "V. Lakh Scientific-Production Association "Thermoprylad" which is a leading organization in the field of electric temperature measurement. Instruments created at the Scientific-Production Association "Thermoprylad" assure temperature control for complex technological processes in various fields of industry and scientific research. These are atomic and thermal power plants, metallurgical and cement works, chemical and food industry objects, spacecrafts, surface ships and submarines, crystal growing plants, etc. According to different estimates, temperature measurements make nearly 30 % of all the measurements in modern industry and science.

At the Scientific-Production Association "Thermoprylad" more than 1000 types of temperature control instruments have been developed and commercialized practically for all areas of national economy and scientific research in the temperature range of -270 °C to +4000 °C. Specialists of the Association have received more than 500 inventor's certificates.

O.P. Huk is the author of over 60 published works, in particular, the books "Scientific-Production Association "Thermoprylad": History, Activity, Staff" (2006) and "Temperature Measurement: Theory and Practice" (2006).

O.P. Huk's personal contribution has been honoured with numerous commendations from the Ministry of Industrial Policy of Ukraine, Certificates of Merit from Lviv Regional State Administration and Diplomas of the International Thermoelectric Academy (2000, 2004).

International Thermoelectric Academy, Institute of Thermoelectricity of the NAS and MES of Ukraine, "Journal of Thermoelectricity" Publishers sincerely congratulate the esteemed Oleksandr Petrovych Huk on his 60-th jubilee, wishing him sound health, inexhaustible energy, happiness and success in his multifarious activities.

M.A. Korzhuev¹, V.V. Temyakov²

M.A. Korzhuev

¹A.A. Baikov Institute of Metallurgy and Material Science of RAS, 49, Leninsky Ave., Moscow, 119991, Russia;
²Open Joint Stock Company “The Great Russian Encyclopedia”, 8, Pokrovsky Boulevard, Moscow, 109817, Russia



V.V. Temyakov

**RICHMANN'S AND LOMONOSOV'S
RESEARCH IN THE FIELD
OF THERMOELECTRICITY (1745 – 1753)**

The works of G.-W. Richmann and M.V. Lomonosov, academicians of Saint-Petersburg Academy of Sciences (1745 – 1753) on studying “heat ↔ electricity” cross effects in the gaseous, liquid and solid dielectrics are considered. These effects are compared to thermoelectric (TE) effects observed in other thermoelectrically-active media. It is shown that TE effects in dielectrics feature large operating voltages (U up to 10^3 – 10^5 V or more) and small discharge currents ($I \sim 1$ – $10 \mu\text{A}$) due to high intrinsic resistivity ρ of the samples. The paper is dedicated to the thousandth anniversary of cultural interaction between Russia and Germany commemorated in 2012.

Key words: thermoelectrets, atmospheric electricity, thermoelectricity.

Introduction

The sequence of discovery of the basic TE effects in various thermoelectrically-active media has been studied previously [1-3]. According to [3], the first TE effects were found in dielectrics where they are of the highest value (the measured voltage U is up to 10^2 – 10^3 V or more).¹ It was not until later, with increasing instrument sensitivity, that TE effects were also found in metals (1821) where their value is essentially limited by the strong Fermi degeneration of samples ($U \sim 10^{-3}$ V) (T.I. Seebeck (1770 – 1831)). The present paper contributes to further research [3]. The paper discusses the experiments of academicians G.-W. Richmann (1711 – 1753) (Fig. 1)² and M.V. Lomonosov (1711 – 1765) (Fig. 2) in thermoelectricity carried out in St. Petersburg Academy of Sciences in 1745 – 1753 [4-5]. The Academy (founded in 1724) was specialized in natural science research, both academicians working at the junction of the theories of electricity and heat. As a result, Richmann was the first to discover and study a series of TE effects in dielectrics (charge transfer by flame, TE effects in sulfur and resins, etc.) [4]. Together with Lomonosov he was the first to discover and study complex atmospheric TE effects responsible for the electrization of clouds [4, 5]. It is shown that one of these atmospheric TE effects could have caused the tragic death of Richmann (1753).

¹ Some of these effects have been known since ancient times [3].

² Richmann and Seebeck were born in the Russian Empire, in the families of Baltic Germans - Lutherans. Both were at various times trained in the former Swedish Gustav II Adolf's grammar school in Reval (now Tallinn, Estonia) of what the local regional specialists E. Velmre and E. Keerov have kindly informed us.

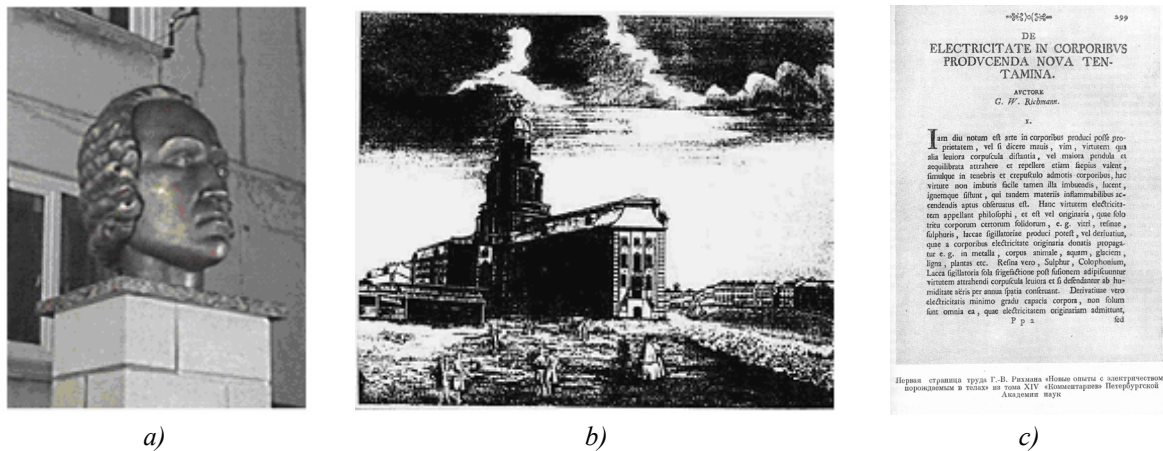


Fig. 1. A monument to Richmann in his homeland in Pärnu (Estonia) (sculptor E. Kuulbush, 2011) (a), the Kunstkamera Museum in SPb, (engraving 1730 – 1740) (b), and the priority paper on the thermoelectrets discovered by Richmann ("Comments of the Petersburg Academy of Sciences", V. 4, 1751) (c) [4].

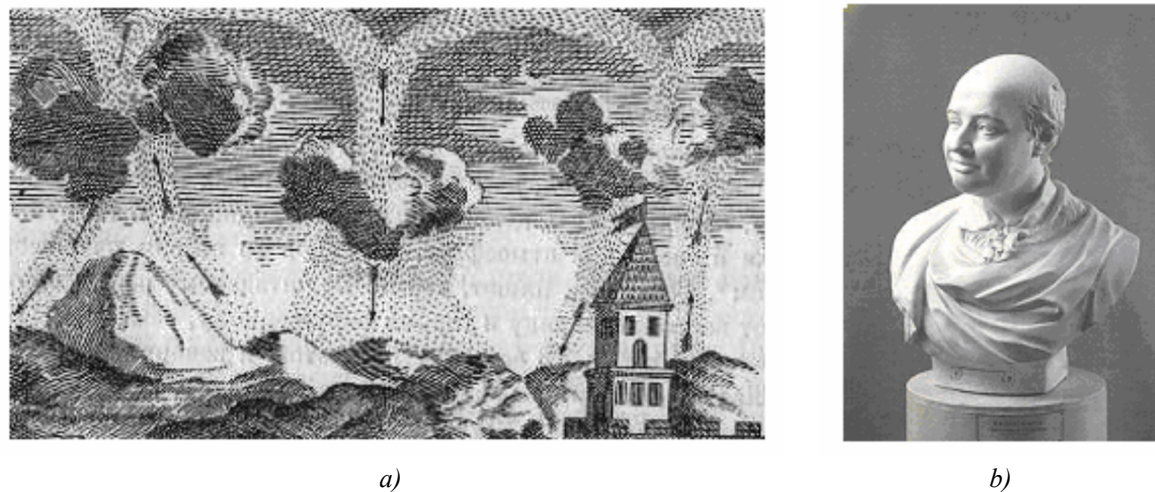


Fig. 2. Complex atmospheric TE effect explaining electrification of clouds by friction of the ascending and descending air flows (1753) (a) [5]. A bust of M.V. Lomonosov (Sculptor F.I. Shubin, 1792). Lomonosov Museum, the Kunstkamera Museum, SPb (b).

1. Richmann's works on thermoelectricity

Academician Richmann went down in the history of physics as the inventor of the “electric pointer” (electrometer), the first device suitable for quantitative measurements of electric voltage U (Fig. 3 a) [6]. The operation of Richmann’s “pointer” is based on the laws of electrostatics. When connected to a source of electricity by wire (a), the movable thread (e) and the stationary lineal (c) obtained electric charges of the same sign. As a result, the thread deviated from the lineal by the corner α which determines the measure of the electrical force ($U \sim \alpha$, for small angles α) (Fig. 3 a).

In 1745, Richmann was appointed head of the Physical Cabinet of St. Petersburg Academy of Sciences located in the Kunstkamera Museum up to the 1747 fire (Fig. 1 b). It was there that Richmann began the first studies of “heat-electricity” cross effects in various thermoelectrically-active media [3, 4]. At an early stage of his research, Richmann “... carrying out his own and repeating somebody else's experiments on electricity ... came across many new phenomena that he had not found in the works of his predecessors” ([4], p. 207).

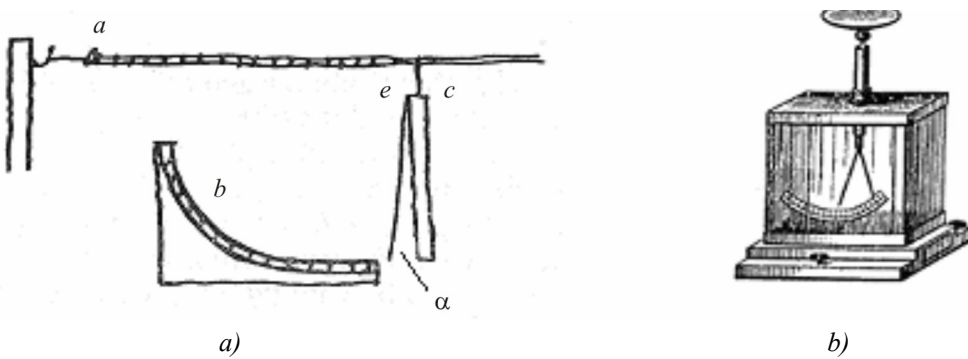


Fig. 3. Richmann's "Electric pointer" (1745) (c – "lineal" (Fe), a – lead wire (Fe), e – linen thread (weight – $\frac{1}{2}$ apothecary grain (0.312 g), length – 1 $\frac{1}{2}$ London ft (0.4572 m), b – wooden quadrant with a scale [4] (a) and the Cavallo electrometer (1799) with a protective case (b) [6].

The first success in Richmann's investigation of TE effects was achieved when studying the effect of electric charge transfer by flame. This effect had been described by Gilbert as applied to the case of charge transfer from dielectric to dielectric [7]. Richmann managed by the same method to transfer electrical charge from dielectrics (in his terminology – "electricitas originaria" – "primary electrical bodies" ("PEB") to metals ("electricitas derivative" – "secondary electrical bodies" ("SEB") (conductors)) [4]. Richmann wrote: "*June 30th (1746). Using a lit candle, I rejected electricity ... <from the electrophoresis> to the table, from the table to the chandelier, from the chandelier to the flame, from the flame to iron plate ...*" [4]. Richmann then investigated the effect using his "pointer": "... I brought wax candle flame to the CB iron wire (connected to the source of the charge) ... and the pointer began to show a smaller degree α " (Fig. 4 a) ([4], p. 268). Comparing the effect of the extinguished and burning candle on the pointer readings, Richmann found that it was not the candle itself that rejected electricity, but its flame ([4], p. 212). In this case, the transfer of electricity was also observed when a burning candle was sufficiently removed from the wire. Richmann found that the products of candle combustion also transferred the electrical charge: "... an electrified body ... attracted some of the smoke from the extinguished candle, and the other part of smoke ascended as usual" ([4], p. 222).³

At the same time, a blast of water steam produced by the aeolipile (steam turbine) invented by Heron of Alexandria and directed at "electric pointer" practically did not change its readings (Fig. 4 b). Hence Richmann concluded that "... for the rejection of electricity one needs a solid PEB. But water vapors are corpuscles separated by certain gaps and unable of forming a solid PEB and they can neither take nor reject any appreciable amount of electricity." ([4], p. 312).

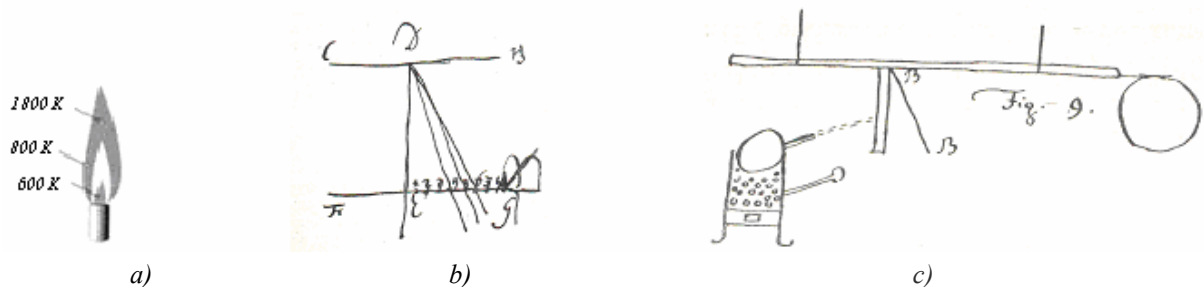


Fig. 4. Schematics of Richmann's experiments (original figures) with candle flame (a), electric indicator (b) and the aeolipile (steam turbine) of Heron of Alexandria (c) [4].

³ The conductive properties of flame and the charge of smoke particles are determined by ions and radicals formed in combustion process and forming a conductive halo around the flame [8].

Richmann also made a number of important discoveries in triboelectricity. As is known, charge transfer at mutual friction of different materials promotes local temperature increase in the microregions of frictional contact (ΔT_{local} to 10^3 K or more) [8]. Richmann found that the initial temperature T_0 of the samples also affects the processes of electrization by friction. He showed that dielectrics having a lower triboelectricity compared to amber (agate, jasper, porphyrites, granite, marble, etc.) can also be successfully electrified by friction. For this purpose, they "... should be hot and rubbed for long time."⁴ Richmann also recommended heating "... to the point of ignition" the relevant counter-bodies (bristle, leather, parchment, paper, silk, linen, etc.). Finally, for the first time Richmann managed electrifying metal by friction using intermediary material. He inserted iron bars into thin glass jars and "... excited electricity by gently stroking, whereby these rods emitted a spark when touching them" ([4], p. 285).⁵

However, the most important result in thermoelectricity was obtained by Richmann studying thermoelectret effect in sulfur and resins (1746) [2].⁶ Richmann wrote: "*June 25, 1746. I melted the bodies which, when cooled and solidified, being protected from air moisture have long lasting (for instance, for a year) electricity (common sulfur, wax, resin or rosin) ...*" ([4], p. 244). With his "pointer" Richmann found that sulfur and resins can be electrified both by friction and by "melting-solidification" [4]. Richmann published the results of his experiments in the priority article: "Recent experiments with electricity generated in the bodies" ("Comments of the Petersburg Academy of Sciences", v. 4, 1751) (Fig. 1 c) [4].⁷ Table 1 shows the main types of electrets currently known and the thermoelectrets discovered by Richmann [9]. From Table 1 it is clear that Richmann is the pioneer of the monopoly (plus sign) thermoelectric effect observed in a number of dielectrics at "melting-solidification" phase transition (Table 1).⁸ Charging samples with "electricity", Richmann then investigated the possibilities of maintaining the resulting electrical charges under various conditions. He studied in detail the acceleration of charge leakage processes from the sharp parts of samples, wetted by water and depending on room humidity ([4], p. 645 and 237). According to Richmann (1748), "... *in a wooden house electricity often persisted for 50 minutes before disappearing, whereas in stone <rooms> ... it could not persist for more than 10 minutes. Possibly, moisture contained in a stone house rejects electricity*" ([4]).

According to modern concepts, the process of relaxation of the electric potential of charged bodies depending on the time t follows an exponential law

$$U(t) = U_0 \exp(-t / \tau), \quad (1)$$

where U_0 is the initial value of the potential, $\tau = \min(\tau_M, \tau_M^0)$, τ_M , $\tau_M^0 = \epsilon_r \cdot \epsilon_0 \rho$ is 'Maxwell relaxation time for the test material and the environment, $\epsilon_0 = 8.85 \cdot 10^{-12}$ F/m and ϵ_r are the dielectric constant and the relative dielectric constant (static), ρ is the resistivity of the material or medium [8, 12]. Table 2 shows a comparison of the values τ_M and τ_M^0 , calculated for different materials and media according to present data [12] and according to Richmann's data (marked with *) [4].

⁴ The effects are related to decreasing the output energy of electrons from materials with a rise in temperature [8].

⁵ Since the time of Gilbert, the majority of physicists had shared the opinion that metals cannot be electrified by friction [7]. The Richmann's effect is obviously related to glass electrification with subsequent charge transfer to metal.

⁶ Currently one refers to electrets the dielectrics with resistivity $\rho > 10^{12} - 10^{17}$ Ω·m, which are able of accumulating and storing the nonequilibrium electric charges for 1 to 10 years or more [9].

⁷ Sometimes the discovery of thermoelectrets is attributed to Epinus or Wilke (1765) [10] who found different signs of the charges received by the sulfur (-) and the casting mold (+) which in due time had been overlooked by Richmann [11].

⁸ The effect is associated with the formation in sulfur band gap ($E_g = 2.6$ eV) of the deep donor levels [9].

From Table 2 it is clear that Richmann correctly identified the characteristic times of the charge leakage from the samples at varying humidity in the room. In particular, from Table 2 it follows that the charge on thermoelectrets (sulfur, wax, etc.) in a dry place really could persist for up to a year or more [4].

Table 1

*The main types of electrets depending on the production method**

Nº	Name	Method of charging	Charge	Examples	Discoverers
1	Triboelectrets	Friction on counterbody	Monopole	Amber ⁻ /yarn ⁺ Glass ⁺ /silk ⁻ Resin ⁻ /wool ⁺ Sulfur ⁻ /cloth ⁺	Thales of Miletus (625 –545 B.C.) Dufay (1733) -<- Aepinus, 1765
2	Thermoelectrets	Melting-solidification	Monopole	Sulfur ⁺ /cup ⁻	Richmann, 1746 Aepinus, Wilke, 1765
3	Electro-thermo-electrets	Similarly, but in electric fields	Dipole	Wax	Eguchi, 1919
4	Ferro-electrets	Cooling below T_c (Curie temperature), electric field	Dipole	Segnett's salt, KDP (kaliumdihydrogenphosphate), TGS (triglycinesulphate)	P. and J. Curie, 1880, F. Pockels, 1894

* There are also corona-, photo-, radio-, chemo-, mechano-, bio-and other electrets whose electrization is not connected directly to the thermal effects on the samples [9].

From Table 2 it also follows that candle flame reduces air resistivity ρ by 3 – 4 orders, although the value of ρ in the flame zone still retains a significant amount corresponding to "bad" dielectrics (wood). From Table 1 it is also evident that the triboelectric effect in metals under normal conditions is not observed because of the small τ_M . However, this does not preclude impact electrization of metals [8]⁹.

Table 2

Maxwell relaxation times τ_M of charges for different materials and media [4, 12]

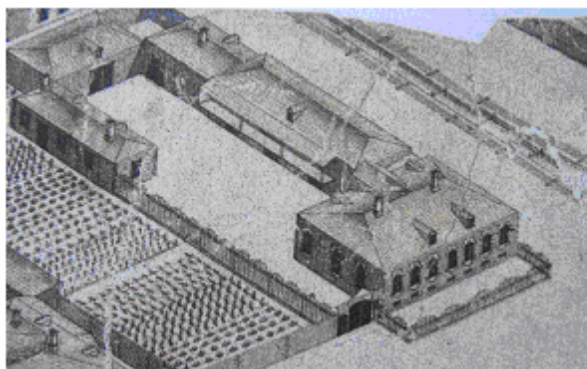
Media	ϵ_r	$\rho, \Omega \cdot m$	τ_M^0, c	Material	ϵ_r	$\rho, \Omega \cdot m$	τ_M, c
Dry air	1	$> 10^{15}$	$> 10^4$ $\sim 3.10^3$ *)	Sulfur	3.7	10^{17}	$\sim 10^6$ $\sim 10^{8*})$
Natural ionization air**	1	10^{14}	10^3 $\sim 6.10^2$ *)	Sealing wax	~3	10^{16}	10^5
			Oils		$10^{11} - 10^{14}$	$1 - 10^3$	
Humid air (100%)	1	$< 10^{13}$	$< 10^2$	Paraffin	2.2	$10^{14} - 10^{16}$	$10^3 - 10^5$
Candle flame	~1	$\sim 10^{11}$	~1	Amber	2.9	10^{18}	10^7
Rain water	31	10^4	10^{-6}	Paper	2-4	10^{15}	$\sim 10^4$
Sea water	31	0.3	$\sim 10^{-11}$	Iron	~1***	10^{-7}	$\sim 10^{-18}$
Wet soil	~10	10^2	$\sim 10^{-8}$	Wood	3.5 – 5	$10^9 - 10^{13}$	$10^{-2} - 10^2$

*) – Richmann's data ** – at the Earth's surface; *** – the contribution of the crystal lattice.

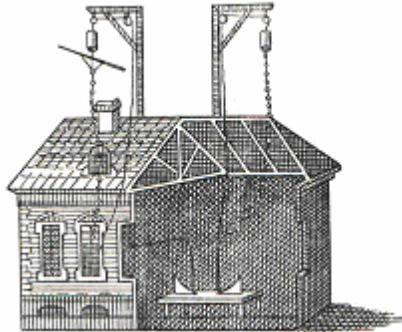
⁹The method was proposed by Lomonosov (1753) ([5], p. 278), and then successfully implemented for metals by acad. V.V. Petrov (1761 – 1834) in his work "The new electrical experiments" (1804) [5, 6, 8].

2. Atmospheric thermoelectric effects

In 1752, the “St. Petersburg News” published the first message on the B. Franklin’s experiments proving the electrical nature of lightning [13]. Richmann immediately embarked on a study of atmospheric electricity, having adapted for measurement his “electrical pointer” (Fig. 3 a). A little bit later academicians M.V. Lomonosov (theoretical issues) and K.G. Kratzenstein (1723 – 1795) (creation of lightning arresters) also joined in the research on atmospheric electricity [4, 14]¹⁰. By that time Lomonosov had already considerable scientific developments on the matter under investigation [5, 15, 16]. In 1744 – 1748 he held systematic observations of thunderstorms at his home in St. Petersburg and established their TE nature (Fig. 2 a) [5, 16]. Lomonosov found that “... the storm clouds mostly in the afternoon occur ... when the actions of the sun to heat the air all the more sensitive” ([5], p. 236), p. 226).¹¹ The mechanism of cloud electrization was attributed by Lomonosov to mutual friction of ascending and descending air flows at convection resulting from the non-uniform heating of the Earth's surface by solar rays (Fig. 2 a). The widely known characteristic of atmospheric electricity by Lomonosov is “... *Electric force produced by natural heat ...*” ([5], p. 226). As the other thermal sources of atmospheric electrization, Lomonosov also considered the Earth's interior heat, fires and even smoking [5]. Richmann and Lomonosov started their experimental study of atmospheric electricity with construction of “thunder machines” – installations for the production of electricity from storm clouds by Franklin’s method (Figs. 5 and 6) [13]. Since the late 1752 Richmann had in his town house (Fig. 5 a) two “thunder machines” with “sharp” and “blunt” rod ends (Fig. 5 b) which were used for comparative measurements ([4], p. 653). In 1753 Lomonosov placed one of the installations in his town mansion (Fig. 6 and 6 b), the other – in “the village” (Estate Ust-Ruditsa) (Fig. 6 c), where he built his factory of art mosaics ([5], p. 260).



a)



b)

Fig. 5. Richmann's mansion with a one-story brick house “on the basement” on the corner of Great Prospects and Line 5 in SPb (right side) (a) [18] and his “thunder machine” (end of 1752) (b) ([4], p. 653) [28].

All installations were similar and consisted of isolated vertical or inclined iron rods placed on the roofs of the houses (Fig. 5 b and 6 b) or on the trees (Fig. 6 c). The rods acted as aerials that were connected with iron wires (or chains with Richmann) to “electrical pointers” (Fig. 3 a). Electrical wire insulation was carried out with a silk cloth. Richmann placed his pointers inside the house (Fig. 5), Lomonosov

¹⁰ Acad. K.G. Kratzenstein (1723 – 1795), physician, physicist and engineer. After Richmann’s death (1753) he was dismissed from the Academy at the end of the contract period (1748 – 1753). He went to Copenhagen to study the theory of gases and the application of electricity in medicine [4, 6].

¹¹ According to present data, the electrical activity of the Earth's atmosphere is also significantly affected by cosmic rays [12, 17].

conducted observations outdoors (points *c*, Fig. 6 *b* and 6 *c*) (Fig. 1).¹² To improve inleak of charges from the atmosphere, Lomonosov's installations had “many metal needles” at the ends of the rods (Fig. 6 *b* and 6 *c*) [5], p. 265.

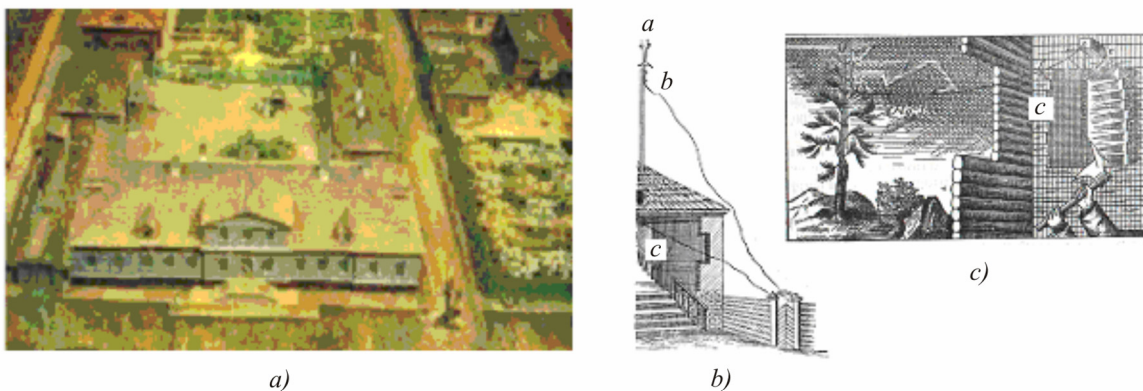


Fig. 6. “Bonn house” mansion in the second line of Vasilevsky Island in SPb where Lomonosov resided (1741 – 1757) (third building on the left in the background is Lomonosov's chemical laboratory), (a) [15] and his "thunder machines" (May 1753) (b), and (June 1753) (c) (a – aerial; b – lead wire, c – the place of observation) [5, 16].

The experimental works of Richmann and Lomonosov with the “thunder machines” proved to be extremely fruitful. Richmann identified the range of variation of pointer readings α and found that in the area of St. Petersburg “the highest degree α to which the thread is raised by the action of natural electricity was the 30th” ([4], p. 358). He found that for the clouds offset from the observer by the distance of $L > 3$ km, the value of α (that is the normal component of electric field E) at observation point decreases with increasing time interval between lightning and thunder $L \sim \Delta t$ ([4], p. 358) (curve 1, Fig. 7).¹³ In turn, Lomonosov found that the primary cause of atmospheric electricity are not thunder and lightning proper, but the electrical charges of the clouds [4] (p. 269). He also found small deviations in α readings of “electric pointer” and for a cloudless sky.¹⁴ On this occasion Richmann wrote: “*The renowned man Lomonosov observed that even in the absence of thunder and lightning, significant electricity is transferred to iron properly insulated. As for me, I observed that electricity after lightning and thunder was immediately reduced*” ([4], p. 358).¹⁵

Using as a prototype the earlier work of I.G. Winkler (1746), Richmann concluded that the physical mechanism of cloud electrification consists in the friction of PEB (solid particles¹⁶ or water vapors) with SEB (water droplets) ([4], p. 640). Lomonosov did not find in the air any sufficient number of solid particles, and as a PEB he considered hypothetical ether oils evaporated by animals and plants. Then, making sure there are none, as a possible mechanism of cloud electrification Lomonosov proposed “*fight (impact) of electric vapors and their friction at counter motion in the atmosphere*” [5]. The latter mechanism with variations has been used to this date to account for cloud electrification [17].

¹² The two houses of Lomonosov were wooden and had increased fire hazard ([5], p. 260).

¹³ Recalculation of $\Delta t \leftrightarrow L$ and $\alpha \leftrightarrow E$ was made by us for relationships $\alpha \sim E^{0.5}$ and $\alpha = 30^0 \sim /E/ = 25$ kV/m.

¹⁴ According to our estimates (Fig. 7), the sensitivity of Lomonosov's installation was sufficient ($\Delta\alpha \sim 0.5^0$) to observe Earth's natural field $E_0 \sim 0.14$ kV / m (↓)) in good weather [12].

¹⁵ The effect is due to the annihilation of positive and negative charges in the cloud discharges [17].

¹⁶ As it was established later, Richmann's mechanism explains electrification of atmosphere in the zone of industrial emissions containing solid particles [17].

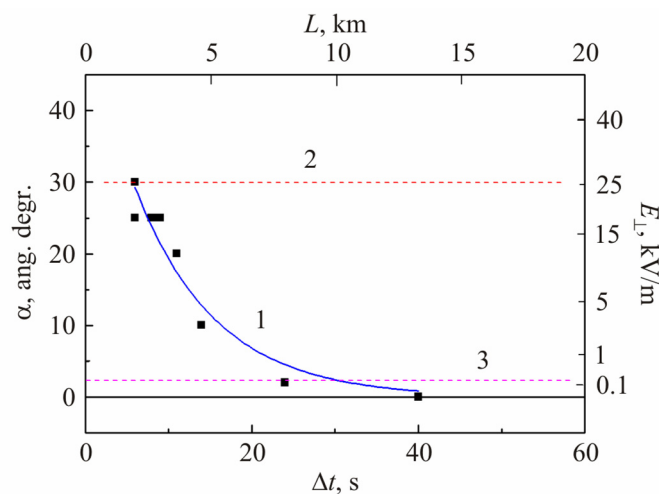


Fig. 7. The α readings of Richmann's "pointer" and the corresponding changes in the electric field E (\downarrow or \uparrow) versus the delay of "lightning-thunder" signals Δt and the distance L to the storm front (recalculation is ours). 2 – α_{\max} ([4], p. 358), 3 – $E_{\perp}^0 \sim 0.14$ kV/m (\downarrow) is Earth's natural field in the cloudless sky.

On July 26, 1753, Lomonosov and Richmann for the last time attended together the meeting of Saint-Petersburg Academy addressing an issue of their reports on atmospheric electricity that were appointed on September 5, 1753. About 12:00 p.m. noon, when a big storm cloud appeared over Petersburg, they left the meeting and both went to their homes for making observations. Richmann took with him the academic engraver I.A. Sokolov to create drawings for "Petersburg News" newspaper. On entering the house and getting closer to his installation at a distance of about a foot (about 30 cm), while the sky was still cloudless, Richmann was struck by a discharge of atmospheric electricity (Fig. 8 b). A white and blue ball the size of a fist that separated from the electrometer lineal touched the scientist's head and then exploded. Sokolov, who was standing a little aside, got a few sparks from the falling wire, flung out of the room and called the fire brigade. Richmann's wife, Anna Elizabeth Hinze, tried to give her husband mouth to mouth. Reanimation attempts were continued by Kratzenstein who urgently came to the place of accident, but he failed to reanimate the academician. Lomonosov who also arrived at Richmann's house, wrote to Count Shuvalov, favorite of Empress Elizabeth: "... the thunder killed Professor Richmann in exactly the same circumstances I was at that time".

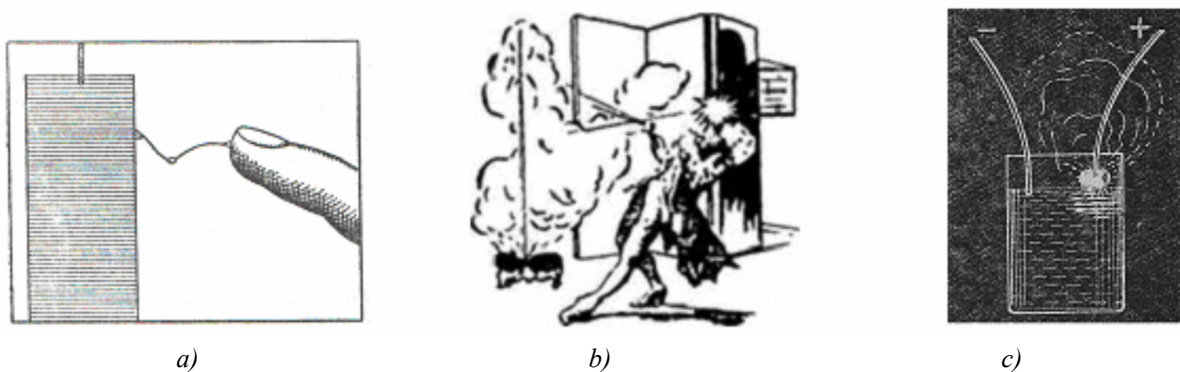


Fig. 8. Different types of electrical discharges: a – an individual spark observed by Lomonosov [5], b, c – positive plasma streamers (glowing ball discharges). b – Richmann's death as described by Sokolov [4], c – Plante experience with liquid electrolyte (1883) [8].

Richmann's unusual death caused a wide resonance in Russia and abroad. The incident was investigated by the academic committee (Ch.G. Kratzenstein, M. Schreiber, M. Kleinfeld) [4],¹⁷ Lomonosov pursued his own independent inquiry [4, 5]. Kratzenstein reported (Fig. 9) that a loop of electric shock ran from the left side of Richmann's forehead to his left heel (with separate outputs for left chest and under the ribs), which, according to contemporary statistics, is typical of head electrocutions [20]. Kratzenstein also established places of electrical breakdowns in the house (Fig. 9 b) and stated the main reason for the accident, namely the violation of safety rules (the installation was not grounded) (Fig. 5).¹⁸ According to Kratzenstein, lightning did not spread from the roof of the building, but "... a ray of lightning "entered" the door, which was carried by a gust of wind into the house, and then along the wire to Richmann, passing by Sokolov".¹⁹ Lomonosov did not support Kratzenstein's conclusions and wrote that "many a man said to have seen the lightning flash outside" ([5], p. 547).

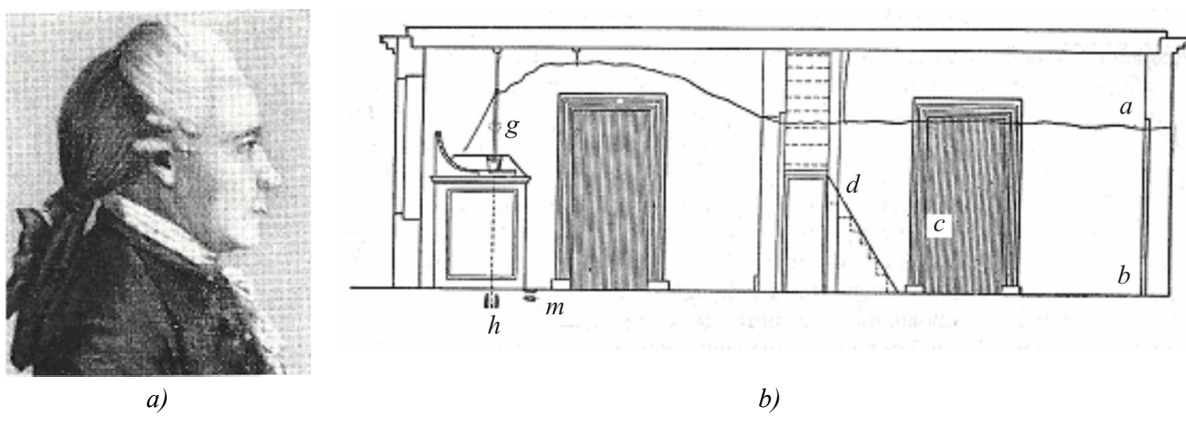


Fig. 9. Academician Ch.G. Kratzenstein (1723 – 1795) [14] (a) and places of electrical breakdown in the hall of Richmann's house (b) [4], p.653]. g, h – the breakdown of Richmann's body, m – Sokolov burns with sparks from the fallen wire, c – breakdown in the kitchen door jamb (d – bounced piece of wood), a, b – breakdown and falling of entrance door ([5], p.653).

Foreign scholars of the day came out with their own versions of the incident. Thus, I. Winkler (1753), W. Watson (1754) and I.-F. Hartman (1764) showed that Richman was killed not by lightning, but by electricity induced in the aerial by clouds. I.K. Wilke (1759) supposed that Richmann came up to the lineal at a dangerous distance, since he did not know that *some clouds may induce positive electricity in the aerial, the others – negative, and sometimes it changes instantly* ([4], p. 700). But all the details of the incident remain unclear up to now [4].

In this paper, we have undertaken further investigation of the incident using current data on the affecting factors of atmospheric electricity [12, 17]. Comparing the data by Kratzenstein [4], Lomonosov and Sokolov [5], we have determined the position of a storm front at the time of the incident (Fig. 10), assessed the readings of Lomonosov's and Richmann's electrometers, as well as restored the sequence of the observed electrical discharges and their nature (Fig. 11). According to Fig. 10, at the time of the incident the storm front was far from Richmann's house at a distance of 1 km. Therefore, we also believed that the scientist was struck not by a direct stroke of lightning into the

¹⁷ Special dossier «About the death of Prof. Richmann» № 433 ([4], p. 695) has remained.

¹⁸ Richman did not ground the lineal intentionally, as in that case the installation was transform into an arrester and its sensitivity would become equal to zero [4].

¹⁹ Kratzenstein's report gave rise to known hypothesis of Richmann's injury by a fireball that flew into the open door of the house.

"thunder machine", but by the discharge of electricity induced in the aerial by the charged cloud [4]. Based on the time coincidence of discharges (2 and 3, Fig. 11) [4, 5], we believed that the peripheral lightning near Lomonosov's house (3, Fig. 10) became a "trigger mechanism" for the discharge in Richmann's house (Fig. 8 c).



Fig. 10. Position of storm front (2) and direction of its motion at the discharge of periphery lightning (4) in the experiments of 26 July 1753.
 1 – Lomonosov's house, 3 – Richmann's house.

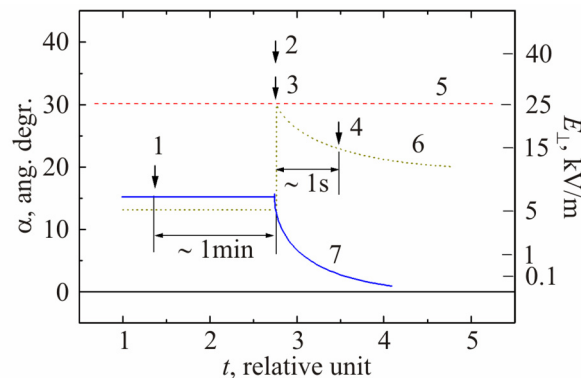


Fig. 11. The α readings of Lomonosov's (7) [5] and Richmann's (6) electrometers (our estimate) depending on time t in the experiments of July 26, 1753.
 Discharges: 1 – lineal-Lomonosov's hand,
 2 – peripheral lightning, 3 – lineal-Richmann's forehead,
 4 – wire-Sokolov. Type of discharge:
 1, 4 – plural spark (brush-type), 2 – lightning,
 3 – positive streamer.

In turn, the discharge was caused by the scientist's careless approach to the "pointer". According to Sokolov, Richmann approached the "pointer" because he wanted to clarify its contradictory reading, namely the cloud was near (Fig. 10), but low α showed that "thunder is still a long way" (see Fig. 7).²⁰ Our estimates of Richmann's electrometer readings (curve 6, Fig. 11) confirm this version of Sokolov.²¹ The supposed electrical circuit of Richmann's injury is shown in Fig. 12. The estimates of the circuit parameters (Fig. 12) prior to and at the moment of air breakdown of "lineal – Richmann's forehead" gap (R_2) are shown in Table 3. From the characteristic shape of the discharge (the ball) and the direction of its motion from the "lineal" to Richmann's forehead, we supposed that at the breakdown of R_2 there was positive plasma streamer formation (Fig. 8 b and 8 c) [8]. This assumption is confirmed by the discharge duration (several seconds) and characteristic "collapse" and explosion of the ball [4, 5]. Hence it follows that at the discharge the lower edge of the cloud closest to Richmann's house was charged positively (+) (Fig. 13). Moreover, the concentration of positive ions in the electrode gap R_2 exceeded the critical value $N_{\text{crit}}^+ \sim 10^{12} \text{ cm}^{-3}$ necessary for self-discharge of this type, and the energy of the breakdown was sufficiently large [8, p. 238]. We determined the magnitude of the voltage $U_2 \sim 25 \text{ kV}$ in the discharge gap R_2 (Fig. 12) from the tabulated data for the air breakdown of the "point-plane type" (edge of the lineal (+)-Richmann's forehead (-)) for the length of $L = 1$ foot (about 30 cm) (Table 3) [12]. Hence, when aerial height $h = 4 \text{ m}$ and cloud height $H \sim 1 \text{ km}$ we have $E_{\perp} \sim 25 \text{ kV/m}$ (↓) (Fig. 13), which yields $U_1 \sim 25 \text{ MV}$ at

²⁰ The majority of academicians of SPb AS suffered from short-sightedness, as they worked much by candlelight [4, 5].

²¹ Richmann ([4], p. 212) and Lomonosov [5] often used the "over head" discharge for research and medical purposes. Richmann suffering "strongest toothache" ([4], p. 92) could treat it by "electricity". However, this cause of the incident seems to us less likely.

the moment of discharge (Table 3) [12]. According to Sokolov, “... the thunder was still not very close but in the hall there was already smoke, at the same moment lightning flashed, the door to the kitchen was opened, and Professor fell down on the chest” (Fig. 4 b). From this we concluded that, even before the main electrical discharge, lethal for Richmann, there was a leakage of current from a supply wire to the ground²². The leakage took place through the damp wooden parts of the doors leading to the kitchen and to the street (*c* and *ab*, Fig. 9). The values of resistances $R_i = \rho l/s$ ($i = 1, 2 \dots 6$) (Table 3) (here ρ is ambient resistivity, l and s are characteristic lengths and the effective sections of conducting channels) were estimated by us according to Table 2, for damp wood and brick we assumed $\rho \sim 10^4 \Omega \cdot \text{m}$ [12]. In the calculations we used the values l (m) = 10^3 ; 0.3; 1; 2; 1 and s (m²) = 10^5 ; 0.01; 10; 10^{-2} ; 10 for $i = 1, 2, 4, 5, 6$ (Table 3), resistance $R_3 = 10^4 \Omega$ was taken from [20].

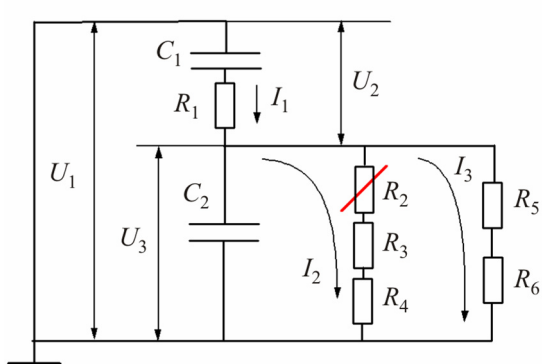


Fig. 12. Schematic of Richmann's injury with a discharge of atmospheric electricity (The notation – see Table 1).

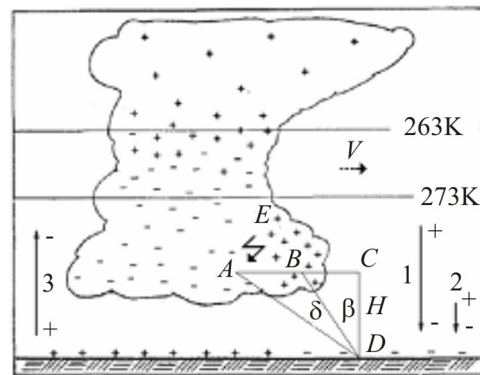


Fig. 13. Schematic of storm cloud and the mechanism of increasing the electric field E at the Earth surface (point D) with a peripheral electric discharge AE . Cloud areas: 1, 2 – “positive”, 3 – “negative”. E : 1 – after discharge, 2 – prior to discharge [17].

Under normal conditions, the indoor air comprises $N = 10^3 \text{ cm}^{-3}$ ions of opposite sign, the outdoor air before the storm – $N = 10^5 \text{ cm}^{-3}$, and electricity leak into the ground through the damp walls could have increased the concentration of ions in the air up to $N \leq 10^6 \text{ cm}^{-3}$. This is in conformity with plural spark (“brush-type”) injury of Sokolov [4], however it is obviously not enough to form a positive plasma streamer in the R_2 space (Fig. 11). According to [3], formation of plasma streamer in the R_2 gap (Fig. 8 b) could have been caused by the scientist's breath due to the effect of interfacial charge separation during evaporation of water $H_2O(L) \rightarrow K \cdot H_2O^{-1}(L) + H_2O(G) + K \cdot p^+$. The effect is accompanied by formation of a small amount of free protons p^+ (here $K \sim 10^{-6}$ is the coefficient of the distribution).²³ Under normal conditions, the pressure of saturated water vapor amounts to $p = 2.3 \cdot 10^3 \text{ Pa}$, the concentration of water molecules in the air is $N(H_2O) \sim 6 \cdot 10^{17} \text{ cm}^{-3}$. As a result, even with a single exhalation of the scientist the concentration of free protons in R_2 gap could have reached $p^+ \sim 10^{12} \text{ cm}^{-3}$, which is sufficient for the development of a positive streamer (Fig. 8 b) [8, 19]. In this case, the “trigger mechanism” for R_2 breakdown (Fig. 12) was a sharp increase in the voltage U_2 caused by peripheral lightning discharge (4, Fig. 10). Such abrupt changes of $E \sim U_3 \sim \alpha$ are common with the segmented clouds close to the observer [17]. The abrupt changes of α were

²² It was lunch time, meal was being cooked in the kitchen, oven was burnt and water vapors were deposited on the doors. Subsequently exactly these door areas were destroyed at the main breakdown.

²³ The effect was discovered by Volta (1770), it accounts for the negative charge of the Earth surface [17].

repeatedly observed by Richmann and Lomonosov for clouds of $L < 3$ km (Fig. 7), but the authors failed to find due explanation of this effect [4, 5].²⁴

Table 3

*Parameters of schematic of Richmann's injury by a discharge
of atmospheric electricity (Fig. 12)*

Parameter	Prior to discharge	At the moment of discharge
Cloud-to-ground voltage, U_1 , MV	~ 6	25
Cloud-to-aerial voltage, U_2 , MV	~ 6	~ 25
Aerial -to-ground voltage, U_3 , kV	25	100
Electric field at the surface of the Earth, E_\perp , kV/m	~ 6 ↓	25 ↓
Atmosphere-land current, I_1 , A	~ 0.025	~ 2.6
Aerial-to-ground current, I_2 , A	~ 0	2.5
Leakage current (house walls), I_3 , A	~ 0.025	~ 0.1
Atmospheric resistance, R_1 , kΩ	~ 10^8 (10^{11} *)	~ 10^7 (10^7 **)
Breakdown resistance, R_2 , Ω	10^{17}	~ 0
Body resistance, R_3 , Ω	10^4	10^4
Leakage resistance (raw wood), R_5 , Ω	10^6	10^6
Ground resistance, $R_4 \sim R_6$, Ω	~ 10^3	~ 10^3
Released, W_{R5} , W	625	10^3
Released power, W_{R2} , W	0	$2.5 \cdot 10^5$

* – estimate for non-ionized air. ** – estimate with regard to thunderstorm air ions ($N \sim 10^5$ cm⁻³).

To explain the growth of E_\perp at the peripheral discharge (4, Fig. 10), we used a model of a partitioned cloud (Fig. 13). According to Fig. 13, a discharge between points A and E causes annihilation of positive and negative charges in one of the cloud segments. As a result, the electric field E_\perp at point of observation D increases in $\delta E_\perp = E_\perp' / E_\perp \sim \cos^2 \beta / (\cos^2 \beta - \cos^2(\beta + \delta))$ by the time $t \sim 5 - 10\tau$ and more (here $\tau \sim 1 - 5$ s is the characteristic relaxation time of a cloud) [17]. The estimates were made in the approximation of point charges at the cloud height of 1 km. The angles $\delta \sim 6^\circ$, $\beta \sim 50^\circ$ (Fig. 13) were determined from Fig. 10. We obtained $\delta E_\perp \sim 4$ whence under condition of $\alpha \sim 30^\circ \sim E_\perp \sim 25$ kV/m at the moment of discharge we calculated circuit parameters (Fig. 12), as well the readings of Richmann's electrometer prior to discharge (Table 3 and Fig. 11). Then using the equations for a plane capacitor and coaxial line, respectively, we assessed the electric capacity of the cloud $C_1 = \epsilon_0 \epsilon S / H \sim 10^{-8}$ F (here $\epsilon \sim 1$ is for air, $S \sim 10^6$ m² is the effective area of the cloud) and "thunder machine" $C_2 = 4\pi \epsilon_0 \epsilon l / \ln(r_1/r_2) \sim 2 \cdot 10^{-10}$ F (here $l \sim 10$ m, $r_1 \sim 0.5$ cm and $r_2 \sim 100$ cm is conducting wire length, its radius and average distance between the wire and house walls). Then we calculated the maximum charges of the cloud and "thunder machine" – $Q_1 = C_1 U_1 \sim 0.25$ C and $Q_2 = C_2 U_2 \sim 2 \cdot 10^{-5}$ C, and time constants of the "thunder machine" charging at the moment of breakdown $\tau_1 = R_1 C_2 \sim 10^{-3}$ s and $\tau_1' = R_1 C_2 \sim 20$ s for the nonionized atmosphere, respectively. From the relation $\tau_1 \ll \tau_1'$ it follows that the atmosphere over Richmann's house at the moment of breakdown was strongly ionized. In so doing, all the discharges in the house (Fig. 9 b) were

²⁴ Richmann and Lomonosov did not know that positive and negative charges can form simultaneously and then annihilate ([5], p. 523). The abrupt changes in α were attributed by Lomonosov to a transition of "electrical force" between clouds during discharges.

determined by the energy C_2 of charged installation that was constantly “powered” by the energy of charged cloud C_1 , which accounted for their total large value.²⁵ As a result, at the breakdown of the electrode gap ($R_2 \rightarrow 0$), Richmann could pass through himself the shock current I up to ~ 2.5 A, exceeding considerably the lethal value ($I_0 = 0.1$ A) (Table 3) [20]. The scientist's pale body and numerous burns ([4], p. 545) confirm this assumption.²⁶

Thus, the cause of Richmann's death was an extremely rare combination of various unfavorable factors.²⁷ The key factors included the positive charge of the cloud over the house, a dangerous configuration of the discharge gap of the "point-plane" type reducing the discharge voltage by a factor of 3, damp room and clothing, as well as two TE effects that increased the affecting factors of atmospheric charges. This is increased air conductivity close to the aerial due to the burning oven in the house and high concentration of protons $p^+ \sim 10^{12} \text{ cm}^{-3}$ in the gap R_2 caused by the scientist's breath.²⁸ It should be noted that the majority of these effects were known to Richmann, or he even was their discoverer [4]. In particular, Richmann had earlier investigated the effect of air breakdown at reduction of a discharge gap ([4], p. 233), studied “dripping of charges from the tip” and “conducting properties of flame and smoke”, described the effect of “wet” room, etc.) [4]. Richmann also tried to measure the conductivity of water vapor (the experiment with the aeolipile) (Fig. 4 c), but did not estimate its value due to the low sensitivity of his “pointer”. However, as shown above, it is exactly low proton conductivity of water vapors exhaled by the scientist that could be the main reason for his death. Accordingly, the easiest way to prevent the tragedy for Richmann would be to use an electrometer with a protective housing (Fig. 3 b) [20].²⁹ At the same time, the relative safety of Lomonosov and Sokolov under similar conditions has been associated primarily with lower ionization of air around them. As a result, electrical discharges also experienced by them during the storm of July 26, 1753, were of relatively safe spark (brush) type [8].

Conclusions

We have examined the works of Richmann and Lomonosov (1745 – 1753) related to the origin of national thermoelectricity (TE). It is shown that the authors were the first to discover or study in detail TE effects (thermoelectric, atmospheric and so on) in various thermoelectrically-active media belonging to the class of dielectrics (sulfur, resins, air, water, etc.). All TE effects studied by them were of similar physical nature and associated with spatial separation and/or transport of non-equilibrium electric charges in samples with a change in temperature. In some cases the TE effects were further enhanced by the phase transitions and chemical reactions (“melt-crystallization”, “evaporation-condensation”, combustion, etc.) also related to a change in temperature. The distinctive feature of TE effects was their discreteness manifested in the processes of “charging” and

²⁵ Considerable decrease of R_1 could have been also caused by oven burning in the house (Fig. 5 b).

²⁶ At primary respiratory arrest the affected bodies are blue, at primary cardiac arrest – red, white color indicates a simultaneous cessation of breathing and circulation ([20], p. 236).

²⁷ By our estimation, the probability of a casual combination of affecting factors in the incident with Richmann was exclusively small ($P < 10^{-7}$ per single experiment). It is proved by the absence of new similar incidents with researchers for the recent 260 years.

²⁸ Richmann who was constantly talking to Sokolov, did not take off the robe and wet shoes, he took off only a wig, and as a result he was at the installation even with a wet head [4].

²⁹ In this paper, we do not consider the case of simultaneous connection of two Richmann's “thunder machines”. Their series ($U_3' \sim 2U_3$), or parallel ($C_2'' \sim 2C_2$) connection increase essentially the likelihood of the scientist's injury by current (Fig. 5 b).

“discharging” of samples. Thus, even for high U , the TE effects remained virtually harmless for the researchers, except for the cases of electrical breakdown of dielectrics (the incident with Richmann).

References

1. A.A. Buryak, N.B. Karpova, *Essays on the Development of Thermoelectricity* (Kyiv: Naukova Dumka, 1988), 290 p.
2. L.I. Anatychuk, *Dedicated to 70th Anniversary*, Ed. L.M. Vikhor (Chernivtsi: ITE- NANU, 2007), 728 p.
3. M.A. Korzhuev, I.V. Katin, On the Sequence of Discovery of the Basic Thermoelectric Phenomena, *J. Thermoelectricity* **3**, 79 – 90 (2011).
4. G.-V. Richmann, *Proceedings in Physics* (Moscow: Ac.Sc.USSR, 1956), 712 p.
5. M.V. Lomonosov, *Selected Papers on Chemistry and Physics* (Moscow: Ac.Sc. USSR, 1961), 560 p.
6. Yu.A. Khramov, *Physicists. Bibliography* (Moscow: Nauka, 1983), 400 p.
7. V. Gilbert, *On Magnet, Magnetic Bodies and a Large Magnet – the Earth* (Moscow: Ac.Sc. USSR, 1956), 412 p.
8. K.A. Putilov, *Physics Course, Vol.2* (Moscow: State Publishing House of Physics and Mathematics Literature), 584 p.
9. *Electrets*, Ed. G. Sessler (Moscow: Mir, 1983), 478 p.
10. M. Laue, *History of Physics* (Moscow: State Publishing House of Technical and Theoretical Literature, 1956), 232 p.
11. F.T.W. Aepinus, *Theory of Electricity and Magnetism* (Moscow: Ac.Sc. USSR, 1951), 564 p.
12. I.S. Grigoryev, E.Z. Meilikhov, *Physical Properties of Materials* (Moscow: Energiya, 1991), 1232 p.
13. B. Franklin, *Experiments and Observations on Electricity* (Moscow: Ac.Sc.USSR, 1956), 272 p.
14. *The Academy of Sciences of the USSR. Membership (1724 – 1917). Vol.1.* (Moscow: Nauka), 480 p.
15. E.P. Karpeev, *Lomonosov. A Short Encyclopedia* (Saint-Petersburg: Electronic Ed., 2007). 218 p.
16. A.A. Morozov, *Lomonosov* (Moscow: Molodaya Gvardia Publ., 1961), 322 p.
17. V.M. Muchnik, *Physics of Clouds* (Moscow: Gidrometeoizdat, 1974), 352 p.
18. *A Perspective Plan of St. Petersburg 1765 – 1773* (Plan of de St-Hilaire, I. Sokolov, A. Gorikhvostov, etc), Ed. V.S. Sobolev (Saint-Petersburg: Kriga Publ., 2003), p. 126.
19. A.V. Shavlov, The Mechanism of Interfacial Electrostatic Evaporation and Condensation Growth of Ice and Water, *Cryosphere* **12** (2), 52 – 59 (2008).
20. V.E. Manoilov, *Fundamentals of Electrical Safety* (Leningrad: Energoatomizdat, 1991), 480 p.

Submitted 24.10.2013.

ARTICLE PREPARATION RULES

The article shall conform to the journal profile. The article content shall be legible, concise and have no repetitions.

The article shall be submitted to the editorial board in electronic version.

The text shall be typed in text editor not lower than MS Word 6.0/7.0.

Page setup: “mirror margins”- top margin – 2.5 cm, bottom margin – 2.0 cm, inside – 2.0 cm, outside– 3.0 cm, from the edge to page header – 1.27 cm, page footer – 1.27 cm.

Graphic materials, pictures shall be submitted in color or, as an exception, black and white, in .ojp or .cdr formats, .jpg or .tif formats being also permissible. According to author’s choice, the tables and partially the text can be also in color.

The article shall be submitted in English on A4 paper sheets; the number of pages shall not exceed 12. By agreement with the editorial board, the number of pages can be increased.

To accelerate publication of the article, please adhere to the following rules:

- the authors’ initials and names are arranged in the centre of the first page at the distance of 1 cm from the page header, font Times New Roman, size 12 pt, line spacing 1.2;
- the name of organization, address (street, city, postal code, country) – indent 1 cm below the authors’ initials and names, font Times New Roman, size 11 pt, line spacing 1.2, center alignment;
- the title of the article is arranged 1 cm below the name of organization, in capital letters, semi-bold, font New Roman, size 12 pt, line spacing 1.2, center alignment. The title of the article shall be concrete and possibly concise;
- the abstract is arranged 1 cm below the title of the article, font Times New Roman, size 10 pt, in italics, line spacing 1.2 ,center alignment;
- key words are arranged below the abstract, font Times New Roman, size 10 pt, line spacing 1.2, justified alignment. The title “Key words” – font Times New Roman, size 10 pt, semi-bold;
- the main text of the article is arranged 1 cm below the abstract, indent 1 cm, font Times New Roman. size 11 pt, line spacing 1.2, justified alignment;
- formulae are typed in formula editor, fonts Symbol, Times New Roman. Font size is “normal” – 12 pt, “large index” – 7 pt, “small index” – 5 pt, “large symbol” – 18 pt, “small symbol” – 12 pt). The formula is arranged in the text, centre aligned and shall not occupy more than 5/6 of the line width, formulae are numbered in round brackets right;
- dimensions of all quantities used in the article are represented in the International System of Units (SI) with the explication of the symbols employed;
- figures are arranged in the text. The figures and pictures shall be clear and contrast; the plot axes – parallel to sheet edges, thus eliminating possible displacement of angles in scaling;
- tables are arranged in the text. The width of the table shall be 1 cm less than the line width. Above the table its ordinary number is indicated, right alignment. Continuous table numbering throughout the text. The title of the table is arranged below its number, center alignment;
- references should appear at the end of the manuscript. References within the text should be enclosed in square brackets. References should be numbered in order of first appearance in the text. Examples of various reference types are given below.

- L.I. Anatychuk, *Thermoelements and Thermoelectric Devices: Handbook* (Kyiv: Naukova Dumka, 1979), p.766. (Book)
- T.M. Tritt, Thermoelectric Phenomena, Materials, and Applications, *Annual Review of Materials Research* **41**, 433 (2011). (Journal paper)
- U. Ghoshal, *Proceedings of the XXI International Conference on Thermoelectrics* (N.Y., USA, 2002), p. 540. (Proceedings Conference)

The article should be supplemented by:

- letter from the organization where the work was performed or from the authors of the work applying for the publication of the article;
- information on the author (authors): last name and initials; full name and postal address of the institution where the author works; academic degree; position; telephone number; E-mail;
- author's (authors') photo in color or, as an exception, in black and white. With the number of authors more than two their photos are not given;
- author's application to the following effect:

<p>We, the undersigned authors, ... transfer to the founders and editors of "Journal of Thermoelectricity" the right to publish the article...in Ukrainian, Russian and English. This is to confirm that the present publication does not violate the copyright of other persons or organizations.</p>	
Date	Signatures

Below is given an example of article preparation.

Author's
photo
 3×4 cm

A.I. Casian¹, B.M. Gorelov²

¹Technical University of Moldova,
168, Stefan cel Mare Ave.,
Chisinau, MD-2004, Moldova;
²Institute of Surface Chemistry of National Academy
of Sciences of Ukraine, 17, Gen. Naumov Str.,
Kyiv, 03164, Ukraine

Author's
photo
 3×4 cm

STATE OF THE ART AND PROSPECTS OF THERMOELECTRICITY ON ORGANIC MATERIALS

The aim of the paper is to analyze the expected thermoelectric opportunities of organic materials, including some highly conducting quasi-one-dimensional crystals. It is shown that interest of investigators in these materials has been growing recently. Quasi-one-dimensional organic crystals have high prospects for thermoelectric applications. These materials combine the properties of multi-component systems with more diverse internal interactions and of quasi-one-dimensional quantum wires with increased density of electronic states. It is shown that the values of the thermoelectric figure of merit $ZT \sim 1.3 - 1.6$ at room temperature are expected in really existing organic crystals of tetrathiotetracene-iodide, TTT_2I_3 , if the crystal parameters are approaching the optimal ones.

Key words: thermoelectricity, tetrathiotetracene-iodide, polarizability.

Introduction

It is known that conducting organic materials usually have much lower thermal conductivity than the inorganic materials. Moreover, the organic materials can be fabricated by simpler chemical methods, and it is expected that such materials will be less expensive in comparison with the inorganic ones. Exactly these properties attracted attention to such materials for the use in thermoelectric (TE) applications long time ago [1, 2]. In spite of relatively high value of the thermoelectric figure of merit $ZT = 0.15$ at room temperature observed in polycopper phthalocyanine [2] as early as 1980, the thermoelectric properties of organic materials are still weakly investigated. This situation has the only explanation that thermoelectricians are still weakly interested in organic materials, and organic chemists are also weakly interested in thermoelectric materials. Moreover, in order to seek good organic thermoelectrics, it is necessary to organize multidisciplinary consortiums of physicists, organic chemists and engineers in the field of thermoelectricity.

The aim of this paper is to present briefly the state-of-the-art of investigations in the area of new organic thermoelectric materials and to describe the nearest expected results for really existing quasi-one-dimensional organic crystals of tetrathiotetracene-iodide, TTT_2I_3 .

Quasi-one-dimensional organic crystals of TTT_2I_3

The structure of quasi-one-dimensional organic crystals of tetrathiotetracene-iodide, TTT_2I_3 , has been briefly described in [34]. These needle-like crystals are formed of segregate chains or stacks of planar molecules of tetrathiotetracene TTT , and iodine ions. The chemical compound TTT_2I_3 is of mixed-valence: two molecules of TTT give one electron to the iodine chain which is formed from I_3^- ions. The

conductivity of iodine chains is negligibly small, so that only *TTT* chains are electrically conductive and holes serve as carriers. The electrical conductivity σ along *TTT* chains at room temperature varies between 10^3 and $10^4 \Omega^{-1} \text{cm}^{-1}$ for crystals grown by gas phase method [35], and between 800 and $1800 \Omega^{-1} \text{cm}^{-1}$ for crystals grown from solution [36]. Thus, the conductivity is very sensitive to crystal impurity and perfection which depends on growth method. In the direction perpendicular to chains σ is by three orders of magnitude smaller than in the longitudinal direction and is neglected. ...

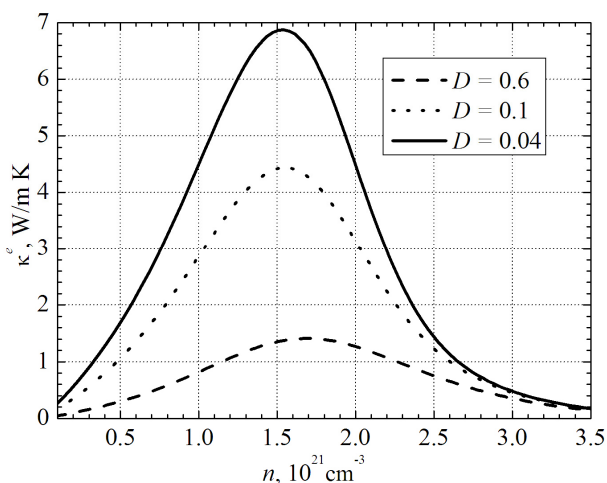


Fig. 1. Dependences of electron thermal conductivity κ^e on n .

$$\sigma = R_0, S = R_i / eTR_0, \kappa^e = (e^2 T)^{-1} (R_2 - R_i^2 / R_0), \quad (1)$$

Thermoelectric properties

Expressions (2) – (3) have been calculated in order to determine the thermoelectric properties of quasi-one-dimensional organic crystals of TTT_2I_3 with different degrees of purity....

Conclusions

The state-of-the-art of research on new organic materials for thermoelectric applications is analyzed. It is shown that the interest of investigators in these materials has been growing in recent years. The highest value of $ZT \sim 0.38$ at room temperature has been measured in doped acetylene, with the only problem that this material is not stable. Accurate control of the oxidation level in poly (3, 4-ethylenedioxythiophene) (PEDOT) gave the power factor $324 \mu\text{W}\cdot\text{m}^{-1}\text{K}^{-2}$ and in combination with its low intrinsic thermal conductivity ($\kappa = 0.37 \text{ W}\cdot\text{m}^{-1}\text{K}^{-1}$) yielded $ZT = 0.25$ at room temperature, and this material is air-stable....

References

1. Ali Shakouri, Recent Developments in Semiconductor Thermoelectric Physics and Materials, *Annu.Rev.Mater.Res.* **41**, 399-431 (2011).
2. L.I. Anatychuk, *Thermoelectricity, Vol.2, Thermoelectric Power Converters* (Kyiv, Chernivtsi: Institute of Thermoelectricity, 2003), 376p.
3. M.E. Bengen, *German Patent Appl. OZ 123, 438, 1940; German Patent 869,070, 1953*, Tech. Oil Mission Reel, 143,135, 1946.